

**Neuromechanical Mechanisms of Locomotion in *C. elegans***

By

Carter L. Johnson

DISSERTATION

Submitted in partial satisfaction of the requirements for the degree of

DOCTOR OF PHILOSOPHY

in

APPLIED MATHEMATICS

in the

OFFICE OF GRADUATE STUDIES

of the

UNIVERSITY OF CALIFORNIA

DAVIS

Approved:

---

Timothy J. Lewis

---

Robert D. Guy

---

Becca Thomases

Committee in Charge

2020

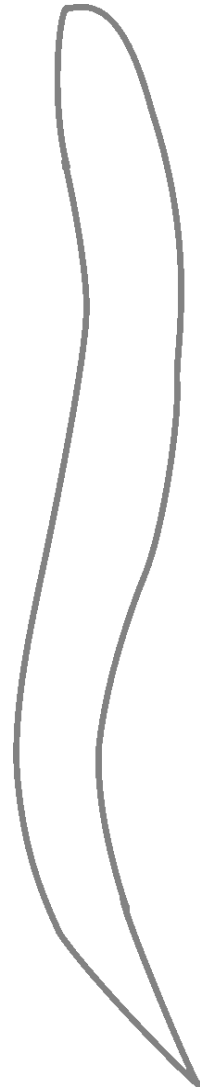
© Carter L. Johnson, 2020. All rights reserved.

“ Oh to be a nematode!  
One that came into being in July: glorious!

No one doubts our numbers, easily a Million species  
and never to be counted, not ever.

Shine on we beasties!  
2018 and forever,  
Controllers of the universe! ”

— George Quentin Baker, July 4, 2018



# Contents

Abstract	v
Acknowledgments	vi
Chapter 1. Introduction	1
1.1. A Brief History of <i>C. elegans</i> as a Model Organism	2
1.2. <i>C. elegans</i> Neurophysiology	4
1.3. <i>C. elegans</i> Biomechanics	6
1.4. Previous Models of <i>C. elegans</i> Forward Locomotion	6
1.5. Remaining Questions	9
Chapter 2. Neuromechanical Model of Forward Locomotion in <i>C. elegans</i>	11
2.1. Model Development	11
2.2. Model Discretization for Numerical Simulation	16
2.3. Parameter Discussion	17
2.4. Model Results	18
Chapter 3. Phase Model: Insight Into Mechanisms Underlying Gait Adaptation	25
3.1. Isolated Neuromechanical Modules are Intrinsic Oscillators	25
3.2. Network of Coupled Oscillators	27
3.3. Two-Oscillator Analysis Explains the Coordination Mechanism	29
3.4. Mechanism for Gait Adaptation Holds in Six-Oscillator Case	35
Chapter 4. Neuromechanical Oscillator Model	38
4.1. Bifurcation Analysis of the Neuromechanical Oscillator Model	38
4.2. Phase Response Properties of the Neuromechanical Oscillator Model	48

Chapter 5. Reduction of the Neuromechanical Oscillator to a 1-D Map Captures Limit Cycle Dynamics	58
5.1. Reduction of the Neuromechanical Oscillator	58
5.2. 1-D Map Captures Limit Cycle Dynamics	63
Chapter 6. Chains of Different Numbers of Modules	70
Chapter 7. Discussion and Conclusions	75
Appendix A. Neuromechanical Model Details	80
A.1. Defining Wavelength	80
A.2. Derivation of Mechanical Parameters	81
Appendix B. Theory of Weakly Coupled Oscillators	83
B.1. Phase and Inverse Phase Map	83
B.2. Weakly Coupled Oscillators	84
B.3. Computing the Phase Response Curves	86
B.4. Computing the Interaction Functions Quickly Using the Fourier Transform	88
Appendix C. Deriving the 1-D Poincaré Map	90
C.1. Steady-State Analysis	90
C.2. Map Derivation	91
C.3. Numerically Finding the Roots of the Map Branches	97
C.4. Limit Cycle from Map	99
Bibliography	100

**Abstract**

Understanding principles of neurolocomotion requires the synthesis of neural activity, sensory feedback, and biomechanics. The nematode *C. elegans* is an ideal model organism for studying locomotion in an integrated neuromechanical setting because its nervous system is well characterized and its forward swimming gait adapts to the surrounding fluid using sensory feedback. However, it is not understood how the gait emerges from mechanical forces, neuronal coupling, and sensory feedback mechanisms. Here, a modular neuromechanical model of *C. elegans* forward locomotion is developed and analyzed. The model captures the experimentally observed gait adaptation over a wide range of parameters, provided that the muscle response to input from the nervous system is faster than the body response to changes in internal and external forces. The model is analyzed as a system of coupled neuromechanical oscillator modules using the theory of weakly coupled oscillators to identify the relative roles of body mechanics, neural coupling, and proprioceptive coupling in coordinating the undulatory gait. The analysis shows that the wavelength of body undulations is set by the relative strengths of these three coupling forms and the experimentally observed decrease in wavelength in response to increasing fluid viscosity is the result of an increase in the relative strength of mechanical coupling, which promotes a short wavelength. Parameters of the neuromechanical modules were also explored to assess their effects on the existence, period, amplitude, and phase response properties of the oscillations; this analysis allows the coordination trend of the full neuromechanical model to be inferred from the properties of the individual neuromechanical oscillator modules themselves. The neuromechanical module is also reduced to a form that is analytically piecewise solvable, which allows for the construction of a 1-D Poincaré map that captures the limit cycle dynamics. This builds a framework for future analysis of the biophysical mechanisms underlying the oscillator properties and thus the coordination of the full neuromechanical model. The systematic analysis of the neuromechanical model presented in this dissertation provides a deeper understanding of how the interactions between the neuromechanical components of the *C. elegans* forward locomotion system produce coordination and gait adaptation.

## Acknowledgments

I would like to thank my advisors, Professors Tim Lewis and Bob Guy, for teaching, training, and mentoring me for the past 7 years. Tim, thanks for taking me on as naive young student, supporting me all this time, and molding me into a less-naive scientist. Bob, thanks for always being skeptical of simulation outputs and challenging me to think critically about research. It's been a privilege to work with both of you.

I would like to thank Professors Becca Thomases and Elena Fuchs for their personal support and dedication to making the department a more welcoming place. Becca, thank you for all the group meetings, and of course for chairing my qualifying exam and dissertation committees. Elena, thank you for letting me help out with M-Pact. Your work with that school has truly inspired me to be a more socially-focused academic.

Thank you to the math department staff, especially Sarah Driver, Tina Denena, and Victoria Whistler. Thank you also to Professors Sam Walcott and Brian Mulloney for serving on my qual committee, and thanks Dr. Korana Burke and Professor Craig Benham for giving me the opportunity to develop math bio curriculum.

A big thank you to my big loving and supportive family: Mom and Dad, Nolan and Spencer, Grandma Jean and Grandpa Quentin, Nonni, Margo and Thomas, Auntie Rachel and Uncle Rick, Auntie Lisa, Aaron, Taylor, Emma, Logan, and Jady. To all the educators in my family - Grandma Jean, Grandpa Quentin, Auntie Rachel, Auntie Lisa, and Mom - thanks for inspiring in me a love for education.

Thank you to all of my friends in the math department and around Davis, especially Christine Angeles, Sam Fleischer, Sattik Ghosh, Emily Meyer, Ducko Nguyen, Alex Randazzo, and Eric Wetzel.

Finally, thanks to my wife, Becky, for always being there for me, for challenging me to be a better scientist, and for being my best friend. One day, I hope to live up to the standard you set. You make me want to have a wetter brain.

## CHAPTER 1

# Introduction

The central goal of neuroethology is to understand how an organism's body and nervous system interact with its environment to produce behaviors such as locomotion. Model organisms have been used to study the complex interactions between the nervous system, body mechanics, and environmental dynamics in generating and coordinating locomotion [24, 33]. Some studies of locomotion in model organisms highlight feedforward control of locomotion, where the nervous system drives motor activity and sensory feedback plays only a modulatory role; these include swimming behavior in lamprey, crayfish, and leeches [8, 36, 45, 46, 47, 50]. However, other organisms, such as cockroaches and stick insects, can only be understood as fully integrated neuromechanical systems because sensory feedback is essential to generate and coordinate movements [4, 17, 24, 32, 42]. This sensory feedback is necessary for navigating more complex environments and can often lead to gait adaptation. The nematode *C. elegans* is an ideal model organism for studying locomotion in an integrated neuromechanical setting because of its relatively simple and fully-described nervous system [53], limited stereotypical locomotive behavior [40], dependence on sensory feedback for forward locomotion [43, 51], and undulatory gait that adapts to different fluid environments.

*C. elegans* locomote forward using alternating dorsal and ventral body bends that propagate from anterior to posterior. The properties of this undulatory gait adapt to fluid environments of different viscosities: higher external fluid viscosities result in slower undulations of shorter wavelengths [3, 15, 49]. Previously, it was thought that *C. elegans* had two distinct gaits, swimming and crawling. However, recent experiments have shown that the wavelength and frequency of swimming in highly viscous fluids resemble crawling on agar surfaces [3, 15], and instead of a sharp swim/crawl transition, there is a smooth transition between the two gaits as the fluid viscosity of the environment is varied [3, 15, 49]. How this adaptation in gait emerges from the interactions between the external environment, mechanical forces, and internal sensory feedback mechanisms is not understood.

There are several hypotheses for how the undulatory gait is generated and coordinated [19]; however, it is generally agreed that proprioception plays a key role [5,38,51]. One hypothesis is that there is a central pattern-generating (CPG) neural unit in the head that initiates the propagation of the bending wave — higher fluid viscosities slow the propagation and shorten the wavelength [28,51]. Another hypothesis is that the ventral nerve cord consists of a network of neural modules that are capable of either (i) intrinsic neural oscillations [41] or (ii) intrinsic *neuromechanical* oscillations (i.e., involving an entire feedback loop from neural to muscular to body mechanics and back through proprioception) [5,7]. Recent experiments by Fouad et al. [16] support the presence of multiple neural or neuromechanical oscillators, and gait adaptation has been demonstrated in computational models consisting of a chain of neuromechanical oscillators [5,9,11]. However, it is still unclear how the interplay between neural, proprioceptive, and mechanical coupling gives rise to gait adaptation.

Here, we introduce a neuromechanical model of the *C. elegans* forward locomotion system. We use our model to systematically analyze the role of body mechanics, neural coupling, and proprioceptive coupling in gait adaptation. The model captures the experimentally observed gait adaptation over a wide range of parameters, provided that the muscle response to input from the nervous system is faster than the body response to changes in force. The modular structure of our model allows the use of the theory of weakly coupled oscillators to further dissect out the mechanisms underlying gait adaptation. Specifically, we assess the influence of each coupling modality (mechanical, neural, and proprioceptive). We find that proprioception leads to a posteriorly-directed traveling wave with a characteristic wavelength. Neural coupling promotes synchronous activity (long wavelength), and mechanical coupling promotes a high spatial frequency (short wavelength). The wavelength of the undulatory waveform is set by the relative strengths of these three coupling forms. As the external fluid viscosity increases, the mechanical coupling strength increases and the wavelength decreases, resulting in the observed wavelength trend of gait adaptation.

### 1.1. A Brief History of *C. elegans* as a Model Organism

*C. elegans* has a long history as a model organism in biology. Typically found in soils and compost heaps around the world, they can now be commonly found on Petri dishes in university

labs. *C. elegans* and other nematodes have been studied since the invention of the microscope in the 17th century, and early studies focused on species classification and culture methods, i.e., how to systematically raise nematodes in a reproducible way in the laboratory [40]. This early work was important in devising the methods that would lead to *C. elegans*' widespread use later: specifically, how to grow healthy populations on agar plates and breed them sexually and asexually.

In the 1960s, molecular biologist Sydney Brenner was searching for an animal candidate to start a new research program in developmental biology and neurobiology and found *C. elegans*. The appeal of *C. elegans* was its fast growth, ease of culture, transparent and small body for microscopic observations, and relatively invariant cell composition [40]. Rapid genetic and developmental research began in this research group, and many mutants were isolated and classified. Some mutants exhibited phenotypes with defective behavior; many of these had alterations in the nervous systems [53]. How these changes to the nervous system resulted in behavior defects posed a fascinating scientific problem.

Inspired by work on neuronal cell invariance and nervous system connectivity in the larger parasitic nematode, *Ascaris*, by R. Goldschmidt in the early 20th century [20], a similar project was undertaken to understand and characterize the neurophysiology of *C. elegans* [52]. This resulted in the first mapping of an entire nervous system at the cellular level in any animal [53], an achievement that to this day is still unrivaled. Over a period of 15 years (1970-1986), John White, Eileen Southgate, Nichol Thompson, and Sydney Brenner reconstructed the structure and connectivity of the hermaphrodite *C. elegans* nervous system by piecing together a massive puzzle of thousands of cross-sectional micrographs [53]. Using laser ablation of neurons, they systematically determined the role of most cells in development or behavior. Through building this canonical structure of the *C. elegans* nervous system, these scientific pioneers paved the way for understanding the mechanisms by which this nervous system produces behavior.

Today, *C. elegans* is used as a model organism in almost every area of biology, including genomics, cell biology, neuroscience, and aging. Hundreds of laboratories around the world raise and study *C. elegans*, and many specimens are in direct lineage from Brenner's lab. These labs form a tight scientific community that shares tools, methods, and common databases (Wormbase.org [22], WormAtlas.org [1]). The biannual *C. elegans* International Conference regularly draws over a

thousand scientists presenting novel *C. elegans* research. Yet despite all this scientific progress and achievement, the full neuromechanical mechanisms underlying coordination are not understood.

## 1.2. *C. elegans* Neurophysiology

The *C. elegans* hermaphrodite has 302 individual neurons, which are arranged into 118 classes based on morphology and connectivity [53]. This nervous system structure is invariant between animals, and many mutants are classified by neural changes that manifest as behavioral defects. Most of the neurons are located in the head of the nematode: sensory neurons such as chemoreceptors and touch-sensitive neurons; motor neurons involved in controlling head turns; and interneurons that connect neurons to other neurons, e.g. to enable communication between sensory and motor neurons [53]. The rest of the neurons are distributed along the ventral nerve cord, which runs down the ventral side from the head to the tail [53].

*C. elegans* has 75 motor neurons that are distributed along the ventral nerve cord; these are grouped functionally into six modules for locomotion [23]. The motor neurons in each module synapse onto the ventral and dorsal muscles along the body wall, which are responsible for the bending of that body region. Each module contains motor neurons of the classes VB, VA, VD, which synapse onto ventral muscles, and AS, DB, DA, and DD, which synapse onto dorsal muscles [53]. These motoneurons are involved in either forward locomotion (VB, DB), backward locomotion (AS, VA, DA), or both (VD, DD), and are connected to interneurons in the head that decide which locomotive circuit is activate [53]. The interneurons AVB and AVA activate the forward and backward locomotion circuits respectively [53]. In this dissertation, we focus on the forward locomotion circuit, so we only consider neurons of the classes AVB, VB, VD, DB, and DD. Another key fact is the different numbers of neurons in each class: 7 DB neurons, 11 VB neurons, 6 DD neurons, and 13 VD neurons [53]. Thus, the basic neural module for forward locomotion consists of 1 DB, 1 DD, 2 VB, and 2 VD neurons, and there are six such repeated modules in the body [23,58].

While much is known about the nervous system structure and connectivity, probing the electrophysiology of the neurons in *C. elegans* is difficult in part due to the small size and pressurized nature of the nematode body, so many neural properties, such as synaptic strengths and membrane potential timetraces, are unknown [10,19,58]. Electrophysiological recordings of related nematode

*Ascaris* motor neurons have shown electrotonic potentials instead of all-or-nothing action potentials [48]. That is, the neurons switch between steady “on” and “off” signals, instead of the brief output spikes typically associated with neural signaling. Similar recordings of head motor neurons involved in head-turns in *C. elegans* have shown that those motor neurons also exhibit electrotonic potentials [34], so it is generally thought that the motor neurons in the ventral nerve cord, particularly those involved in forward locomotion, act as similar bistable, non-spiking elements [5].

The neural connectivity alone does not reveal every aspect of the *C. elegans* forward locomotion circuit. Proprioception, or sensory feedback regarding the mechanical state of the body, is thought to be necessary for the generation and coordination of the locomotive gait [5, 51, 58]. Proprioceptive interneurons have been found in the head circuit [43], and proprioceptive processes are hypothesized to exist somewhere in the B-class motorneurons, either in neural processes that extend posteriorly that don’t have any discernible role [53] or elsewhere [51]. Wen et al. [51] showed that the B-class motorneurons respond to stretching and bending in local and anterior segments. While proprioception is necessary for the generation of the locomotive rhythm, it is not clear what its exact role in coordination is in comparison with other coordination mechanisms such as neural coupling and body mechanics.

An outstanding question in *C. elegans* neurolocomotion is whether the rhythmic bending in forward locomotion is driven by a central-pattern-generating (CPG) neural unit in the head and/or by coupled neural or neuromechanical oscillator modules. While the neural circuitry contains motifs that could theoretically function as CPGs according to computational models [41], no CPGs have been found experimentally for the forward locomotion circuit [10, 58]. In the backward circuit, Gao et al. [18] showed that the A-class motor neurons can function as intrinsic neural oscillators that can drive backward locomotion. There is recent experimental evidence that the forward motor circuit functions as a system of coupled neural or neuromechanical oscillators: Fouad et al. [16] showed that *C. elegans* is capable of decoupled “two-frequency undulations”. By suppressing neural activity in the neck region during forward locomotion, the head and body can undulate seemingly independent of one another at different frequencies (the head slower and the body faster). This evidence supports the presence of multiple neural or neuromechanical oscillators in the forward circuit, though not as conclusively as in the backward circuit [18].

### 1.3. *C. elegans* Biomechanics

*C. elegans* normally live in the gaps between damp soil particles or decomposing biomass, in films of water that are held to surfaces via surface tension [53]. They locomote via undulation, alternating between dorsal and ventral body bends that propagate in a wave-like fashion from anterior to posterior in forward locomotion and reverse in backward locomotion. The head is capable of making turns so that the nematode can navigate its environment [53]. The forward gait can be represented in 2-D, since the body only bends in the ventral-dorsal plane [5, 12].

The body of *C. elegans* is about 1 mm long and cylindrical with an average radius of 40  $\mu\text{m}$ , tapering off towards the head and the tail. The body is covered by a tough elastic cuticle, lined with interior muscles, and is hydrostatically pressurized like a water-filled hose. However, measuring the body's mechanical properties, such as its stiffness and viscosity, is difficult. These mechanical properties have been measured and estimated across several orders of magnitude and how active muscle contractions affect them is not clear [2, 15, 49]. Active biomaterials are notoriously difficult to model mechanically, as it is difficult to piece apart the natural properties of the body material from the active biological components.

The kinematics of its forward undulatory gaits are typically characterized by the undulation frequency, wavelength, and amplitude. The undulation amplitude is highest in the head of the worm and decreases along the body towards the tail [3]. In water, the swimming wavelength and frequency is long and fast (roughly 1.5 bodylengths and 1.8 Hz) [15]. On agar, the crawling wavelength and frequency is short and slow (0.65 bodylengths and 0.3 Hz) [15]. Previously, it was thought that these were two distinct gaits (swimming and crawling). However, recent experiments have shown that the wavelength and frequency of swimming in highly viscous fluids resemble crawling on agar surfaces [3, 15], and instead of a sharp swim/crawl transition, there is a smooth transition between the two gaits as the viscosity of the fluid environment is varied [3, 15, 49]. Increasing the fluid viscosity shortens the undulation wavelength and slows the undulation frequency.

### 1.4. Previous Models of *C. elegans* Forward Locomotion

Understanding locomotion involves the integration of neural dynamics, sensory feedback, and body mechanics. Mathematical models have been particularly useful in putting these separate

pieces together to develop an integrated neuromechanical understanding [24, 33]. In particular, modeling of *C. elegans* forward locomotion has played a major role in developing the theories of rhythm generation and coordination in *C. elegans*. Several models [5, 28, 38] predicted the necessity of proprioceptive feedback in generating the bending wave and in adapting the gait, which experiments later verified [51].

There are several hypotheses for how the undulatory gait is generated and coordinated, and mathematical models have been crucial to understanding how the experimental data supports each hypothesis [19]. One hypothesis is that there is a central pattern-generating (CPG) neural unit in the head that initiates the propagation of the bending wave — higher fluid viscosities slow the propagation and shorten the wavelength [28, 51]. Another hypothesis is that the ventral nerve cord consists of a network of neural modules that are capable of either (i) intrinsic neural oscillations [41] or (ii) intrinsic *neuromechanical* oscillations (i.e., involving an entire feedback loop from the neurons to the muscles to the body mechanics and back through proprioception) [5, 7]. In all of these hypotheses, proprioception is necessary to generate and/or coordinate the bending wave.

The earliest model of *C. elegans* forward locomotion was developed by Ernst Niebur and Paul Erdos in the early 90s [12, 38, 39], shortly after the publication of the connectome by White et al. [53] in 1986. They modeled the nematode crawling on agar, carefully deriving the mechanical forces between the body and the agar grooves it carves out as it moves, and they modeled the motor neurons as bistable elements (i.e., with electrotonic potentials) driven by a neural CPG in the head. Through quantitative comparisons between their mathematical model and experimental measurements, they deduced that proprioception is necessary to generate and propagate the bending wave. However, their work was limited to forward crawling on agar and relied heavily on a neural head-CPG.

Later work by Netta Cohen and colleagues continued to explore the role of proprioception in generating and coordinating the undulatory gait [3, 5, 6, 7, 9, 11]. They used a more modular version of Niebur and Erdos' neural circuit, and modeled the body mechanics against realistic environmental forces in both fluids and agar substrates. The model functions as a chain of coupled

neuromechanical oscillator modules, where proprioception is an essential component of the rhythm-generating mechanism. Cohen sought to characterize the swim/crawl gait transition using this neuromechanical model, and concurrent experimental work showed that the gait adapted to fluids of intermediate viscosities in a continuous fashion, i.e., the environment modulates a single gait [3]. Their neuromechanical model showed that the proprioceptive mechanism, which was responsible for generating the bending oscillations of each module, could also account for the modulation of this gait [5]. However, how the trend of gait adaptation emerges from the components of the model is not understood. Specifically, the role of proprioception in coordination, in comparison to neural coupling and body mechanics, was not investigated in these models.

Other groups (Karbowski et al. [28], Izquierdo, Olivares, and Beer [26, 41], and Kunert et al. [31]) have focused mostly on the neural dynamics without the biomechanical aspect, seeking to understand the mechanisms of rhythm generation rather than explain gait adaptation. Karbowski et al. [28] proposed that proprioception must be necessary to generate the neuromechanical oscillations throughout the body and also proposed two rhythm-generating mechanisms. In the first, a neural CPG in the head drives the oscillations, and proprioceptive feedback acts to propagate the oscillations and slow down the emerging rhythm, as in the Erdos and Niebur model [12]. In the second, proprioceptive feedback in the head generates a neuromechanical head CPG, which is coupled to neuromechanical oscillators down the body in a similar way as in the Boyle et al. model [5]. Olivares et al. [41] further explored this range of possible rhythm-generation mechanisms by using an evolutionary algorithm to find parameter regimes in which the model motor circuit could oscillate, and interpreting these outcomes as rhythm-generation mechanisms. Izquierdo et al. [26] then used the biomechanical model of Boyle et al. [5] to determine whether the theoretical rhythm-generating mechanisms in the neural circuit yielded appropriate locomotion on agar. Kunert et al. [31] examined the entire neural connectome, modeling the whole system with simple neural dynamics, and used “proprioceptive-like sensory inputs” to their neural model to show how the entire nervous system is arranged to encode dynamical structures that correspond to locomotion states. These computational models have been used to support several rhythm-generation hypotheses, so whether *C. elegans* forward locomotion is driven by a head-CPG, coupled neural oscillators, or coupled neuromechanical oscillators remains unclear.

## 1.5. Remaining Questions

From an experimental point of view, many of the key players in forward locomotion and gait adaptation have been identified. The motor neurons involved are known and the mechanism of proprioceptive feedback, while not physiologically identified, has been well-established as a necessary ingredient for forward locomotion. However, how all these pieces integrate together to generate the undulatory rhythm and adapt the gait to the environment requires computational and mechanistic modeling.

The state-of-the-art neuromechanical model for *C. elegans* remains that of Boyle et al. [5] and later refinements [9,11]. These models are able to capture gait adaptation, however, the complexity of the models limits their ability to systematically assess the relative roles of body mechanics and proprioception in coordination. Here, we present a simpler mechanical model in tandem with a similar neural model in order to investigate the roles of proprioception, neural coupling, and body mechanics in coordinating locomotion and find a mechanism for gait adaptation.

In Chapter 2, we present a neuromechanical model of the *C. elegans* forward locomotion system that is complicated enough to capture the complex behavior of gait adaptation, but simple enough to analyze the mechanisms behind the behavior. Our model captures the experimentally observed gait adaptation over a wide range of parameters, provided that the muscle response to input from the nervous system is faster than the body response to changes in force, suggesting an ordering on the relatively unknown system timescales.

Furthermore, the modular structure of our model allows us to leverage the theory of weakly coupled oscillators to dissect out the mechanisms behind gait adaptation. The theory of weakly coupled oscillators is a mathematical tool that has been useful in understanding motor rhythm coordination in other model organisms [29, 30, 44, 45, 55, 56]. In Chapter 3, we introduce the technique to the *C. elegans* modeling community in order to identify the influence of each coupling modality (mechanical, neural, and proprioceptive) in the forward locomotion system.

In Chapter 4, we also explore how parameters of the neuromechanical modules affect the existence, period, and amplitude of their oscillations as well as their phase response properties. Through this analysis, we are also able to infer the coordination trend of the full neuromechanical model from the properties of the individual neuromechanical oscillator modules themselves. In Chapter

5, we show that with a few additional simplifying assumptions, we can also reduce the oscillator model to a form that is analytically piecewise solvable. This reduction allows us to construct a 1-D Poincaré map that captures the limit cycle dynamics, which we use as a framework for future analysis of the biophysical mechanisms underlying the oscillator properties and thus the coordination of the full neuromechanical model. In Chapter 6, we show that our model is able to capture gait adaptation independent of the number of oscillator modules we consider, given that the parameters are adjusted carefully. The systematic analysis of our neuromechanical model presented in this dissertation provides a deeper understanding of how the many different neuromechanical components interact to produce coordinated locomotion.

## CHAPTER 2

### Neuromechanical Model of Forward Locomotion in *C. elegans*

The neuromechanical model developed here describes the motor circuit, body-wall muscles, and the resulting body shapes of *C. elegans*. The body description is derived from a continuous centerline-approximation of an active viscoelastic beam, whereas the muscles and neural subcircuits are discrete in nature. The model for the motor circuit uses the repeated motif of Haspel and O’Donovan [23]: 6 modules of roughly 12 motor neurons and 12 muscle cells, of these 12 repeated motor neurons roughly 6 (the dorsal/ventral B and D-class neurons) are responsible for forward locomotion. The model also includes proprioception: the B-class motor neurons respond to bending in the local and anterior regions of the body [51, 58].

A schematic of this model is shown in Figure 2.1, which highlights the modular structure of the neural circuit, body-wall muscles, and the corresponding body region. Within each module, the motor subcircuit drives the body-wall muscles, which in turn apply contractile forces to bend the corresponding body region. The body mechanics then feed back into the neural circuit through proprioceptive feedback, which translates body-wall length changes into neural signals. This structure allows each module to function, in isolation, as a neuromechanical oscillator, and it suggests that the full body functions as a system of coupled neuromechanical oscillators.

#### 2.1. Model Development

**2.1.1. Body Mechanics.** The nematode body is modeled as an active viscoelastic beam for small amplitude displacements submerged in fluid. *C. elegans* usually operates in a regime where inertia plays a minor role (i.e., low Re), thus the equation of motion is a balance of internal elastic forces, internal viscous forces, and a fluid drag force described by a local drag coefficient  $C_N$  [15, 49, 54]:

$$(2.1) \quad C_N \dot{y} = -k_b \partial_{xx} \left( \kappa + \frac{\mu_b}{k_b} \dot{\kappa} + M(x, t) \right),$$

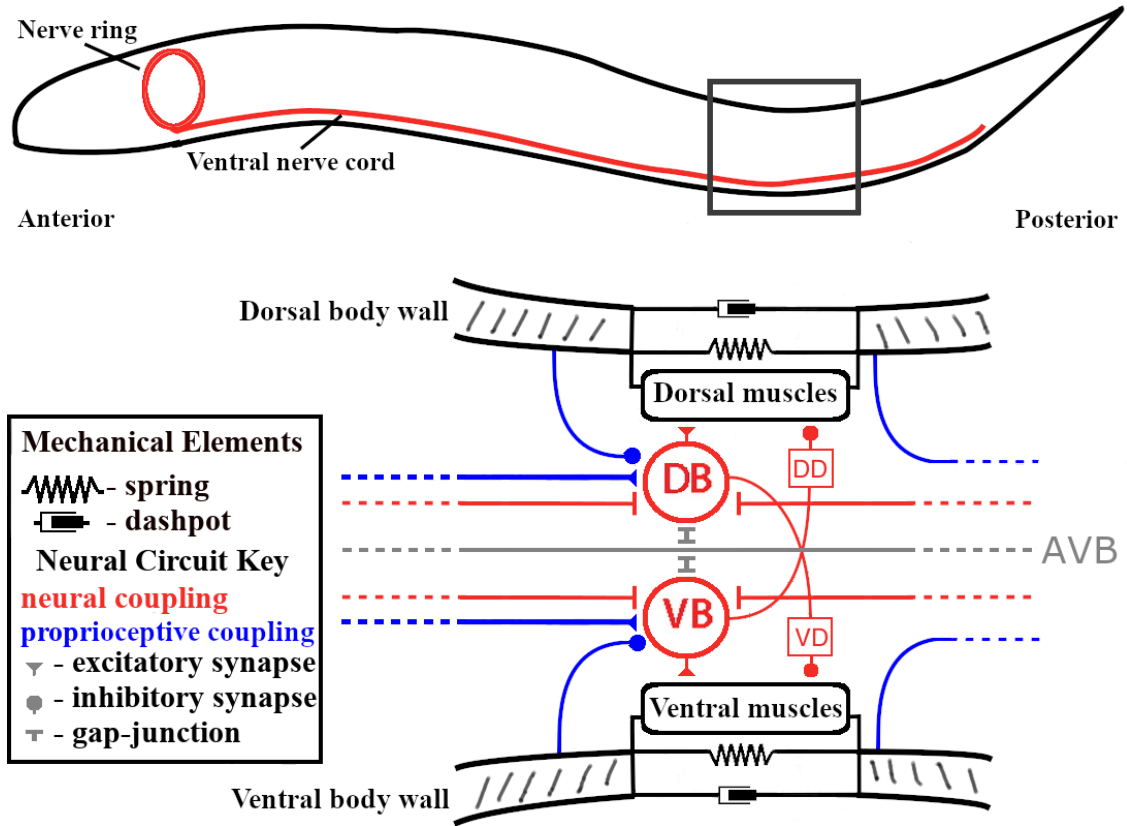


FIGURE 2.1. The highlighted schematic here depicts the repeating neuromechanical module: a 4-motoneuron functional unit consisting of DB, VB, DD, and VD-class neurons, the post-synaptic muscles, and corresponding body wall region. The dorsal B-class (ventral B-class) neurons are excitatory and synapse onto the ipsilateral muscles and contralateral D-class neurons. The dorsal D-class (ventral D-class) neurons are inhibitory and synapse onto the dorsal (ventral) muscles. The B-class motoneurons also receive proprioceptive feedback from the local body segment (inhibitory) and anterior segments (excitatory). The interneuron AVB is connected to VB and DB via gap-junctions, and the VB (DB) neurons are also coupled via gap-junctions with their nearest neighbors of the same class. The body wall is modeled as a viscoelastic material connected to a contractile muscle.

where  $x$  is the length-wise body coordinate,  $t$  is time,  $y(x, t)$  is the displacement in the ventral-dorsal plane,  $\kappa(x, t)$  is the curvature, and  $M(x, t)$  is the active moment that comes from internal muscle activity. The parameter  $k_b$  is the bending modulus,  $\mu_b$  is the effective internal viscosity, and the normal drag coefficient  $C_N$  is proportional to the external fluid viscosity  $\mu_f$  ( $C_N = \alpha\mu_f$ , see Appendix A.2). The values for these parameters are given in Table 2.1, and a discussion of how they were selected is provided in Chapter 2.3.

We consider small amplitude undulations, so that the curvature  $\kappa(x, t)$  is approximately the second spatial derivative of the displacements  $y(x, t)$ :

$$(2.2) \quad \kappa(x, t) \approx \partial_{xx}y(x, t).$$

Taking two partial derivatives in  $x$  of equation 2.1 and applying force-free, moment-free boundary conditions, the curvature  $\kappa(x, t)$  of the body satisfies

$$(2.3) \quad \alpha\mu_f\dot{\kappa} = -k_b\partial_{xxxx}\left(\kappa + \frac{\mu_b}{k_b}\dot{\kappa} + M(x, t)\right),$$

$$(2.4) \quad \kappa(x, t) + \frac{\mu_b}{k_b}\dot{\kappa}(x, t) + M(x, t) = 0, \quad \text{for } x = 0, x = L,$$

$$(2.5) \quad \partial_x\left(\kappa + \frac{\mu_b}{k_b}\dot{\kappa} + M(x, t)\right) = 0, \quad \text{for } x = 0, x = L,$$

where  $x = 0$  is the head and  $x = L$  is the tail ( $L$  is the body length). Note that in equations 2.3-2.5, a positive curvature  $\kappa(x, t)$  represents a bend towards the dorsal side. The active moment  $M(x, t)$  comes from internal muscle activity, which will be defined below.

**2.1.2. Muscles.** The body is driven by six modules of roughly 6 ventral and 6 dorsal muscle cells, that apply contractile forces to either the dorsal or ventral side [23, 58]. These muscle modules split the body into six distinct regions of length  $\ell = L/6$ . Each ventral/dorsal muscle group applies a contractile force as a function of its activity level  $A(t)$ . The ventral and dorsal ( $k = V, D$ ) muscle activities  $A_{k,j}$  in the  $j^{\text{th}}$  module are given by

$$(2.6) \quad \tau_m\dot{A}_{k,j} = -A_{k,j} + I_M(k, j),$$

where  $\tau_m$  is the timescale of muscle activation and  $I_M(k, j)$  is the input from the  $j^{\text{th}}$  neural module (described below). The tension  $\sigma(A(t))$  generated by the muscle is only contractile ( $\sigma \geq 0$ ) and saturates at some peak force  $c_m$ :

$$(2.7) \quad \sigma(A(t)) = \frac{c_m}{2}(\tanh(c_s(A(t) - a_0)) + 1),$$

where  $c_s, a_0$  define the scale and shift of the nonlinear threshold. In the  $j^{\text{th}}$  module, the dorsal and ventral muscles apply contractile forces to opposite sides of the body, which induces a moment

$m_j(t)$  on the centerline from  $x_{j-1} = (j-1)\ell$  to  $x_j = j\ell$ :

$$(2.8) \quad m_j(t) = \sigma(A_{V,j}(t)) - \sigma(A_{D,j}(t)).$$

The active moment  $M(x, t)$  as a function of the body coordinate  $x$  is then given by

$$(2.9) \quad M(x, t) = m_j(t) \text{ for } x \in [x_{j-1}, x_j].$$

**2.1.3. Neural Module.** The repeated neural module includes six motor neurons responsible for forward locomotion: DB (dorsal B-class), VB (ventral B-class), DD (dorsal D-class), and VD (ventral D-class) [5, 23, 58], as shown in Figure 2.1. The neural modules are similar in structure to Boyle et al. [5]. Each neural module is driven by constant input from the head interneuron AVB [23, 53, 58]. The D-class neurons are assumed to invert excitation from the B-class neurons into inhibition of the contralateral muscles. The B-class neurons are modeled as bistable, non-spiking elements, in line with recordings of similar motor neurons involved in head-turns [34]. The activities of the ventral and dorsal ( $k = V, D$ ) B-class neurons in the  $j^{\text{th}}$  neural module are given by

$$(2.10) \quad \tau_n \dot{V}_{k,j} = F(V_{k,j}) + P(k, j) + I_{gj}(k, j),$$

where

$$(2.11) \quad F(V_k) = V_k - aV_k^3 + I.$$

Here,  $\tau_n$  is the timescale of neural activity, and  $I$  is the offset from the constant “on” input from AVB, and  $a > 0$  is a parameter that controls the range of hysteresis. For simplicity, we generally use  $a = 1$ .  $P(k, j)$  is proprioceptive feedback into the neuron, and  $I_{gj}(k, j)$  is gap-junctional (electrical) coupling between neurons, both of which will be described below.

The D-class neurons are excited by the ipsilateral B-class neurons and inhibit the contralateral body-wall muscles. This effect is captured by direct inhibition of the muscles by the B-class neurons. We model the B-class neurons as exciting the ipsilateral muscles and inhibiting the contralateral

muscles. The input from the  $j^{\text{th}}$  neural module to the ventral/dorsal muscles is given by

$$(2.12) \quad I_M(k, j) = \begin{cases} V_{V,j} - V_{D,j}, & \text{if } k = V \\ V_{D,j} - V_{V,j}, & \text{if } k = D. \end{cases}$$

**2.1.4. Proprioceptive Feedback.** To close the neuromechanical loop, the body segment curvatures feed back into the circuit via proprioceptive processes in the VB and DB neurons. There are two types of proprioception in this model: local (from the body region covered by the muscles of the module) and nonlocal (from neighboring anterior body regions).

Local proprioceptive feedback acts to reset the neural modules, i.e., switch between dorsal bend commands and ventral bend commands. Thus, *local* proprioception is modeled as an excitatory current to the ventral B-class neurons in response to positive average curvature over the local module of length  $\ell = L/6$ , and an inhibitory current in response to negative average local curvature. The input to the dorsal B-class neurons is the same but with the polarities reversed. This feedback acts to relax the contracted muscles and contract the relaxed muscles.

Nonlocal proprioception promotes a wave of activity that propagates from anterior to posterior. The anatomical structures underlying proprioception are unknown [58], however, the evidence in Wen et al. [51] suggests that proprioceptive information affects the B-class motoneurons and is propagated posteriorly. In our model, positive nonlocal *anterior* segment curvature yields a weak inhibitory current to the ventral B-class neurons and a weak excitatory current to the dorsal B-class neurons. Negative nonlocal anterior segment curvature yields similar currents with the polarities reversed to each side. This is similar to the assumptions of Boyle et al. [5], but diverges in the directionality and sign of nonlocal proprioception.

The proprioceptive feedback to the ventral and dorsal B-class neurons in the  $j^{\text{th}}$  neural module ( $j = 1, \dots, 6$ ) of length  $\ell = L/6$  is modeled by

$$(2.13) \quad P(V, j) = +c_p \frac{1}{\ell} \int_{(j-1)\ell}^{j\ell} \kappa(x, t) dx - \varepsilon_p \frac{1}{\ell} \int_{(j-2)\ell}^{(j-1)\ell} \kappa(x, t) dx,$$

$$(2.14) \quad P(D, j) = -c_p \frac{1}{\ell} \int_{(j-1)\ell}^{j\ell} \kappa(x, t) dx + \varepsilon_p \frac{1}{\ell} \int_{(j-2)\ell}^{(j-1)\ell} \kappa(x, t) dx,$$

where  $c_p$  is the strength of *local* proprioception,  $\varepsilon_p$  is the strength of *nonlocal* anterior proprioception, and  $\kappa(x, t) = 0$  for  $x \notin [0, L]$  for notational simplicity.

**2.1.5. Gap-Junctional Coupling.** The B-class neurons are also connected via gap-junction synapses to neighboring B neurons of the same type (ventral/dorsal) [23,53,58]. The gap-junctions are modeled as symmetric ohmic resistors with constant conductance, so that the gap-junctional coupling to the ventral and dorsal ( $k = V, D$ ) B-class neurons in the  $j^{\text{th}}$  neural module are described by

$$(2.15) \quad I_{gj}(k, j) = \varepsilon_g(V_{k,j-1} - V_{k,j}) + \varepsilon_g(V_{k,j+1} - V_{k,j}),$$

where  $\varepsilon_g$  is the strength of gap-junction coupling and  $V_{k,0} = V_{k,7} = 0$  for notational simplicity.

## 2.2. Model Discretization for Numerical Simulation

To simulate the model described in Chapter 2.1, the body is discretized into six modules in correspondence with the six neuromuscular modules, so that there are six discrete body segment curvatures. The 4th-order difference operator  $D_4$  is used to approximate the 4th spatial derivative with zero-force, zero-torque boundary conditions:

$$(2.16) \quad \frac{1}{\ell^4} D_4 = \frac{1}{\ell^4} \begin{pmatrix} 7 & -4 & 1 & & & \\ -4 & 6 & -4 & 1 & & \\ 1 & -4 & 6 & -4 & 1 & \\ & 1 & -4 & 6 & -4 & 1 \\ & & 1 & -4 & 6 & -4 \\ & & & 1 & -4 & 7 \end{pmatrix}.$$

Discretizing equations 2.3-2.5 and using 2.8-2.9 yields a linear differential equation for the vector of body segment curvatures  $\underline{\kappa}$ :

$$(2.17) \quad \left( \alpha \mu_f I_6 + \frac{\mu_b}{\ell^4} D_4 \right) \dot{\underline{\kappa}} = -\frac{k_b}{\ell^4} D_4 (\underline{\kappa} + \sigma(\underline{\mathbf{A}}_V) - \sigma(\underline{\mathbf{A}}_D)),$$

where  $I_6$  is the  $6 \times 6$  identity matrix.



TABLE 2.1. Range of parameters explored and sources. See Chapter 2.3 for more details and Appendix A.2 for derivations.

Parameter	Name	Range of values	References
$L$	Body length	1 mm	[53]
$R$	Average body radius	40 $\mu\text{m}$	[9]
$r_{\text{cuticle}}$	Cuticle width	0.5 $\mu\text{m}$	[9]
$E$	Young's modulus	3.77 kPa - $1.3 \times 10^4$ kPa	[2, 15, 49]
$I_c$	Second moment of area of cuticle	$2.0 \times 10^{-7} (\text{mm})^4$	[9]
$k_b$	Bending modulus	$7.53 \times 10^{-10} - 2.6 \times 10^{-6} \text{ N} \cdot (\text{mm})^2$	[2, 15, 49]
$\mu_b$	Body viscosity	$2 \times 10^{-11} - 1.3 \times 10^{-7} \text{ N}(\text{mm})^2\text{s}$	[2, 15, 49]
$\mu_f$	Fluid viscosity	$1 - 2.8 \times 10^4 \text{ mPa}\cdot\text{s}$	[15]
$C_N$	Normal drag coefficient	$3.4\mu_f$	[9, 15]
$\tau_b$	Mechanical timescale $\tau_b = \mu_b/k_b$	1 ms - 5 s	[2, 15, 49]
$\tau_m$	Muscle activation timescale	50-200 ms	[35]

another. Of more importance in the model is the mechanical timescale

$$(2.24) \quad \tau_b = \frac{\mu_b}{k_b},$$

which is the timescale of relaxation in an inviscid fluid. In equation 2.24,  $k_b$  is the bending modulus, which is derived from the Young's modulus  $E$  and the geometry of the cuticle in Appendix A.2 following previous modeling procedures [10, 49]. Given the range of mechanical parameters reported in the literature, the mechanical timescale could be as small as  $\tau_b = 1$  ms or as large as  $\tau_b = 5$  s. The role of this timescale is explored in Chapter 2.4.2.

The electrophysiological details of the internal neural circuit are largely unknown, thus all the feedback and coupling strengths  $c_p, c_m, \varepsilon_p, \varepsilon_g$ , the parameters of the nonlinear functions  $F(V)$  and  $\sigma(A)$  are not well constrained. The feedback strengths  $c_m = 10$ ,  $c_p = 1$  and parameters of the nonlinear functions  $F(V)$  ( $a = 1, I = 0$ ) and  $\sigma(A)$  ( $c_s = 1, a_0 = 2$ ) were chosen so that the neuromechanical oscillator robustly gives the correct frequency ( $\sim 1.76\text{Hz}$ ) in a low-viscosity environment (see Chapter 4 for a more thorough exploration of these parameters). The values for the coupling parameters  $\varepsilon_p$  and  $\varepsilon_g$ , on the other hand, are explored in the next section.

## 2.4. Model Results

*C. elegans* locomote forward using alternating dorsal and ventral body bends that propagate in the form of a traveling wave from anterior to posterior. The spatial wavelength of this traveling

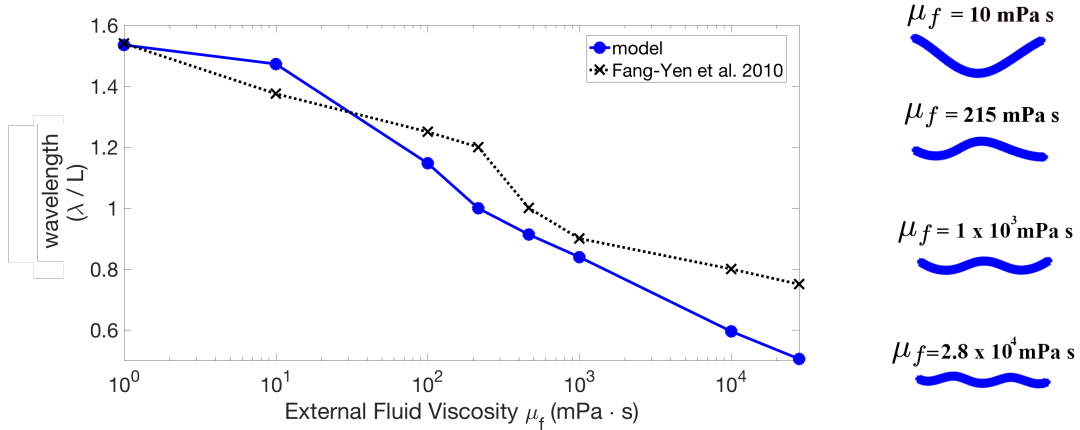


FIGURE 2.2. The model captures the quantitative trend of gait modulation seen in experiments such as [15]. Here,  $\tau_b = 0.5$  s,  $\tau_m = 0.1$  s, and  $\mu_b = 1.3 \times 10^{-7}$  N(mm)<sup>2</sup>s. In water ( $\mu_f = 1$  mPa s) the wavelength is roughly 1.5 bodylengths, and increasing the fluid viscosity  $\mu_f$  smoothly reduces the wavelength down to roughly 0.75 bodylengths in the most viscous case ( $\mu_f = 28$  Pa s).

wave changes in response to changes in the fluid viscosity [3, 15, 49]. In this section, we show that our model captures this gait adaptation for a wide range of mechanical and neural parameters, provided that the muscle response to input from the nervous system is faster than the body response to changes in internal and external forces.

**2.4.1. Model Captures Gait Adaptation.** We fit the model to match the wavelength and frequency in water, and then ran simulations in different fluid environments. Our model captures the quantitative effect of external fluid viscosity on the body wavelength seen in experiments and previous models. Figure 2.2 shows an example of the wavelength trend of the model for fixed body parameters  $\tau_b = 500$  ms,  $\tau_m = 50$ ms (the wavelengths were computed from the model output as described in Appendix A.1). Figure 2.2 also shows that the model wavelengths are in close quantitative agreement with the experimentally-measured wavelengths of Fang-Yen et al. [15]. In water ( $\mu_f = 1$  mPa·s) the wavelength is roughly 1.5 bodylengths, and increasing the fluid viscosity  $\mu_f$  smoothly reduces the wavelength down to roughly 0.75 bodylengths in the most viscous case ( $\mu_f = 2.8 \times 10^4$  mPa·s). This wavelength trend is similar to what has been observed in other experiments [3, 49], and in Chapter 2.4.2, we show that our model captures this trend robustly over a wide range of parameters.

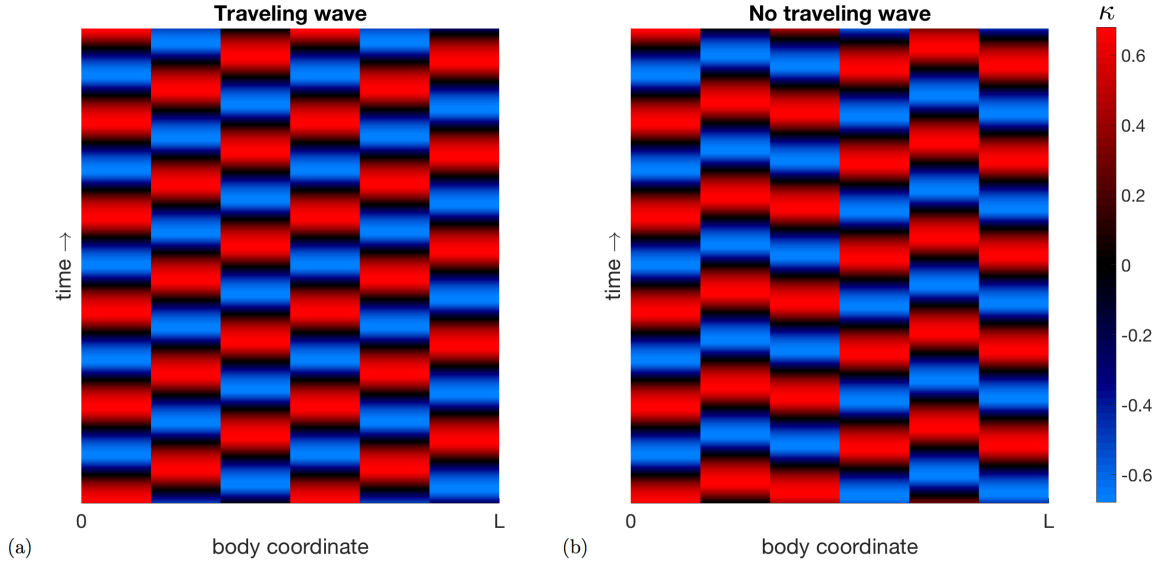


FIGURE 2.3. Sample model curvature kymographs (curvature vs. time) for various parameter regimes. For some parameter regimes, the gait adaptation trend generally held and there was a traveling wave at all  $\mu_f$  values; (a) gives an example of this behavior for  $\tau_b = 0.51$  s,  $\mu_b = 1.3 \times 10^{-7}$  N(mm<sup>2</sup>) s, and  $\mu_f = 28$  Pa s. For other parameter regimes, high enough external fluid viscosity  $\mu_f$  resulted in a loss of the traveling waveform; (b) gives an example of this behavior for  $\tau_b = 0.51$  s,  $\mu_b = 1.5 \times 10^{-9}$  N(mm<sup>2</sup>) s, and  $\mu_f = 28$  Pa s.

The undulation frequency also changes in response to changes in the fluid viscosity [3, 15, 49]. In Fang-Yen et al. [15], the frequency decreases from 1.7 Hz to 0.30 Hz as fluid viscosity increases from 1 mPa s to  $2.8 \times 10^4$  mPa s. Our model also exhibits a decrease in frequency as fluid viscosity  $\mu_f$  increases, but not of the same magnitude (1.7 Hz - 1.6 Hz). Discussion of this discrepancy is given in Chapter 7.

**2.4.2. Parameter Study Highlights Importance of Timescale Ordering in Capturing Gait Adaptation.** We performed a parameter study to show that the model robustly captures gait adaptation. For some parameter regimes, the body deformations were traveling waves for all fluid viscosities  $\mu_f$ , but this was not the case for other parameter regimes. Figure 2.3 shows kymographs of the body curvature that demonstrate two typical cases exhibited by the model.

The model parameters were systematically varied to characterize the model behavior. For a given body timescale  $\tau_b$  and body viscosity  $\mu_b$ , the muscle activity timescale  $\tau_m$  was selected in the range 50-250 ms to match the undulation frequency (1.7 Hz) in water ( $\mu_f = 1$  mPa s). Next,

the proprioceptive coupling strength  $\varepsilon_p$  was selected to match the wavelength (1.5 bodylengths) in water, and the gap-junctional coupling strength was fixed at  $\varepsilon_g = 0.0134$  (we examine the effects of varying the gap-junctional strength in the next subsection). The model was then run in different fluid viscosity  $\mu_f$  environments and the emergent coordination trend is reported in Figure 2.4. The model behavior was classified as either: (1) not a traveling wave for all fluid environments, (2) incorrect wavelength trend, (3) qualitatively correct wavelength trend, or (4) incorrect frequency in water.

There is no traveling wave (red triangles) if, for any viscosity  $\mu_f$ , the difference between the minimum and maximum pair-wise phase difference is greater than or equal to 0.5, because this indicates that there is no consistent directionality to the phase differences in the body. A range of observed wavelength trends in various parameter regimes (the boxed markers in Figure 2.4) are illustrated in Figure 2.5. Figure 2.5(a) and (b) show examples of the qualitatively correct wavelength trend (blue circles), while (c) shows the the incorrect trend, which was only obtained at a single parameter combination. The wavelength trend is incorrect because the wavelengths increased dramatically as the fluid viscosity increased, as opposed to generally decreasing.

A few key observations can be made from Figure 2.4. First, if the mechanical timescale  $\tau_b$  is too large, then the frequency in water cannot be obtained (see the black squares in Figure 2.4). Second, if the mechanical timescale  $\tau_b$  is too small, then there will not be a traveling wave for all fluid viscosities  $\mu_f$ . This suggests that while the body stiffness  $k_b$  and body viscosity  $\mu_b$  have been estimated across several orders of magnitude in various experiments and models, the effective mechanical body timescale  $\tau_b = \mu_b/k_b$  lies within the relatively narrow range 0.07 – 1 s.

In order to match the frequency, the muscle timescale  $\tau_m$  must be inversely related to  $\tau_b$ . When the body timescale  $\tau_b$  is increased, the muscle timescale  $\tau_m$  must decrease to compensate. The frequency in water cannot be obtained for  $\tau_b$  too large since it would require decreasing the muscle activity timescale  $\tau_m$  below physiological limits. Similarly, when the body timescale  $\tau_b$  is decreased, the muscle timescale  $\tau_m$  must be increased to compensate for the frequency. For  $\tau_b$  too small, there is not a traveling wave for all fluid viscosities  $\mu_f$ ; this occurs soon after  $\tau_b < \tau_m$ . This suggests that the relative ordering of the timescales  $\tau_b, \tau_m, \tau_n$  is key to the coordination. Generally, the mechanical timescale  $\tau_b$  must be the largest, the muscle activity timescale  $\tau_m$  intermediate,

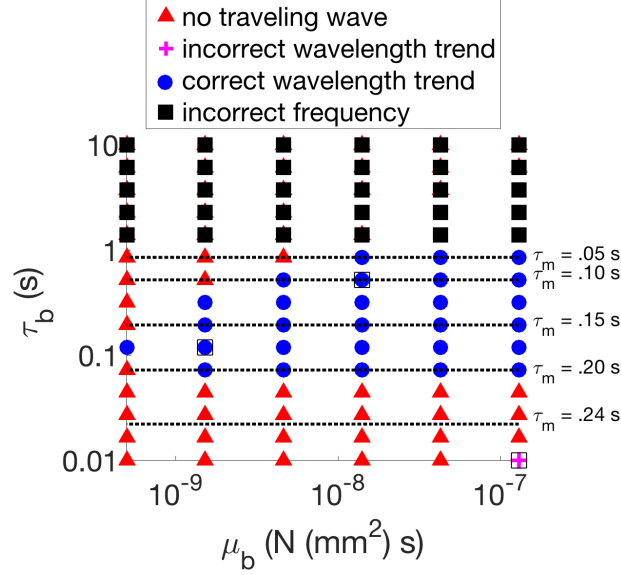


FIGURE 2.4. Classification of the model behavior for different mechanical parameters  $\mu_b$  and  $\tau_b$ . For each parameter combination  $(\mu_b, \tau_b)$ , the muscle timescale  $\tau_m$  was fit to match the undulation frequency in water ( $\tau_m$  contours shown in black dashes). Boxed markers indicate parameter combinations which have the wavelength trend illustrated in Figure 2.5.

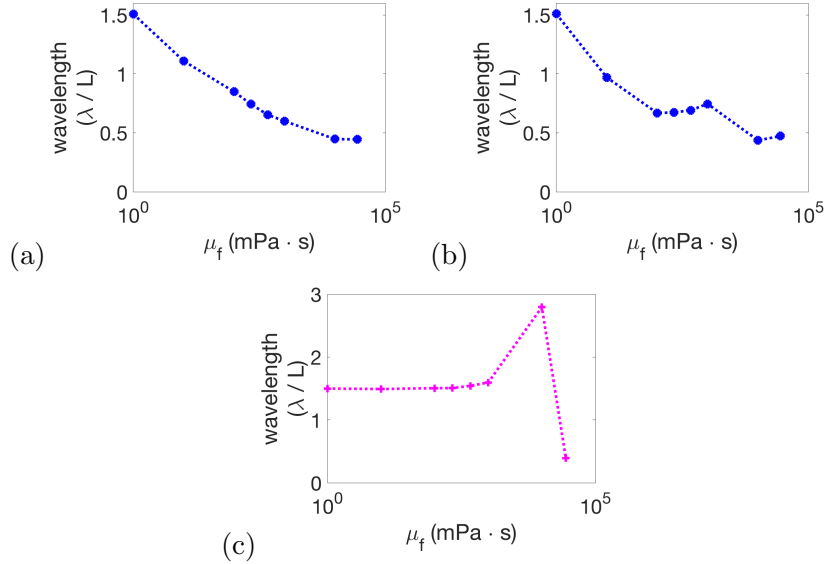


FIGURE 2.5. Model wavelength vs. external fluid viscosity  $\mu_f$  for various parameter regimes (the boxed markers in Figure 2.4). (a) and (b) show examples of the qualitatively correct wavelength trend, while (c) shows an incorrect trend. (a) has  $\tau_b = 0.51$  s ,  $\mu_b = 1.4 \times 10^{-8}$  N(mm<sup>2</sup>)s, (b) has  $\tau_b = 0.12$  s ,  $\mu_b = 1.5 \times 10^{-9}$  N(mm<sup>2</sup>)s, and (c) has  $\tau_b = 0.01$  s ,  $\mu_b = 1.3 \times 10^{-7}$  N(mm<sup>2</sup>)s.

and the neural timescale  $\tau_n$  the shortest. The mechanism by which this timescale ordering affects coordination is explained in Chapter 3.3.

Remarkably, whenever there is a traveling wave in this systematic parameter search, it almost always has the qualitatively correct wavelength trend. This wavelength trend is consistent with gait adaptation across several orders of magnitude of the mechanical parameters.

**2.4.3. Role of Neural Coupling.** In the parameter study of the previous subsection, we fixed the gap-junctional coupling strength  $\varepsilon_g$  and then chose the proprioceptive coupling strength  $\varepsilon_p$  in order to match the wavelength in water (1.54 bodylengths). Here, we vary the gap-junctional coupling strength  $\varepsilon_g$  to examine the role of neural coupling more thoroughly. We fix the parameters  $\tau_b = 0.5$  s,  $\tau_m = 0.1$  s, and  $\mu_b = 1.3 \times 10^{-7}$  N(mm)<sup>2</sup>s, vary the gap-junctional coupling strength  $\varepsilon_g$ , and solve for the proprioceptive coupling strength  $\varepsilon_p$  to match the wavelength in water (1.5 bodylengths). The resulting proprioceptive coupling strengths  $\varepsilon_p$  fit for each gap-junctional coupling strength  $\varepsilon_g$  are shown in Figure 2.6(a). Larger proprioceptive coupling strengths  $\varepsilon_p$  are needed in order to match the wavelength in water for larger gap-junctional coupling strengths  $\varepsilon_g$ , and for small gap-junctional coupling strengths ( $\varepsilon_g < 0.1$ ), the relationship is approximately linear ( $\varepsilon_p \approx 2.7\varepsilon_g$ ).

Figure 2.6(b) shows the resulting wavelength trend of the model for different gap-junctional coupling strengths  $\varepsilon_g$  (with the resulting proprioceptive coupling strengths  $\varepsilon_p$ ). The wavelength trends are generally flatter for larger gap-junctional coupling strengths  $\varepsilon_g$ . At larger gap-junctional coupling strengths  $\varepsilon_g$ , the steep transition from long wavelengths (1.5 bodylengths) to shorter wavelengths occurs at higher fluid viscosities  $\mu_f$ . The experimentally-observed wavelength trend of Fang-Yen et al. [15] (shown in X's and black-dotted lines in Figure 2.6(b)) is more closely matched by  $\varepsilon_g \in [0.02, 0.05]$ . In the previous subsection's parameter study, we used  $\varepsilon_g = 0.0134$ , which is near this range of gap-junctional coupling strengths.

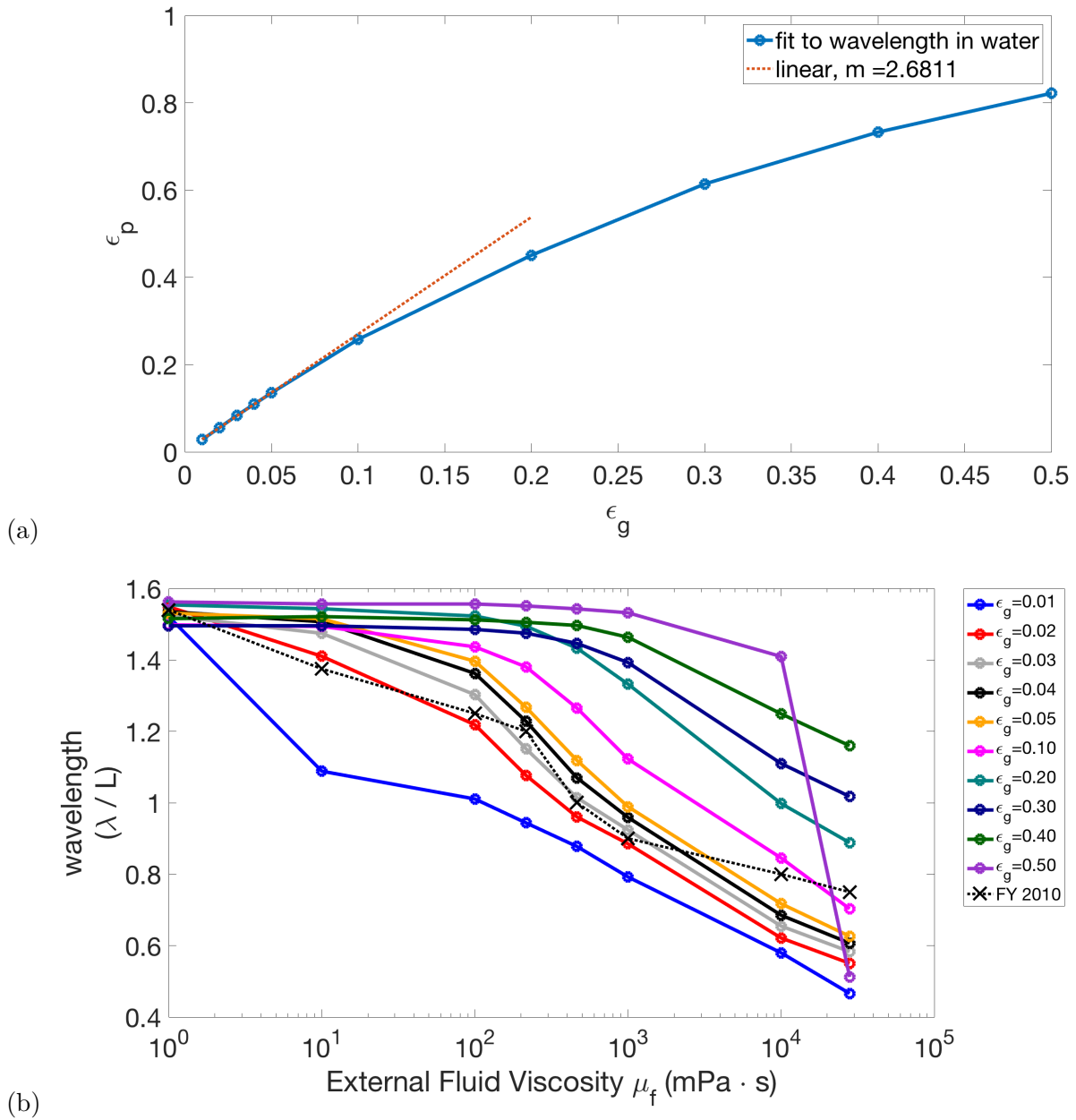


FIGURE 2.6. (a) The proprioceptive coupling strengths  $\epsilon_p$  that were found for each  $\epsilon_g$  in order to match the wavelength in water. Note that for small gap-junctional coupling strengths ( $\epsilon_g < 0.1$ ), the relationship is approximately linear ( $\epsilon_p \approx 2.7\epsilon_g$ ). (b) For each  $\epsilon_g$ , the resulting wavelengths of the model vs. external fluid viscosity  $\mu_f$ .

## Phase Model: Insight Into Mechanisms Underlying Gait Adaptation

The neuromechanical model is able to robustly capture the quantitative trend of gait adaptation across a wide range of parameters. In this chapter, the modular structure of the model will be exploited to uncover the fundamental mechanisms underlying gait adaptation. The isolated, uncoupled neuromechanical modules are intrinsic neuromechanical oscillators. These modules form a network of coupled oscillators with three forms of coupling: mechanical (through the body and external fluid), proprioceptive, and gap-junctional. Furthermore, this coupling is relatively weak, and thus the theory of weakly coupled oscillators can be applied to identify the coordinating effects of each coupling modality. We demonstrate that the competition between mechanical coupling and neural coupling provides an explicit mechanism for gait adaptation.

### 3.1. Isolated Neuromechanical Modules are Intrinsic Oscillators

A single, isolated neuromechanical module is defined as a neural subcircuit, the corresponding muscles and body section, and local proprioceptive feedback (without coupling through the body or neural circuitry). The dynamics for this isolated module is governed by

$$(3.1) \quad \dot{\kappa} = -\frac{1}{\tau_b}(\kappa + \sigma(A_V) - \sigma(A_D)),$$

$$(3.2) \quad \dot{A}_V = \frac{1}{\tau_m}(-A_V + V_V - V_D),$$

$$(3.3) \quad \dot{A}_D = \frac{1}{\tau_m}(-A_D + V_D - V_V),$$

$$(3.4) \quad \dot{V}_V = \frac{1}{\tau_n}(F(V_V) + c_p\kappa),$$

$$(3.5) \quad \dot{V}_D = \frac{1}{\tau_n}(F(V_D) - c_p\kappa).$$

Note that this is the model described in Chapter 2, omitting the intermodular coupling. The isolated modules exhibit robust oscillations over a wide range of parameters, and a single period of the module is shown for each state-variable in Figure 3.1(a). Thus, the neuromechanical modules are intrinsic oscillators, wherein each B-class neuron promotes either a dorsal or ventral bend and the local proprioceptive feedback acts to switch the bistable B neurons from one state to the other. The basic cycle of the oscillator is as follows: when activated, the ventral B-class neuron ( $V_V$ ) excites the ventral muscles which build up activity ( $A_V$ ) to induce a ventral bend (negative  $\kappa$ ); when the curvature  $\kappa$  is sufficiently large, the local proprioceptive feedback deactivates the ventral B-class neuron and activates the dorsal B-class neuron, and the cycle continues towards a dorsal bend.

The system of six identical, uncoupled neuromechanical oscillators is described by

$$(3.6) \quad \dot{\underline{\mathbf{X}}}_j = S(\underline{\mathbf{X}}_j), \quad j = 1, \dots, 6$$

where

$$(3.7) \quad \underline{\mathbf{X}}_j = [\kappa_j, A_{V,j}, A_{D,j}, V_{V,j}, V_{D,j}]^T,$$

and  $S(\underline{\mathbf{X}})$  is given by equations 3.1-3.5. The oscillations correspond to a  $T$ -periodic limit cycle  $\underline{\mathbf{X}}^{LC}(t)$  in  $(\kappa, A_V, A_D, V_V, V_D)$ -state-space. This limit cycle can be parametrized by phase

$$(3.8) \quad \theta_j = (\omega t + \theta_j^0) \bmod 1$$

with the initial phase  $\theta_j^0 \in [0, 1)$ . As  $\theta_j$  increases at a constant rate  $\omega = 1/T$ ,  $\underline{\mathbf{X}}^{LC}(\theta_j)$  traces out the limit cycle through state-space and the state of each oscillator on the limit cycle is given by

$$(3.9) \quad \underline{\mathbf{X}}_j(t) = \underline{\mathbf{X}}^{LC}(\theta_j),$$

where the only distinguishing feature between the oscillators is their unique phase  $\theta_j$ . Figure 3.1(a) shows the components of  $\underline{\mathbf{X}}^{LC}(\theta)$ .

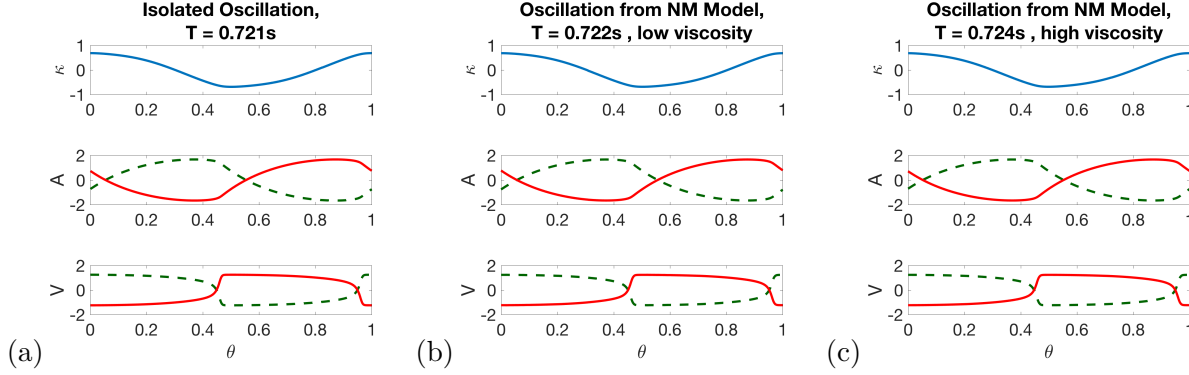


FIGURE 3.1. The period and amplitude of the oscillations in  $\kappa, A_V, A_D, V_D, V_V$  are all relatively similar for (a) the single, isolated neuromechanical module, (b) the single module in the full neuromechanical model at low viscosity ( $\mu_f = 1\text{mPa s}$ ), and (c) the single module in the full neuromechanical model at high viscosity ( $\mu_f = 2.8 \times 10^4 \text{mPa s}$ ). Ventral neural/muscle activities are given in green dashed lines, dorsal neural/muscle activities are given in red solid lines.

### 3.2. Network of Coupled Oscillators

Rearranging equations 2.17-2.23, the neuromechanical model can be written as a network of coupled oscillators:

$$(3.10) \quad \dot{\underline{\mathbf{X}}}_j = S(\underline{\mathbf{X}}_j) + C_j(\underline{\mathbf{X}}_1, \dots, \underline{\mathbf{X}}_6), \quad j = 1, \dots, 6$$

where  $C_j(\underline{\mathbf{X}}_1, \dots, \underline{\mathbf{X}}_6)$  describes the coupling dynamics from all the modules to the  $j^{\text{th}}$  module through gap-junctions, nonlocal proprioception, and body mechanics:

$$(3.11) \quad C_j(\underline{\mathbf{X}}_1, \dots, \underline{\mathbf{X}}_6) = \begin{bmatrix} \varepsilon_m \sum_{k=1}^6 (D_4^{-1})_{jk} \dot{\kappa}_k, \\ 0, \\ 0, \\ \frac{1}{\tau_n} \sum_{k=1}^6 \varepsilon_p (W_p)_{jk} \kappa_k + \varepsilon_g (W_g)_{jk} V_{V,k}, \\ \frac{1}{\tau_n} \sum_{k=1}^6 -\varepsilon_p (W_p)_{jk} \kappa_k + \varepsilon_g (W_g)_{jk} V_{D,k} \end{bmatrix}.$$

The parameter  $\varepsilon_m = \alpha \mu_f \ell^4 / \mu_b$  is the effective mechanical coupling strength.

The intrinsic oscillations of the isolated module (equations 3.1-3.5) in Figure 3.1(a) are almost indistinguishable in both frequency and amplitude to the oscillations in Figure 3.1(b,c) of a module within the fully-coupled network (equations 2.17-2.21) at both low and high external fluid viscosity

$\mu_f$ . Furthermore, Figure 3.1(b,c) show that the change in oscillator period between the low and high viscosity cases is  $\Delta T/T < 0.003$ , so the change in frequency as external fluid viscosity  $\mu_f$  is varied is small. This suggests that the coupling dynamics are “weak” relative to the intrinsic oscillatory dynamics.

Because the coupling is weak, the theory of weakly coupled oscillators can be applied (see Appendix C or [44] for details). The coupling only alters the phase of the oscillators on their respective limit cycles and the effect on amplitude is negligible, therefore the phase completely describes the state of a neuromechanical module. Equation 3.10 can be reduced to the so-called phase equations, a set of differential equations describing the evolution of the phases of each oscillator:

$$(3.12) \quad \dot{\theta}_j = \omega_j + \sum_{k=1}^6 \varepsilon_m (D_4^{-1})_{jk} H_m(\theta_k - \theta_j) + \varepsilon_g (W_g)_{jk} H_g(\theta_k - \theta_j) + \varepsilon_p (W_p)_{jk} H_p(\theta_k - \theta_j),$$

where  $\theta_j$  is the phase of the  $j^{\text{th}}$  oscillator,  $\omega$  is the intrinsic frequency, and  $H(\phi)$  are the interaction functions that describe the change in frequency (resulting from either mechanical, proprioceptive, or gap-junction coupling) as a function of the phase difference  $\phi = \theta_k - \theta_j$  of a given pair of oscillators:

$$(3.13) \quad H_m(\phi) = -\frac{1}{T} \int_0^T Z_\kappa(t) \dot{\underline{\kappa}}^{LC}(t - \phi) dt,$$

$$(3.14) \quad H_p(\phi) = \frac{1}{\tau_n} \frac{1}{T} \int_0^T Z_{V_V}(t) \underline{\kappa}^{LC}(t - \phi) - Z_{V_D}(t) \underline{\kappa}^{LC}(t - \phi) dt,$$

$$(3.15) \quad H_g(\phi) = \frac{1}{\tau_n} \frac{1}{T} \int_0^T Z_{V_V}(t) (\underline{\mathbf{V}}^{LC}(t - \phi) - \underline{\mathbf{V}}^{LC}(t)) + Z_{V_D}(t) (\underline{\mathbf{D}}^{LC}(t - \phi) - \underline{\mathbf{D}}^{LC}(t)) dt.$$

Here,  $Z_\kappa(t)$ ,  $Z_{V_V}(t)$ ,  $Z_{V_D}(t)$  are the  $T$ -periodic phase response functions to perturbations in the corresponding state variable.

The coupling modalities define the *structure* of the interaction functions, through the state variables that are coupled, as well as the coupling topology (the connectivity matrices  $D_4^{-1}$ ,  $W_g$ , and  $W_p$  in equation 3.12). Note that there is a separate H-function for each of the three coupling

modalities and these three coupling modalities add linearly to produce the full interaction of the modules. Therefore, the relative contributions of the various coupling types can be analyzed independently through varying the different coupling strengths: fluid viscosity  $\mu_f$  (through  $\varepsilon_m$ ) for mechanical,  $\varepsilon_p$  for proprioceptive, and  $\varepsilon_g$  for gap-junctional.

### 3.3. Two-Oscillator Analysis Explains the Coordination Mechanism

Analyzing a pair of two coupled oscillators gives considerable insight into the coordination that each coupling modality produces separately and the mechanisms of coordination. With only two oscillators, the phase model reduces to

$$(3.16) \quad \dot{\theta}_1 = \omega + \varepsilon_m \sum_{j=1}^2 (D_4^{-1})_{1j} H_m(\theta_j - \theta_1) + \varepsilon_g H_g(\theta_2 - \theta_1),$$

$$(3.17) \quad \dot{\theta}_2 = \omega + \varepsilon_m \sum_{j=1}^2 (D_4^{-1})_{2j} H_m(\theta_j - \theta_2) + \varepsilon_p H_p(\theta_1 - \theta_2) + \varepsilon_g H_g(\theta_1 - \theta_2).$$

In the two oscillator case, the matrix  $D_4^{-1}$  is symmetric, so  $(D_4^{-1})_{12} = (D_4^{-1})_{21} = d_{12}$ . By defining

$$(3.18) \quad \phi = \theta_2 - \theta_1,$$

and subtracting equation 3.16 from equation 3.17, the dynamics of the two oscillator system can be described by a single differential equation for the phase difference between the two oscillators:

$$(3.19) \quad \dot{\phi} = \varepsilon_m d_{12} G_m(\phi) + \varepsilon_p G_p(\phi) + \varepsilon_g G_g(\phi) = G(\phi),$$

where  $G_m(\phi) = H_m(-\phi) - H_m(\phi)$ ,  $G_p(\phi) = H_p(-\phi)$ , and  $G_g(\phi) = H_g(-\phi) - H_g(\phi)$  are the pairwise interaction functions, or *G-functions* of the pair. The stable phase-locked state of the system  $\phi^*$  is given by  $G(\phi^*) = 0$ ,  $G'(\phi^*) < 0$ .

**3.3.1. Each Coupling Modality Promotes a Different Coordination Outcome.** Figure 3.2 shows the G-functions and corresponding phase-locked states of the different coupling modalities. For mechanical coupling alone, i.e.,  $\varepsilon_p = \varepsilon_g = 0$ , the stable phase-locked state is anti-phase ( $\phi^* = 0.5$ ), since  $G(0.5) = 0$  and  $G'(0.5) < 0$  (Figure 3.2(a)). Similarly, for proprioceptive coupling

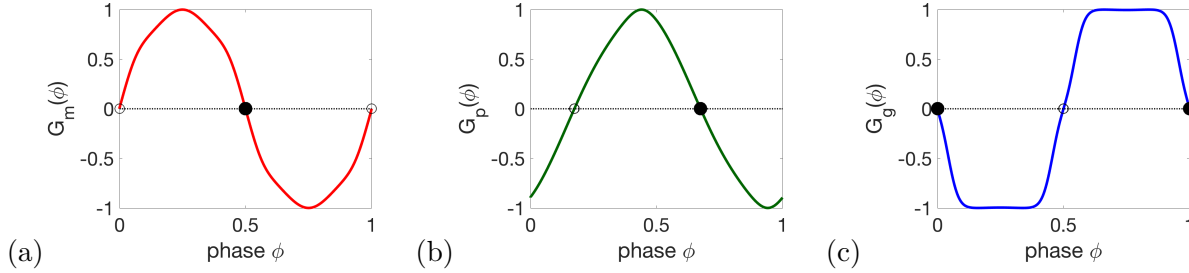


FIGURE 3.2. Each coupling modality promotes a different coordination outcome in a pair of coupled neuromechanical oscillators based on the stable zero of the corresponding G-function: (a) mechanical coupling promotes antiphase since  $G_m(0.5) = 0$  and  $G'_m(0.5) < 0$ ; (b) proprioceptive coupling promotes a phase-wave since  $G_p(0.75) = 0$  and  $G'_p(0.75) < 0$ ; and (c) gap-junctional coupling promotes synchrony since  $G_g(1) = 0$  and  $G'_g(1) < 0$ .

alone, the stable state is an intermediate phase-difference ( $\phi^* \approx 0.75$ , Figure 3.2(b)), so the first oscillator leads the second (front-to-back). For gap-junctional coupling alone, the stable state is synchrony ( $\phi^* = 0$ , Figure 3.2(c)).

The coordination outcome with all three coupling mechanisms present corresponds to the zero of the G-function (equation 3.19), which is a weighted sum of the three individual G-functions. Thus, coordination can be examined in the context of this weighted sum as the three coupling strengths are varied: external fluid viscosity  $\mu_f$  for mechanical coupling, proprioceptive coupling strength  $\varepsilon_p$ , and gap-junction coupling strength  $\varepsilon_g$ .

**3.3.2. Neural Coupling Sets the Low-Viscosity Wavelength.** The stable phase difference  $\phi^*$  of the pair of the neuromechanical oscillators can be used to define a wavelength in the full body (for details see Appendix A.1):

$$(3.20) \quad \frac{\lambda}{L} = \frac{1}{6(1 - \phi^*)}.$$

In the low external fluid viscosity case ( $\mu_f = 1$  mPa·s), setting  $\varepsilon_p = 0.05, \varepsilon_g = 0.01$  as in Chapter 2.4.2 provides a good approximation of the experimentally observed wavelength for the mechanical parameters  $k_b = 2.6 \times 10^{-7}$  N (mm)<sup>2</sup>,  $\mu_b = 1.3 \times 10^{-7}$  N (mm)<sup>2</sup> s. For these parameters,

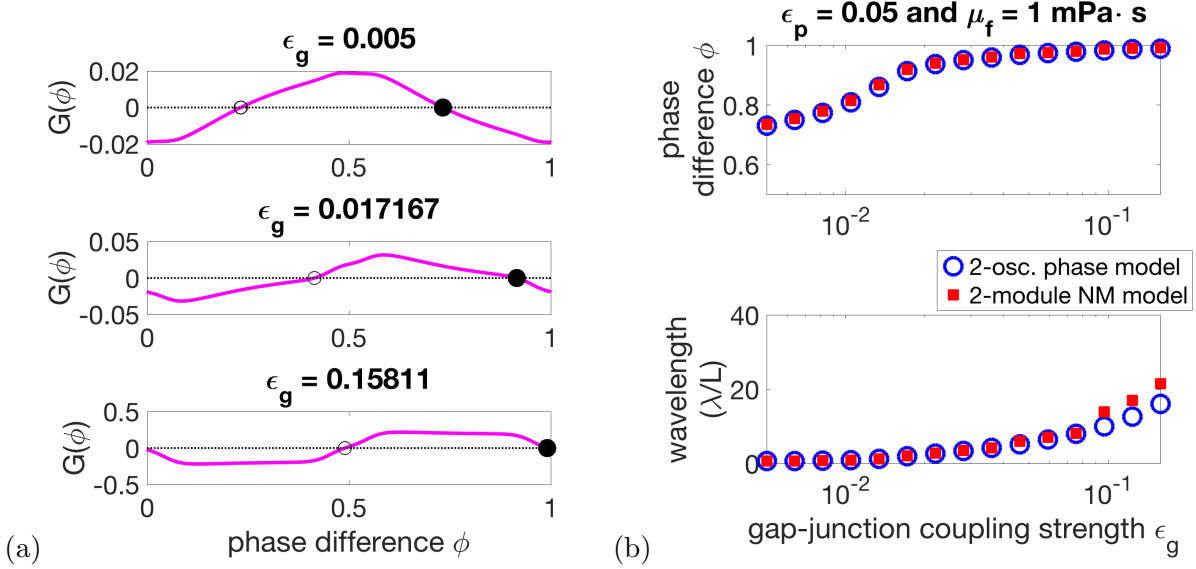


FIGURE 3.3. In the low-viscosity limit, the stable phase-locked states of the pair of neuromechanical oscillators is set by the competition between proprioceptive and gap-junctional coupling. (a) The linear combination of the  $G$ -functions given by equation 3.19 for  $\varepsilon_p = 0.05$ ,  $\mu_f = 1$  mPa·s, and various  $\varepsilon_g$ . Note that as the gap-junctional coupling strength  $\varepsilon_g$  increases, the stable phase-locked phase difference  $\phi^*$  moves from roughly  $\phi^* = 0.75$  towards  $\phi^* = 1$ . (b) The stable phase-locked states of the pair can be tuned by varying the two forms of neural coupling: proprioceptive and gap-junctional. When proprioceptive coupling dominates, the stable phase-locked state is a phase difference of roughly  $\phi^* = 0.75$ , and when gap-junctional coupling dominates, the stable phase-locked state is synchrony  $\phi^* = 1$ . The resulting wavelength in the body, if the pair-wise phase difference was constant in the six-oscillator model, can be tuned by varying the two forms of neural coupling: proprioceptive and gap-junctional. When proprioceptive coupling dominates, the wavelength is roughly 0.75 bodylengths, and when gap-junctional coupling dominated, the wavelength is infinite, since each oscillator pair is in perfect synchrony and thus the body is a standing wave.

the relative sizes of the  $G$ -functions in equation 3.19 are

$$(3.21) \quad \varepsilon_m d_{12} \max |G_m(\phi)| = 3.532 \times 10^{-5},$$

$$(3.22) \quad \varepsilon_p \max |G_p(\phi)| = 2.016,$$

$$(3.23) \quad \varepsilon_g \max |G_g(\phi)| = 1.259.$$

Thus, at low viscosity, mechanical coupling is almost negligible compared to neural coupling, so the coordination is determined by proprioceptive and gap-junctional coupling.

How the wavelength is set in this low-viscosity case can be examined by varying the neural coupling strengths. Figure 3.3(a) shows that as the gap-junctional coupling strength  $\varepsilon_g$  is increased relative to the proprioceptive coupling strength, the phase-locked states move from close to the zeros of  $G_p(\phi)$  towards the zeros of  $G_g(\phi)$ . Figure 3.3(b) shows that when proprioceptive coupling dominates, the stable phase-locked state corresponds to a phase difference of roughly  $\phi^* \approx 0.75$  and corresponds to a wavelength of 0.75 bodylengths according to equation 3.20. When gap-junctional coupling dominates, the stable phase-locked state is close to synchrony  $\phi^* \approx 1$ , which corresponds to an infinite wavelength in the full body if this phase difference was constant. In this gap-junction-dominated case, each pair is in perfect synchrony and the body exhibits a standing wave.

To assess the predictive power of the two-oscillator phase model, a simulation of the neuromechanical model with only two modules was performed alongside the phase model. Figure 3.3(b) shows that the two-oscillator phase model is quantitatively accurate when compared to the phase differences and wavelengths derived from this two-module simulation. Thus, neural coupling sets the low-viscosity wavelength in the two-module neuromechanical model as well.

**3.3.3. Competition Between Mechanical and Neural Coupling Provides a Mechanism for Gait Adaptation.** To examine the effect of mechanical coupling in the two-oscillator phase model, the neural coupling parameters are fixed to  $\varepsilon_p = 0.05$  and  $\varepsilon_g = 0.0134$  so that the wavelength in the low-viscosity case is roughly 1.5 bodylengths. The strength of mechanical coupling is increased in equation 3.19 by increasing the external fluid viscosity  $\mu_f$ . Figure 3.4(a) shows that as the strength of mechanical coupling is increased, the phase-locked states move from close to the zeros set by  $\varepsilon_p G_p(\phi) + \varepsilon_g G_g(\phi)$  towards the zeros of  $G_m(\phi)$ . Figure 3.4(b) shows how the stable phase-locked state changes as a function of the mechanical coupling strength  $\mu_f$ . When neural coupling dominates, the stable phase-locked state is a phase difference of roughly  $\phi^* \approx 0.89$ , and when mechanical coupling dominates, the stable phase-locked state is antiphase  $\phi^* = 0.5$ . Similarly, Figure 3.4(b) shows that when neural coupling dominates the resulting wavelength (according to equation 3.20) is roughly 1.5 bodylengths, and when mechanical coupling dominates the wavelength is roughly 0.45 bodylengths.

This analysis shows that gait adaptation is a result of competition between mechanical and neural coupling. The decrease in wavelength as external viscosity  $\mu_f$  increases is explained by the

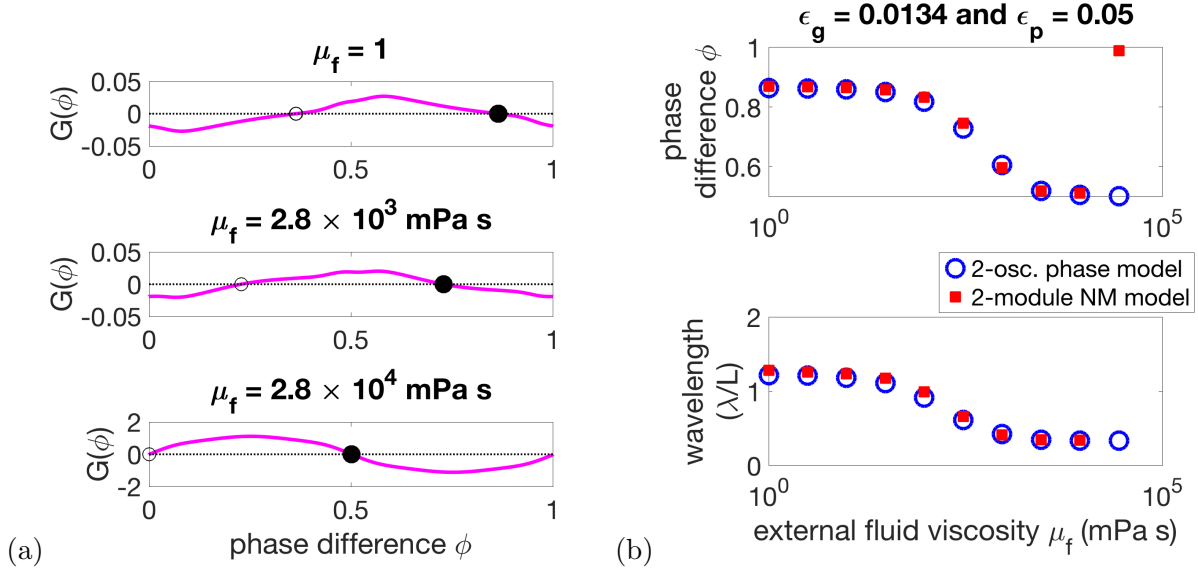


FIGURE 3.4. Gait adaptation is a result of the competition between mechanical and neural coupling in the pair of neuromechanical oscillators. (a) The linear combination of the G-functions given by equation 3.19 for  $\epsilon_p = 0.05$ ,  $\epsilon_g = 0.0134$ , and various  $\mu_f$ . Note that as  $\mu_f$  increases, the strength of mechanical coupling increases and the stable phase-locked phase difference  $\phi^*$  moves from roughly  $\phi^* = 0.8$  towards  $\phi^* = 0.5$ . (b) When neural coupling dominates, the stable phase-locked state is a phase difference of roughly  $\phi^* = 0.88$ , and when mechanical coupling dominates, the stable phase-locked state is antiphase, i.e.,  $\phi^* = 0.5$  phase difference. The resulting wavelength in the body, if the pair-wise phase difference was constant in the six-oscillator model, is set by the competition between the mechanical and neural coupling. When neural coupling dominates, the wavelength is roughly 1.5 bodylengths, and when mechanical coupling dominates, the wavelength is roughly 0.45 bodylengths.

increased strength in mechanical coupling and its associated coordination outcome, antiphase. The two-oscillator phase model is quantitatively accurate when compared to phase differences derived from the neuromechanical model with two modules, as shown in Figure 3.4(b). Thus, this suggests that the mechanism underlying the behavior in the two-module neuromechanical model is the same as the mechanism of the phase model outlined here. However, note that the phase difference at the highest fluid viscosity ( $\mu_f = 2.8 \times 10^4$  mPa s) is different between the two-oscillator phase model and the full two-module neuromechanical model. This indicates the limit of weak coupling, as the phase reduction is not able to capture the transition to synchrony seen in the two-module neuromechanical model. However, weak coupling holds in the two-oscillator case for the rest of the

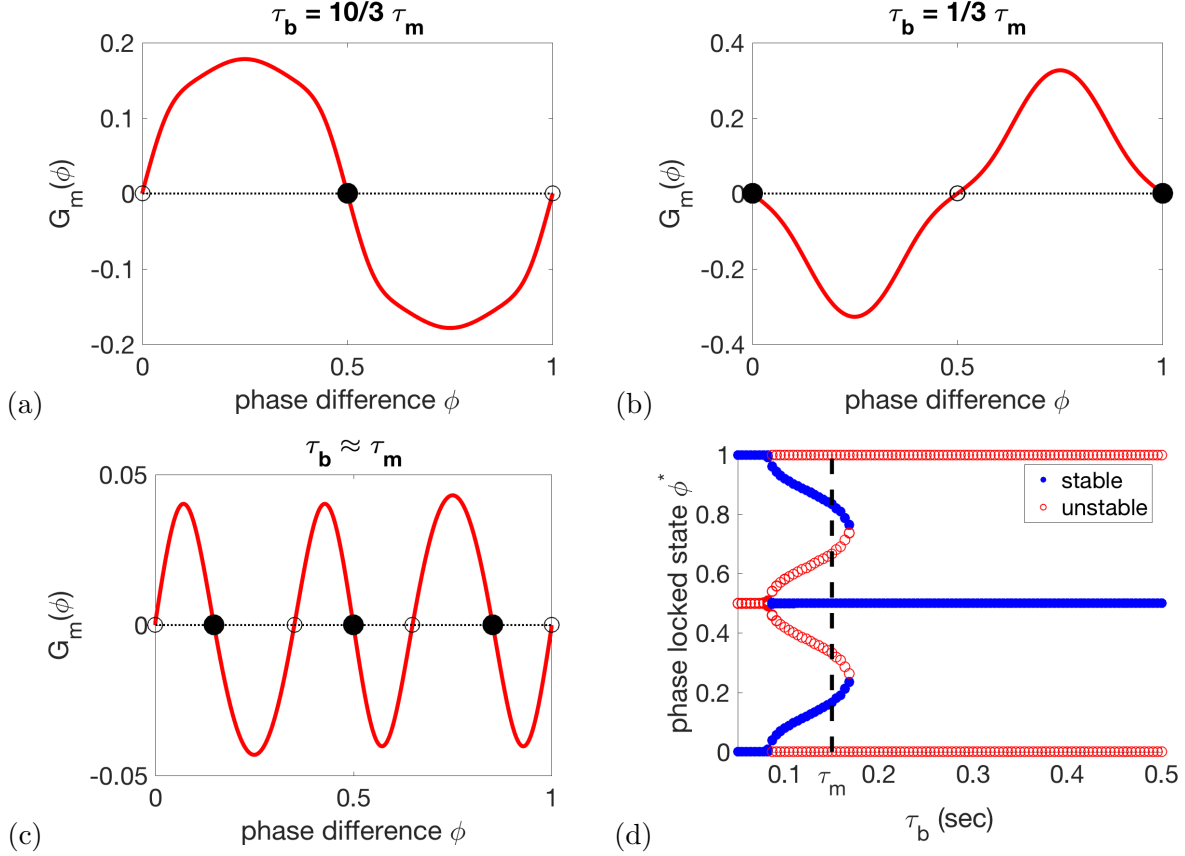


FIGURE 3.5. (a) Mechanical G-function  $G_m(\phi)$  for the pair of neuromechanical oscillators when  $\tau_b$  is sufficiently larger than  $\tau_m$  ( $\tau_b = 0.5$  s,  $\tau_m = 0.15$  s). Note the stable phase-locked state is antiphase since  $G_m(0.5) = 0$  and  $G'_m(0.5) < 0$ . (b) Mechanical G-function  $G_m(\phi)$  for the pair when  $\tau_b$  is sufficiently smaller than  $\tau_m$  ( $\tau_b = 0.05$  s,  $\tau_m = 0.15$  s). Note the stable phase-locked state is synchrony since  $G_m(1) = 0$  and  $G'_m(1) < 0$ , while antiphase is unstable since  $G'_m(0.5) > 0$ . (c) Mechanical G-function  $G_m(\phi)$  for the pair when  $\tau_b \approx \tau_m$  ( $\tau_b = 0.14$  s,  $\tau_m = 0.15$  s). (d) Bifurcation diagram for the phase-locked states  $\phi^*$  of the mechanical G-function vs.  $\tau_b$ , for  $\tau_m = .15$  s.

viscosities  $\mu_f$  considered. Furthermore, this transition to synchrony is not seen in the six-module neuromechanical model.

**3.3.4. Phase Reduction Gives Insight into Timescale Ordering.** The phase reduction also explains why generally  $\tau_b$  must be larger than  $\tau_m$  in order to obtain the correct coordination trend (as described in Chapter 2.4.2). The results in the previous subsection indicate that it is important for mechanical coupling to promote antiphase in order to get the correct wavelength trend as external viscosity  $\mu_f$  is increased. Figure 3.5(a) shows that, when  $\tau_b$  is sufficiently larger

than  $\tau_m$ , the stable zero of  $G_m$  is 0.5, i.e., the stable phase-locked state is antiphase. However, when  $\tau_b$  is sufficiently smaller than  $\tau_m$ , the stable zero of  $G_m$  is 0, i.e., the G-function is flipped and mechanical coupling promotes synchrony. In this case, the wavelength trend as external viscosity  $\mu_f$  is increased is incorrect, since increasing the mechanical coupling strength would pull the oscillators towards synchrony, lengthening the wavelength instead of shortening it.

The shift in the stabilities of the phase-locked states from antiphase to synchrony is somewhat complicated, as Figure 3.5(c) shows that  $\tau_b \approx \tau_m$  can yield tristable phase-locked states. A series of paired saddle-node bifurcations and paired super- and sub-critical pitchfork bifurcations (Figure 3.5D), marks the transition from stable antiphase to tristability to stable synchrony as  $\tau_b$  moves below  $\tau_m$ . The change in the stability of the antiphase state promoted by mechanical coupling is the cause of the rapid change in coordination in Figure 2.4 as  $\tau_b$  becomes sufficiently smaller than  $\tau_m$ .

### 3.4. Mechanism for Gait Adaptation Holds in Six-Oscillator Case

We simulate the six-oscillator phase model in order to (i) assess the predictive power of the phase model by a quantitative comparison to the full six-module neuromechanical model and (ii) determine whether the mechanism of gait adaptation analyzed in the two-module case extends to the full six-module case.

Figure 3.6(a) shows the wavelengths for the six-oscillator phase model (line, circles) and neuromechanical model (crosses) as a function of external fluid viscosity  $\mu_f$  for  $\varepsilon_p = 0.05$  and  $\varepsilon_g = 0.017$  (these coupling strengths were chosen so that the water-wavelength is approximately 1.5). The wavelengths were computed by equation A.7 in Appendix A.1. The phase model and the neuromechanical model agree quantitatively even at high  $\mu_f$ , where the mechanical coupling strength is several orders of magnitude stronger. Figure 3.6(b) shows the stable phase differences between neighboring modules in the six-oscillator phase model (lines, circles) and neuromechanical model (crosses) as a function of external fluid viscosity  $\mu_f$ . Again, the phase model and the neuromechanical model are in quantitative agreement. Furthermore, Figure 3.6(b) shows that increasing fluid viscosity affects the phase-locked states in the six-oscillator case in a similar way as in the two-oscillator case. When neural coupling dominates at low viscosity, the stable phase differences

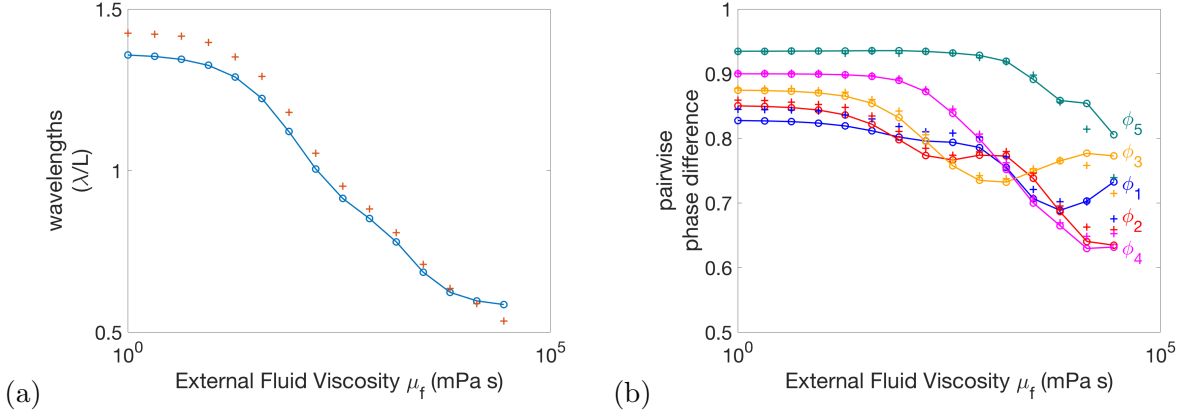


FIGURE 3.6. (a) The wavelengths generated by the six-oscillator phase model (blue line with circles) and neuromechanical model (red crosses) as a function of external fluid viscosity  $\mu_f$  for  $\varepsilon_p = 0.05$  and  $\varepsilon_g = 0.017$ . The wavelength is set by the competition between the mechanical and neural coupling. (b) The phase differences between neighboring oscillator modules in the six-oscillator phase model (lines with circles) and neuromechanical model (crosses) as a function of external fluid viscosity  $\mu_f$  for  $\varepsilon_p = 0.05$  and  $\varepsilon_g = 0.017$ . Similar to the two-oscillator case, the stable phase differences here are set by the competition between mechanical and neural coupling. When neural coupling dominates, the stable phase differences are spread out around 0.9, and when mechanical coupling dominates, the stable phase differences move towards antiphase, i.e., closer to 0.5 phase difference, but with strong boundary effects.

are spread out near 0.9, and as fluid viscosity increases, the mechanical coupling strength increases and the stable phase differences decrease towards antiphase.

The large variation between the phase differences across pairs of modules is due to the non-uniformity of coupling matrices  $D_4^{-1}$ ,  $W_g$ , and  $W_p$ . The modules in the middle receive stronger mechanical coupling than the modules at the boundaries. The boundary modules receive less gap-junctional coupling because they have one fewer neighboring module, and the first module gets zero nonlocal proprioceptive feedback because it has no anterior neighboring module. Figure 3.7 shows the corresponding stable pair-wise phase differences at zero external fluid viscosity as a function of the gap-junctional coupling strength  $\varepsilon_g$ , with proprioceptive coupling strength  $\varepsilon_p$  fit to match wavelength in low-viscosity (1.5 bodylengths) as in Chapter 2.4.3. Even with no mechanical coupling, the phase differences between neighboring modules are still spread out. This indicates that some of the spreading we see in the phase differences in Figure 3.6 is due to the non-uniformity of the neural coupling matrices  $W_g$  and  $W_p$ .

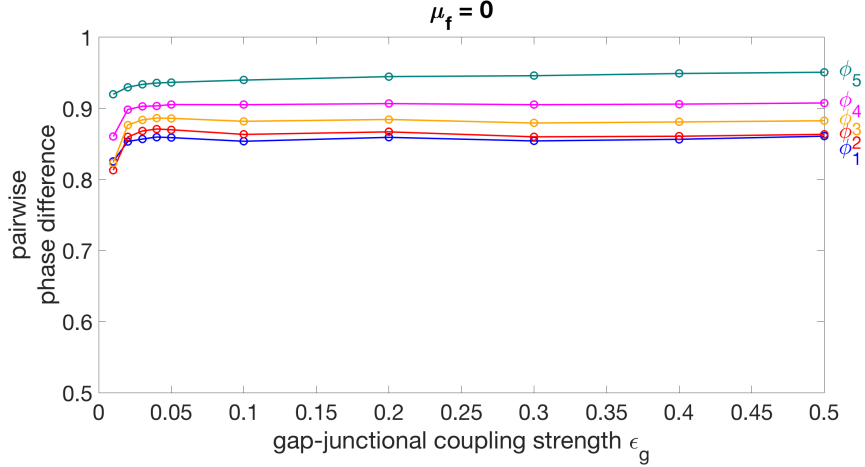


FIGURE 3.7. Stable pair-wise phase differences of the 6-oscillator neuromechanical model at zero external fluid viscosity ( $\mu_f = 0$ ) as a function of gap-junctional coupling strength  $\varepsilon_g$  (proprioceptive coupling strength  $\varepsilon_p$  fit to match wavelength in low-viscosity (1.5 bodylengths) as in Chapter 2.4.3).

The general trend of each phase difference between neighboring modules (decreasing from near-synchrony towards antiphase) underlies the wavelength trend of gait adaptation in Figure 3.6(a) in both the six-oscillator phase model and the neuromechanical model. Thus, the results for the two-oscillator case in Chapter 3.3 extend to the six-oscillator case: the decrease in wavelength in response to increasing fluid viscosity is the result of the corresponding increase in the relative strength of mechanical coupling, which decreases the phase differences between neighboring modules and yields shorter wavelengths.

## CHAPTER 4

### Neuromechanical Oscillator Model

Here, we explore the properties of the neuromechanical oscillator module and provide justification for our choice of neuromuscular parameters in Chapters 2 and 3. We explore the effects of the neuromechanical parameters of the single module, namely the AVB input current  $I$ , the peak muscle force  $c_m$ , the proprioceptive feedback strength  $c_p$ , the body mechanics timescale  $\tau_b$ , and the muscle activity timescale  $\tau_m$ . We show how these parameters affect the period, amplitude, and existence of oscillations in the single module, and we also investigate how they shape the phase response properties.

We perform a bifurcation analysis of the single-oscillator module to find other parameter regimes with oscillations besides the one investigated in Chapters 2 and 3, and investigate the phase response properties of the module in those regimes. We find that there are two major regimes: (I) the “tristable regime” where stable oscillations coexist with two stable states, and (II) the “bistable regime” where stable oscillations coexist with only one stable state. By investigating the phase response properties of the neuromechanical oscillator in these other parameter regimes, we determine that any differences do not significantly alter the coordination or the results of Chapters 2 and 3. However, we show that the ordering of the timescales  $\tau_m$  and  $\tau_b$  can yield changes in the phase response curves that underly the shift in coordination seen in Chapter 3.3.4.

#### 4.1. Bifurcation Analysis of the Neuromechanical Oscillator Model

As in Chapter 3, a single, isolated neuromechanical module is defined as a neural subcircuit, the corresponding muscles and body section, and local proprioceptive feedback (without coupling to the other body regions or neural subcircuits). The dynamics for this isolated module are governed

by

$$(4.1) \quad \dot{\kappa} = -\frac{1}{\tau_b}(\kappa + \sigma(A_V) - \sigma(A_D)),$$

$$(4.2) \quad \dot{A}_V = \frac{1}{\tau_m}(-A_V + V_V - V_D),$$

$$(4.3) \quad \dot{A}_D = \frac{1}{\tau_m}(-A_D + V_D - V_V),$$

$$(4.4) \quad \dot{V}_V = \frac{1}{\tau_n}(F(V_V) + c_p\kappa),$$

$$(4.5) \quad \dot{V}_D = \frac{1}{\tau_n}(F(V_D) - c_p\kappa).$$

The neuromuscular parameters in Chapters 2 and 3 were chosen so that the neuromechanical oscillator units would be in an oscillatory regime and give the approximate frequency (1.76 Hz) observed in a low-viscosity environment. We performed a bifurcation analysis using XPPAUT [13] of the oscillator module (equations 4.1-4.5) to investigate the roles of several unknown parameters in the oscillator, namely the AVB input current  $I$ , the peak muscle force  $c_m$ , the proprioceptive feedback strength  $c_p$ , the muscle activity timescale  $\tau_m$ , and the body mechanics timescale  $\tau_b$ . In particular, we look for different parameter regimes with oscillations, and how the parameters affect the period and amplitude.

**4.1.1. The influence of the AVB input current  $I$ .** In our model,  $I = 0$  is taken to be the default “on” mode. At this value of  $I$ , there are three stable equilibria: a stable “off” rest state, a stable “on” rest state, and a stable limit cycle. In the stable “off” rest state, both  $V_V$  and  $V_D$  are at a low-voltage “off” state, and there is no input from the muscles to the body, so the neuromechanical module is at rest. In the stable “on” rest state, both  $V_V$  and  $V_D$  are at a high-voltage “on” state, and there are equal contractions from the ventral and dorsal muscles to the body, so the neuromechanical module does not bend one way or the other. The stable limit cycle corresponds to the neuromechanical oscillations described in Chapter 3, and the module can reach this state by starting with asymmetric initial conditions (e.g.,  $V_V(0) = 1, V_D(0) = -1, A_V(0) = A_D(0) = \kappa(0) = 0$ ). In other models [5,11], oscillations are induced by including asymmetries in the neural subcircuit, such as an asymmetry in the AVB current to the dorsal and ventral B-neurons and a VD-to-VB inhibitory connection that indirectly allows the DB neuron to inhibit the VB

neuron. This extra connection is not included in the original connectivity diagrams of White et al. [53]; however, it appears in some recent reviews of the motor circuit [10, 19, 25] but not other reviews [58].

The AVB interneuron has been proposed as necessary to forward locomotion [5]. In our model, when the AVB input current  $I$  is “on” and providing steady neural input, the neuromechanical module is capable of oscillations. If  $I$  is larger in magnitude than a critical value, then the system does not oscillate, as shown in the bifurcation diagram in Figure 4.1 for  $c_m = 10, c_p = 1, \tau_n = 0.01s, \tau_m = 0.1s,$  and  $\tau_b = 0.5s$ . For  $I$  sufficiently negative, the only stable state is the “off” rest state, and for  $I$  sufficiently positive, the only stable state is the “on” rest state. For intermediate values of  $I$ , there is bistability between these two states, the boundaries of which are marked by subcritical Hopf bifurcations (HB) in Figure 4.1, which are soon followed by saddle-node bifurcations (SN). Within this region, there are also intermediate values of  $I$  for which there is tristability between the two rest states and neuromechanical oscillations, the boundaries of which are marked by saddle-node of limit-cycles (SNLC) bifurcations in Figure 4.1.

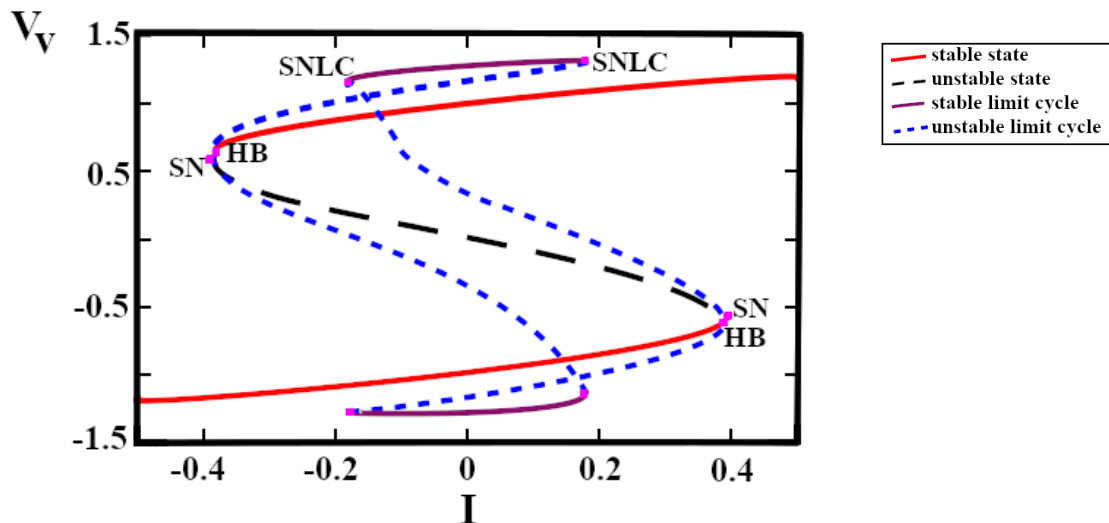


FIGURE 4.1. Bifurcation diagram for  $V_V$  vs.  $I$  for the single oscillator module. Ventral B-class neural activity  $V_V$  is shown on the y-axis. If  $I$  is too large in magnitude, the stable oscillations disappear through saddle-node of limit cycles (SNLC) bifurcations. The stable states lose stability through subcritical Hopf bifurcations (HB), and then disappear soon after in saddle node bifurcations (SN). Other parameters fixed at  $c_m = 10, c_p = 1, \tau_f = 0.5s, \tau_m = 0.1s, \tau_n = 0.01s, a = 1$ .

**4.1.2. The influence of the feedback strengths  $c_m$  and  $c_p$ : increasing robustness of oscillations.** The peak muscle force  $c_m$  and proprioceptive feedback  $c_p$ , both act to increase the range of  $I$ -values for which there are stable oscillations. If their values are too low, oscillations will cease to exist, no matter the value of  $I$ , as shown in the bifurcation diagram in Figure 4.2(a) for  $c_m = 1$ ,  $c_p = 1$ . If  $c_m$ ,  $c_p$  are sufficiently high, oscillations can exist even after one rest state disappears, as shown in the bifurcation diagram in Figure 4.2(b) for  $c_m = 10$ ,  $c_p = 10$ . This case is of particular biological importance because it could give the system a way to start oscillations from rest. If the system is at a rest state,  $I$  can be slowly changed until that rest state becomes unstable in the subcritical Hopf bifurcation, at which point the system will move towards either the stable limit cycle or the other stable state. This cannot happen in the case shown in Figure 4.1, since the subcritical Hopf bifurcations occur when there are no stable limit cycles.

The effects on the robustness of the limit cycles of each of these feedback strengths separately can be seen in the stability diagrams in Figure 4.3. Figure 4.3(a) shows that at a small proprioceptive feedback strength ( $c_p = 1$ ), increasing the peak muscle force  $c_m$  increases the  $I$ -range for which there are stable oscillations with two stable states (the tristable regime), and for sufficiently high  $c_m$  the module is capable of stable oscillations with only one rest state (the bistable regime) as in Figure 4.2(b)). The two white-dotted lines correspond to the bifurcation diagrams in Figures 4.1 and 4.2(a). Figure 4.3(b) shows at a small peak muscle force  $c_m = 1$ , increasing the proprioceptive feedback strength  $c_p$  has a very similar effect. The white-dotted line corresponds to the bifurcation diagram in 4.2(a). Figure 4.3(c) shows that at a higher proprioceptive feedback strength  $c_p = 10$ , increasing the peak muscle force  $c_m$  increases the  $I$ -range for which there are stable oscillations even further, and the module is capable of oscillations that are bistable with only one rest state for an even smaller  $c_m$  threshold than in Figure 4.3(a). The white-dotted line corresponds to the bifurcation diagram in Figure 4.2(b). Similarly, Figure 4.3(d) shows that at a higher peak muscle force  $c_m = 10$ , the effect of increasing the proprioceptive feedback strength  $c_p$  is more dramatic. The two white-dotted lines correspond to the bifurcation diagrams in Figures 4.2(a) and (b). Increasing either feedback  $c_m$  or  $c_p$  increases the  $I$ -range for which there are stable oscillations, and can give the module the potential for bistable oscillations with one stable state.

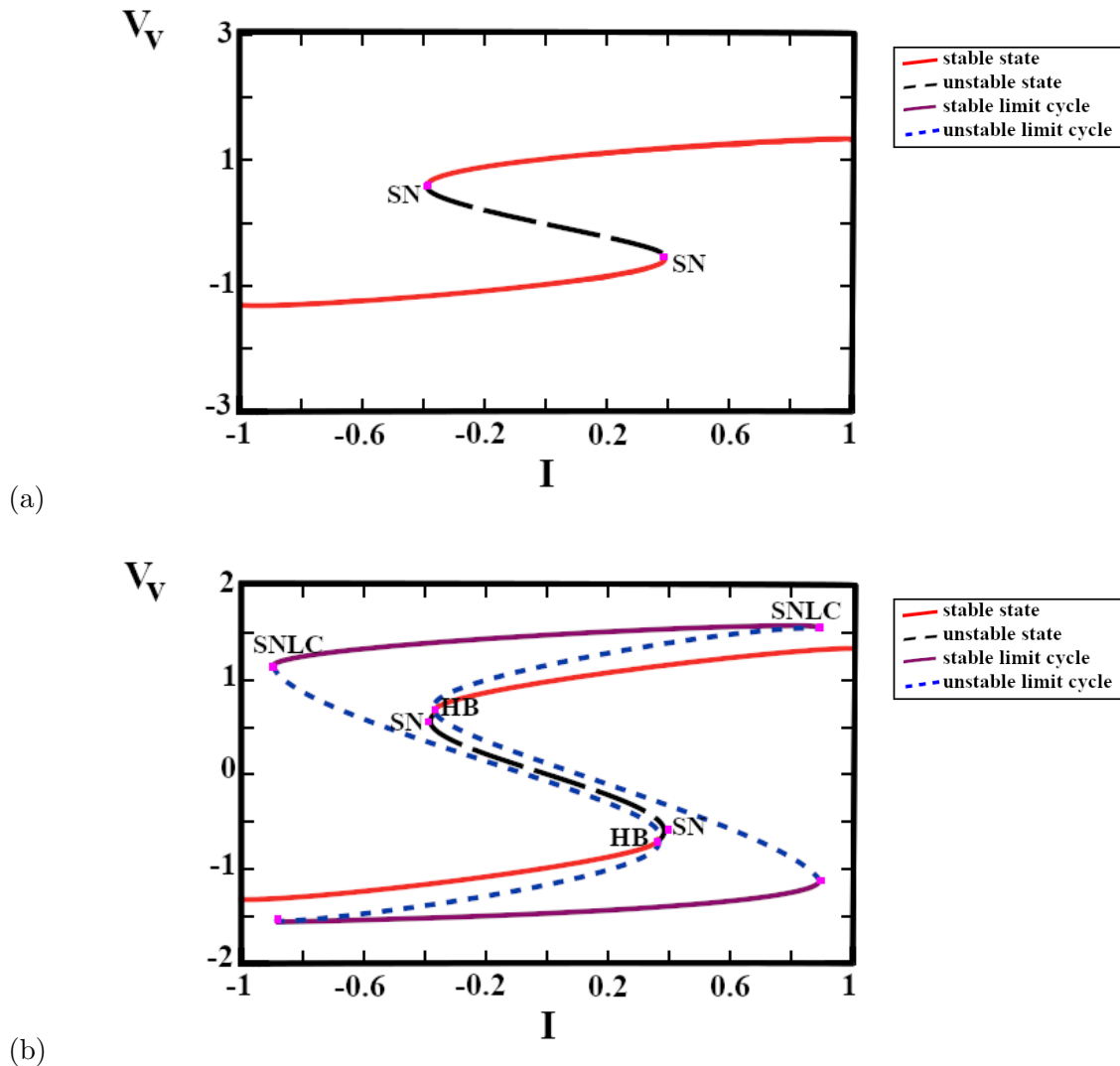


FIGURE 4.2. Bifurcation diagrams for  $V_V$  vs.  $I$  for the single oscillator module in (a) an example non-oscillatory regime, and (b) an example regime with potential for bistable and tristable oscillations. Ventral B-class neural activity  $V_V$  is shown on the y-axis. (a) Feedback strengths too low ( $c_m = 1$ ,  $c_p = 1$ ). Tuning  $I$  cannot lead to stable neuromechanical oscillations. (b) Feedback strengths sufficiently high ( $c_m = 10$ ,  $c_p = 10$ ). There are stable oscillations beyond the bistable stable-state regime, i.e., bistability between a limit cycle and a single stable state.

The effects of  $c_m$  and  $c_p$  can be summarized by Figure 4.4(a), which shows the SNLC and subcritical Hopf bifurcations curves in  $c_m, c_p$ -space. As  $c_m$  and  $c_p$  vary, the system moves through the three parameter regimes corresponding to the bifurcation diagrams in Figures 4.1 and 4.2: no possible oscillations as in Figure 4.2(a); potential for tristable oscillations as in Figure 4.1, i.e., stable

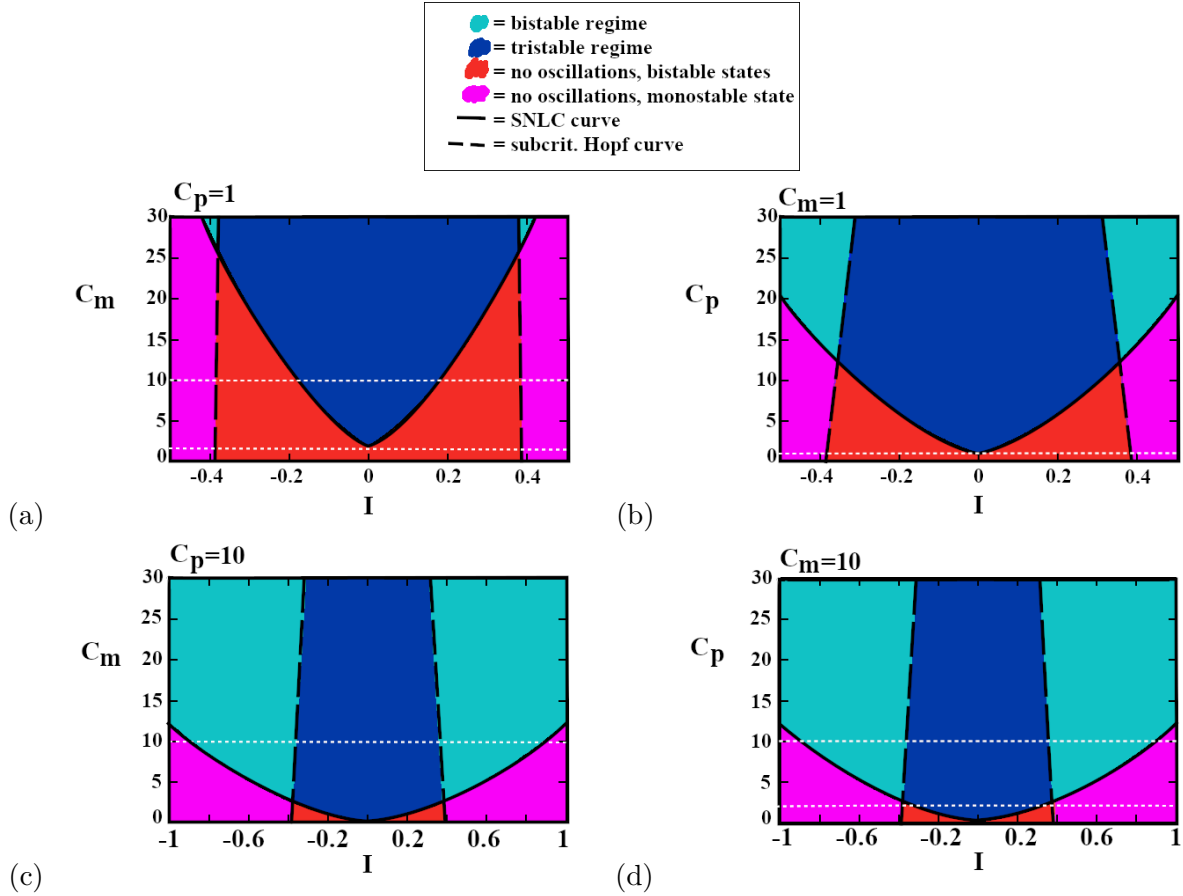


FIGURE 4.3. Stability diagrams for the single oscillator module, tracking the subcritical Hopf and SNLC bifurcations in Figure 4.1 through (a)  $I, c_m$ -space with  $c_p = 1$ , (b)  $I, c_p$ -space with  $c_m = 1$ , (c)  $I, c_m$ -space with  $c_p = 10$ , (d)  $I, c_p$ -space with  $c_m = 10$ . White dotted lines correspond to previous bifurcation diagrams in  $I$ . Increasing either feedback  $c_m$  or  $c_p$  increases the  $I$ -range for which there are stable oscillations, and can give the module the potential for bistable oscillations with one stable state.

oscillations and two stable states; and potential for either tristable or bistable oscillations (with only one stable state) as in Figure 4.2(b). Interestingly enough, these bifurcation curves are given by  $c_m \cdot c_p = \text{constant}$ . Figure 4.4(b) shows that the SNLC and subcritical Hopf bifurcations curves are linear in  $c_m, 1/c_p$ -space. In Chapter 5, we explore an idealized version of the neuromechanical oscillator, which has  $c_m \cdot c_p = c$  as a nondimensional feedback strength. In this model,  $c_m$  and  $c_p$  act together through their combined effects on the robustness of oscillations.

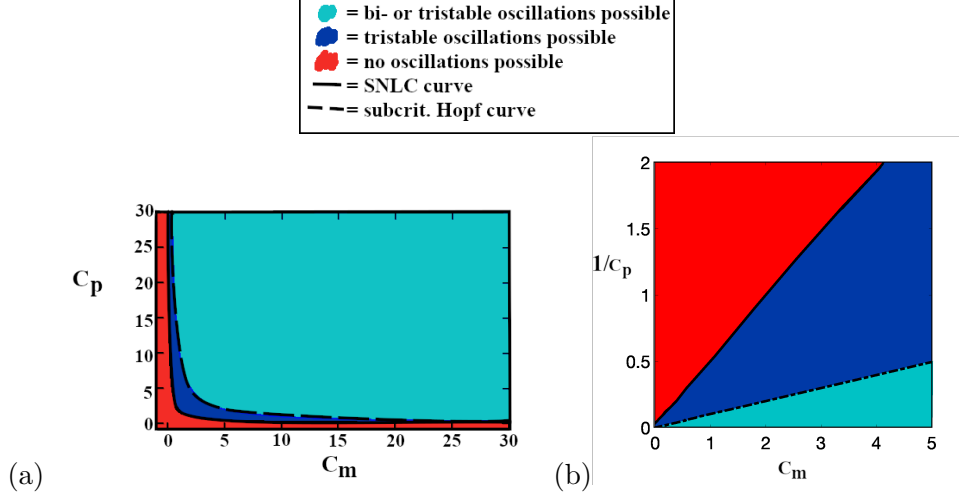
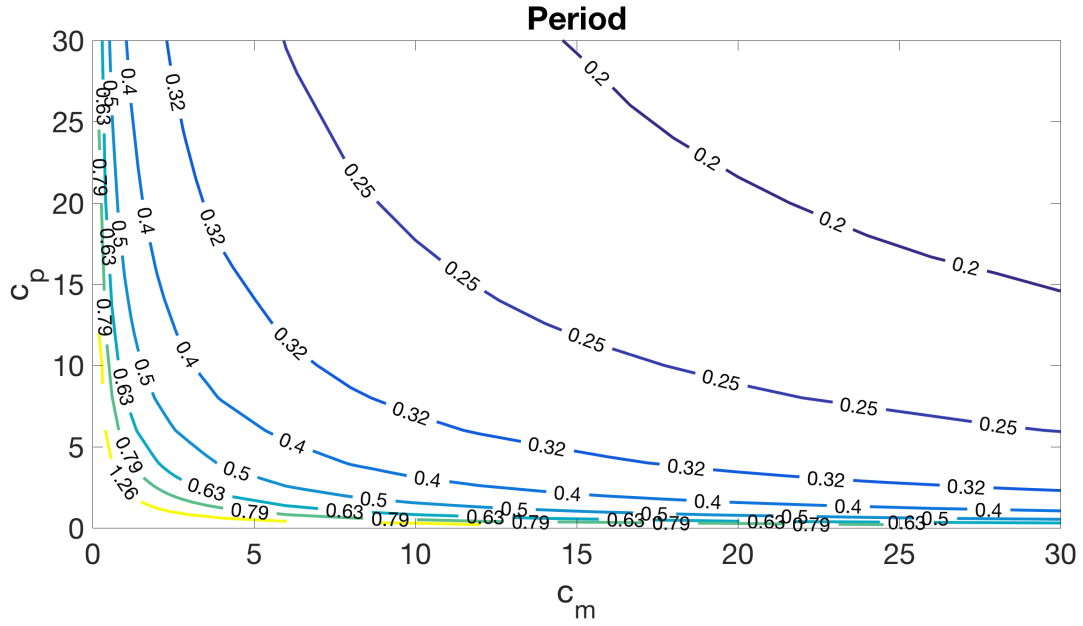


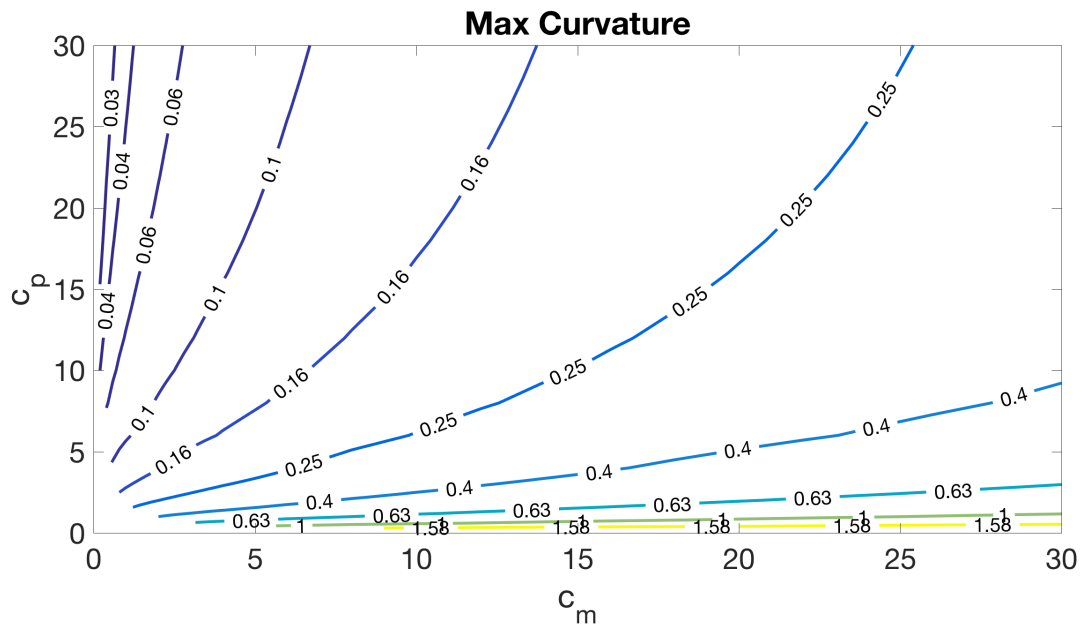
FIGURE 4.4. Stability diagrams for (a)  $c_m$  and  $c_p$ , and (b)  $c_m$  and  $1/c_p$ , both with  $I = 0, \tau_f = 0.5s, \tau_m = 0.1s, \tau_n = 0.01s, a = 1$ . The black line marks the curve of SNLC bifurcations and the black dashed line marks the curve of subcritical Hopf bifurcations. The red region at low  $c_m, c_p$  values corresponds to the parameter regime with no potential for stable neuromechanical oscillations (as in Figure 4.2(a)). The blue region at intermediate  $c_m, c_p$  values corresponds to the parameter regime with the potential for tristable oscillations (as in Figure 4.1). The cyan region at high  $c_m, c_p$  values corresponds to the parameter regime with the potential for either tristable or bistable oscillations (as in Figure 4.2(b)).

**4.1.3. The influence of the feedback strengths  $c_m$  and  $c_p$ : effects on oscillation period and amplitude.** While the two feedback strengths have similar effects on the robustness of oscillations, they differ in their effects on the period and (max curvature) amplitudes of the oscillator. Figure 4.5(a) shows that increasing either the peak muscle force  $c_m$  or the proprioceptive feedback strength  $c_p$  will decrease the oscillator period. That is, smaller muscle activities will result in larger muscle forces, and smaller body bends will result in larger feedback to the neural circuit, so the neuromechanical oscillations will progress faster. Figure 4.5(b) shows that increasing the peak muscle force  $c_m$  increases the max curvature amplitudes by effectively imposing larger body bends, but increasing the proprioceptive feedback strength  $c_p$  decreases the max curvature amplitudes by effectively lowering the proprioceptive feedback threshold.

Therefore, by changing these two feedback strengths separately, the period and amplitude of the neuromechanical oscillator module can be changed independently of one another while still maintaining robust oscillations. This property of the model will be useful for modeling the body as



(a)



(b)

FIGURE 4.5. (a) Increasing either the peak muscle force  $c_m$  and proprioceptive feedback strength  $c_p$  decreases the period (in seconds) of the oscillator module. (b) Increasing the peak muscle force  $c_m$  increases the max curvature amplitude of the oscillator module, but increasing the proprioceptive feedback strength  $c_p$  decreases the max curvature amplitude. In both contour plots, the other parameters are fixed at  $\tau_f = 0.5s$ ,  $\tau_m = 0.1s$ ,  $\tau_n = 0.01s$ , and  $I = 0$ .

a chain of heterogeneous oscillators. For instance, we could model the body as a chain of oscillators with increasing  $c_p$  posteriorly to account for the decreasing undulation amplitude along the body towards the tail.

**4.1.4. The influence of the timescales  $\tau_b$  and  $\tau_m$ .** We also investigate how the mechanical timescale  $\tau_b$  and muscle activity timescale  $\tau_m$  affect the oscillatory properties of the neuromechanical model.  $\tau_m$  is constrained by biophysical estimates to be within 50-250 ms [35], but  $\tau_b = \mu_b/k_b$  has been estimated across several orders of magnitude, as explained in Chapter 2.3.

We explore how the two timescales affect the period and amplitude of the oscillations. Increasing either the body mechanics timescale  $\tau_b$  or the muscle activity timescale  $\tau_m$  increases the oscillator period, as shown in the contour plot in Figure 4.6(a). In Chapter 2.4.2, we use a parameter search algorithm to choose a muscle activity timescale  $\tau_m$  for every body mechanical timescale  $\tau_b$  in order to obtain approximately the correct period ( $\approx 0.5s$ ) in water. This algorithm is equivalent to selecting a point  $(\tau_m, \tau_b)$  on the 0.5 contour in Figure 4.6(a).

Figure 4.6(b) shows that increasing the body mechanics timescale  $\tau_b$  decreases the max curvature amplitude of the oscillator, however the relationship between the muscle activity timescale  $\tau_m$  and the max amplitude is more complex. Increasing  $\tau_m$  in some ranges of  $\tau_b$  will increase the max curvature amplitude, while for other ranges of  $\tau_b$  it will decrease the max curvature amplitude. These ranges of increasing and decreasing effects are not consistent across values of  $\tau_b$ , as illustrated by the structure of the contours in Figure 4.6(b). While we do not look at the curvature amplitudes of the neuromechanical model in Chapters 2 and 3, the complicated relationship between the timescales and the max curvature amplitude shown here suggests another way to compare the model with experimental data to narrow down the range of the unknown timescales.

We also explore how  $\tau_b$  and  $\tau_m$  affect the robustness of oscillations in the neuromechanical module. Figure 4.7(a) shows the stability diagram created by following the SNLC bifurcations in Figure 4.1 through  $I, \tau_b$ -parameter space, for  $\tau_m = 0.1$  s and  $\tau_n = 0.01$  s. The neuromechanical module has oscillations for a wide range of  $I$ -values when the mechanical timescale  $\tau_b \in [0.01s, 1s]$  ( $\log_{10} \tau_b \in [-2, 0]$  in Figure 4.7(a)), suggesting that it oscillates robustly regardless of our choice of mechanical timescale. The module doesn't cease to oscillate for large or small  $\tau_b$ , but the oscillations

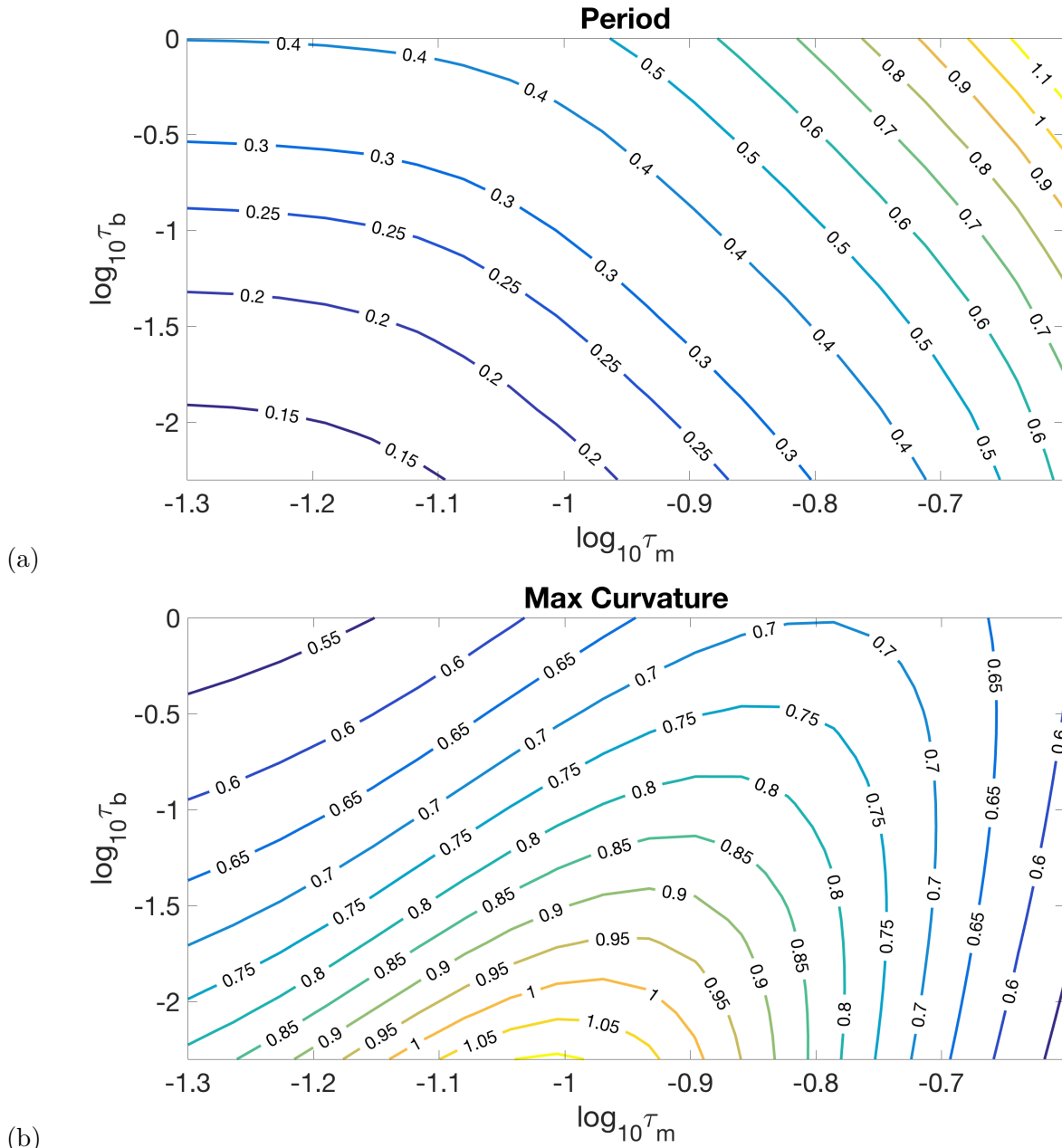


FIGURE 4.6. (a) Increasing either the body mechanics timescale  $\tau_b$  or the muscle activity timescale  $\tau_m$  are increases the oscillator period (timescales and period in seconds). (b) Increasing the body mechanics timescale  $\tau_b$  decreases the max curvature amplitude of the oscillator, however the relationship between the muscle activity timescale  $\tau_m$  and the max amplitude is more complex. In both contour plots, the other parameters are fixed at  $c_m = 10$ ,  $c_p = 1$ ,  $\tau_n = 0.01s$ , and  $I = 0$ .

occur over a narrower  $I$  range as  $\tau_b$  increases above 1 s or decreases below 0.01 s. This lower value (0.01 s) coincides with the value of the neural timescale  $\tau_n$ .

Figure 4.7(b) shows a similar stability diagram created by following the SNLC bifurcations in Figure 4.1 through  $I, \tau_m$ -parameter space, for  $\tau_b = 0.5$  s and  $\tau_n = 0.01$  s. The module has oscillations for a wide range of  $I$ -values when the muscle activity timescale  $\tau_m \in [0.01\text{s}, 1\text{s}]$  ( $\log_{10} \tau_m \in [-2, 0]$  in Figure 4.7(b)), suggesting that it oscillates robustly regardless of our choice of muscle activity timescale. Again, the module doesn't cease to oscillate for large or small  $\tau_m$ , but the oscillations occur over a narrower  $I$  range as  $\tau_m$  increases above 1 s or decreases below 0.01 s.

Figure 4.7(c) shows the stability diagram created by following the SNLC bifurcations in Figure 4.1 through  $c_m, \tau_b$ -parameter space, with  $I \approx 0.19$ . As we show in the previous subsections, increasing  $c_m$  increases the robustness of oscillations in the module, and here it also increases the range of  $\tau_b$  for which there are oscillations. The stability diagram for  $c_p, \tau_b$  is almost identical, so it is omitted here. Figure 4.7(d) shows a similar stability diagram created by following the SNLC bifurcations in Figure 4.1 through  $c_m, \tau_m$ -parameter space, with  $I$  fixed. As we show in the previous subsections, increasing  $c_m$  increases the robustness of oscillations in the module, and here it also increases the range of  $\tau_m$  for which there are oscillations. The stability diagram for  $c_p, \tau_m$  is almost identical, so it is omitted here.

## 4.2. Phase Response Properties of the Neuromechanical Oscillator Model

Here, we will explore how neuromechanical module parameters affect the phase response properties of the neuromechanical oscillator model by looking at the phase response curves (PRCs). In order to determine whether the results of Chapters 2 and 3 were reliant on our choice of neuromechanical module parameters, we first compare the PRCs and G-functions in the two major regimes from the previous section: (I) the tristable regime where stable oscillations coexist with two stable states, (II) the bistable regime where stable oscillations coexist with only one stable state. The tristable regime (I) uses the neuromechanical parameters in Chapters 2 and 3. We conclude that despite slight differences in the PRCs, the similarities between the G-functions implies similar coordination, and thus the results of Chapters 2 and 3 would be similar in the bistable regime (II). We also look at how the neuromechanical oscillator parameters  $c_m, c_p, \tau_b$ , and  $\tau_m$  affect the phase

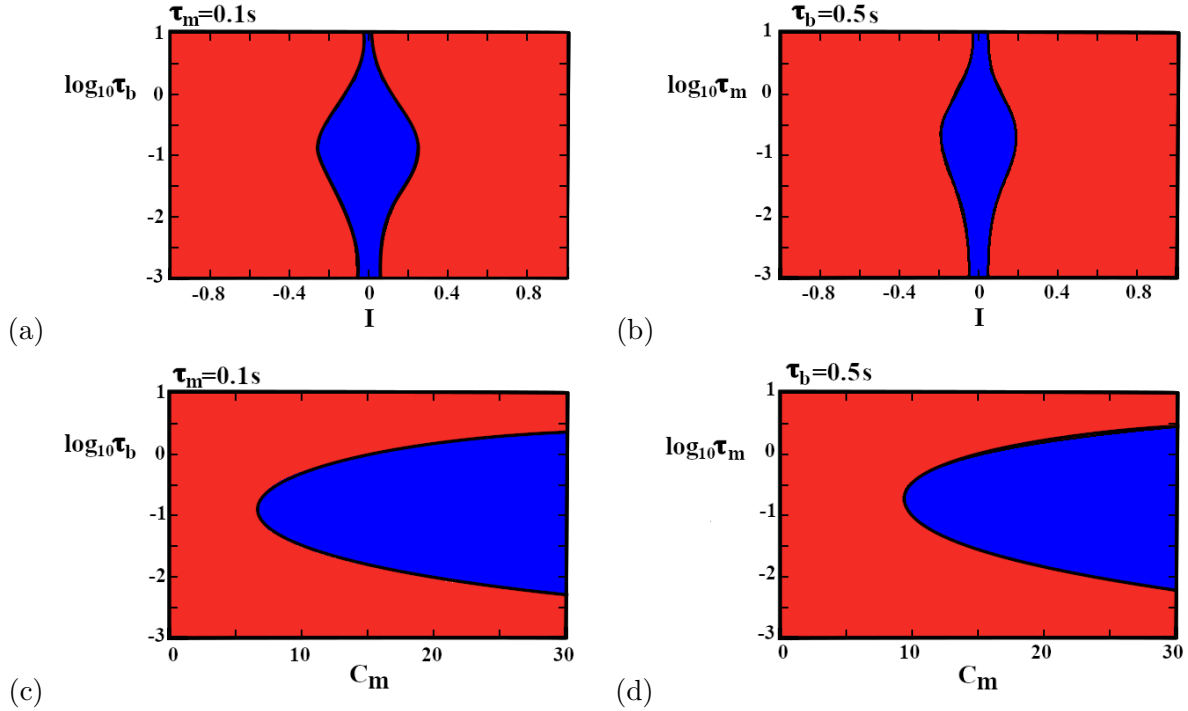


FIGURE 4.7. Stability diagrams for the neuromechanical module, tracking the SNLC bifurcations in Figure 4.1 through (a)  $I, \tau_b$ -space, (b)  $I, \tau_m$ -space, (c)  $c_m, \tau_b$ -space, and (d)  $c_m, \tau_m$ -space. Black lines mark the curves of SNLC bifurcations. Blue regions correspond to parameter regimes with the possibility of oscillations, and red regions correspond to parameter regimes with no possibility of oscillations.

response properties of the neuromechanical oscillators and thus the coordination of the model. In particular, we look at how the phase response properties explain the shift in coordination due to the ordering of the timescales  $\tau_m, \tau_b$  seen in Chapter 3.3.4.

**4.2.1. Comparing the tristable and bistable regimes: PRCs and G-functions.** The phase response curves for both the tristable regime (I) and the bistable regime (II) are shown in Figure 4.8. In the tristable regime, we consider  $\tau_b = 0.5s$ ,  $\tau_m = 0.1s$ ,  $\tau_n = 0.01s$ ,  $c_m = 10$ ,  $c_p = 1$ , and  $I = 0$ ; these are the same parameters used in Chapters 2 and 3 and corresponds to a vertical slice at  $I = 0$  in the bifurcation diagram in Figure 4.1. In the bistable regime, we consider  $\tau_b = 0.5s$ ,  $\tau_m = 0.1s$ ,  $\tau_n = 0.01s$ ,  $c_m = 10$ ,  $c_p = 10$ , and  $I = 0.5$  (i.e.,  $c_p$  and  $I$  are both increased); these parameters correspond to a vertical slice at  $I = 0.5$  in the bifurcation diagram in Figure 4.2(b).

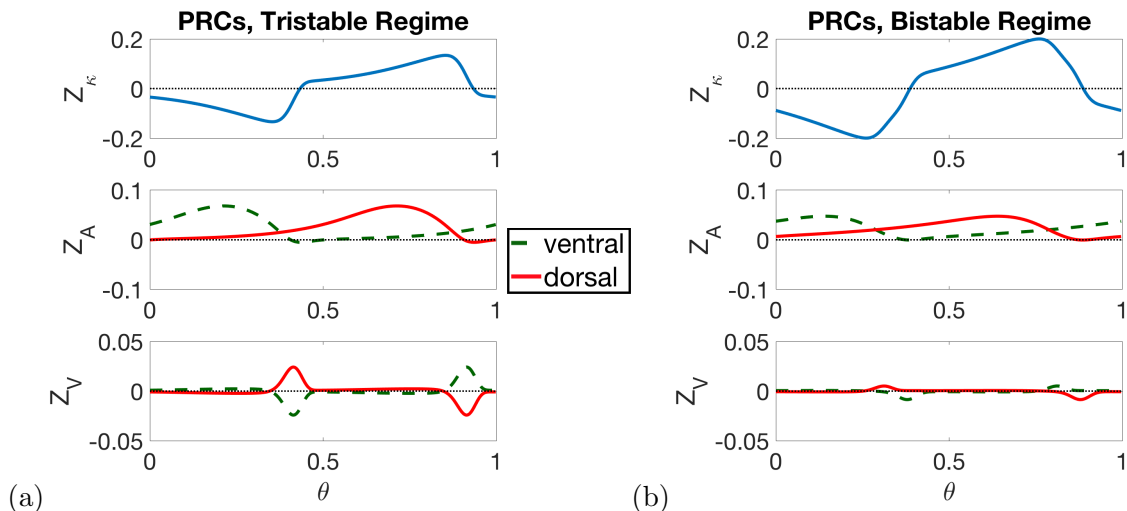


FIGURE 4.8. PRCs for the neuromechanical oscillator module for parameter regimes with (a) tristability between stable oscillations and two stable rest states, and (b) bistability between stable oscillations and one rest state. The PRCs for the muscle and neural activities are given in dashed green lines for the ventral and solid red lines for the dorsal.

The two sets of PRCs have slight amplitude differences and a major timing difference in the neural PRCs. The curvature PRC has a larger amplitude in the bistable regime, which indicates that the bistable regime is more sensitive to mechanical perturbations. The muscle activity PRCs have slightly lower amplitudes in the bistable regime. The neural activity PRCs have much lower amplitudes in the bistable regime. The timing of the neural PRCs is also very different between the two regimes: in the tristable regime, the ventral and dorsal PRCs are always equal and opposite and perfectly synchronized; in the bistable regime, the ventral and dorsal PRCs are more sensitive to perturbation timings that yield negative phase responses than those timings that yield positive phase responses. Moreover, the ventral and dorsal neurons are not symmetric in their phase responses—the first peak of the dorsal PRC is timed before the first peak of the ventral PRC, and the second peak of the dorsal PRC is timed after the second peak of the ventral PRC.

These differences in the phase response curves translate to only minor differences of the G-functions in the pair of neuromechanical oscillators. Figure 4.9 shows the G-functions for the pair of neuromechanical oscillators in both the tristable and bistable regimes. The promoted phase-locked states of the mechanical and gap-junctional coupling modalities are unchanged between regimes, however, so the coordination is relatively similar. Only the proprioceptive G-functions promote

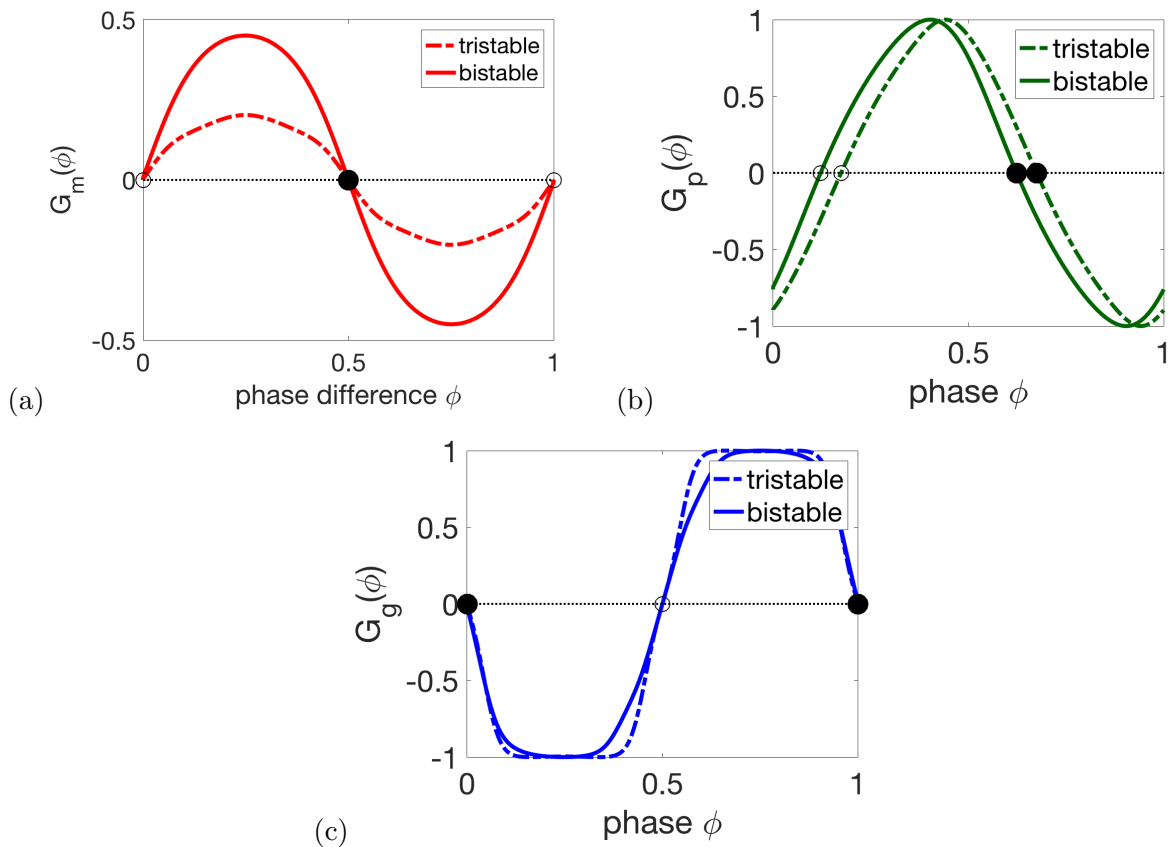


FIGURE 4.9. G-functions for the neuromechanical oscillator module for tristable and bistable parameter regimes: (a) mechanical, (b) proprioceptive, (c) gap-junctional. Stable phase-locked states are given by filled black circles.

different phase-locked states, as shown in Figure 4.9(b), but the promoted phase-locked state is still intermediate between synchrony and antiphase. This difference would likely only change the coupling parameters  $\varepsilon_p$  and  $\varepsilon_g$  needed to obtain the approximate wavelength in water in the model as in Chapter 3.

We also examined how the sign of the AVB input  $I$  in the bistable parameter regime effects the phase response properties of the module. Figure 4.10 shows that for two different modules, each in the bistable parameter regime (with  $c_m = 10$  and  $c_p = 10$ ) but with equal but opposite-signed AVB input current, the PRCs are the same except for the timing and sensitivities of the neural PRCs. Figure 4.10(a) shows that when the AVB input is negative ( $I = -0.5$ ), the ventral and dorsal PRCs are more sensitive to perturbation timings that yield positive phase responses than those timings that yield negative phase responses. Also, the timing of the first peak of the ventral

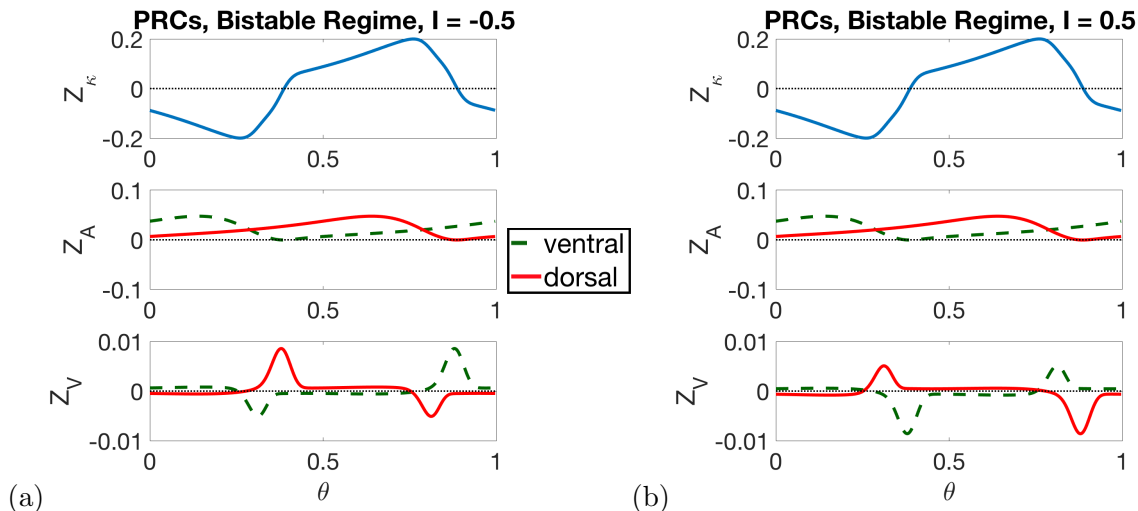


FIGURE 4.10. PRCs for the neuromechanical oscillator module for bistable parameter regimes with  $c_m = 10$ ,  $c_p = 10$ , and (a) negative AVB input  $I = -0.5$ , or (b) positive AVB input  $I = 0.5$ . The PRCs for the muscle and neural activities are given in dashed green lines for the ventral and solid red lines for the dorsal.

PRC is before the first peak of the dorsal PRC, and the second peak of the ventral PRC is timed after the second peak of the dorsal PRC. On the other hand, Figure 4.10(b) shows that when the AVB input is positive ( $I = 0.5$ ), the timings and sensitivities flip. The ventral and dorsal PRCs are more sensitive to perturbation timings that yield negative phase responses than those timings that yield positive phase responses. The first peak of the dorsal PRC is timed before the first peak of the ventral PRC, and the second peak of the dorsal PRC is timed after the second peak of the ventral PRC. These differences indicate that the AVB input  $I$ , which biases the neurons towards one state or the other (active or inactive), has a large effect on both the timing and sensitivity of the neural PRCs. However, as shown in the G-functions in Figure 4.9, these differences are not likely to yield any major coordination changes in the full model.

#### 4.2.2. The influence of feedback strengths $c_m$ and $c_p$ on phase response properties.

We also investigated how the peak muscle force  $c_m$  and proprioceptive feedback strength  $c_p$  affect the phase response properties of the neuromechanical oscillator. Starting with parameters in the tristable regime ( $c_m = 10$ ,  $c_p = 1$ ,  $I = 0$ ), we increased either the peak muscle force  $c_m$  (up to  $c_m = 20$ ) or the proprioceptive feedback strength  $c_p$  (up to  $c_p = 10$ ).

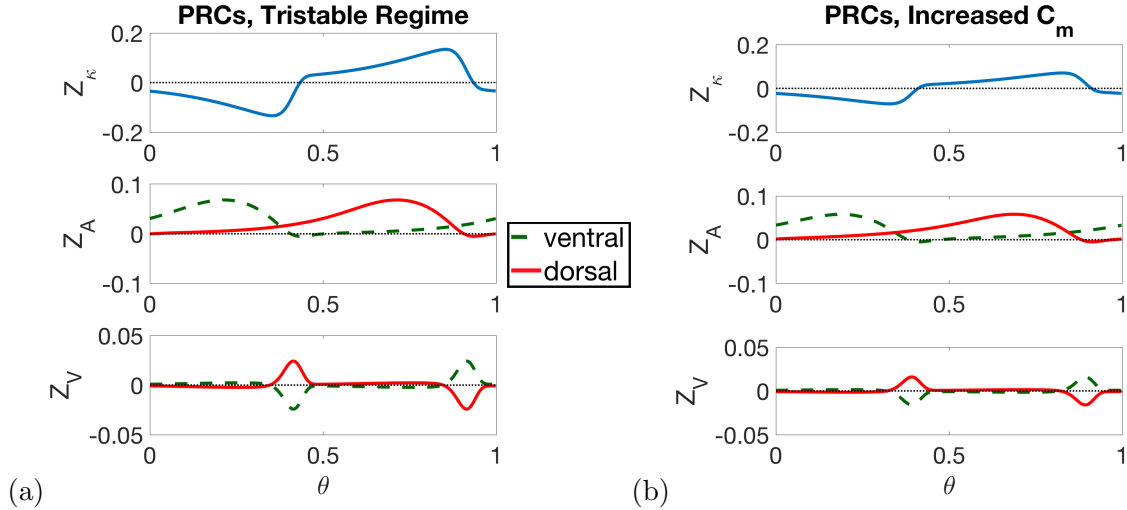


FIGURE 4.11. PRCs for the neuromechanical oscillator module for (a) the tristable regimes (with  $c_m = 10$ ) and (b) increased peak muscle force  $c_m = 20$ . The PRCs for the muscle and neural activities are given in dashed green lines for the ventral and solid red lines for the dorsal.

Figure 4.11 shows that increasing  $c_m$  by a factor of 2 lowers the amplitude of both the curvature PRC and the neural PRCs by a factor of about 2, while the muscle activity PRCs are relatively unchanged. Thus increasing  $c_m$  makes the neuromechanical module less sensitive to perturbations overall. Increasing the peak muscle force  $c_m$  yields a larger bending moment and thus the module reaches its threshold curvature faster, so perturbations have less of an effect.

Figure 4.12 shows that increasing  $c_p$  by a factor of 10 slightly increases the amplitude of the curvature PRC and slightly lowers the amplitude of the neural PRCs and muscle activity PRCs. Thus increasing  $c_p$  makes the neuromechanical module less sensitive to neural perturbations but more sensitive to mechanical perturbations. Increasing the proprioceptive feedback strength  $c_p$  results in a lowering of the effective threshold curvature, i.e., the neurons switch on/off at smaller curvatures, and thus perturbations to the module's curvature can significantly speed up or delay the oscillator. However, because the neurons and muscles are more tightly coupled to the curvature through the stronger proprioceptive feedback, neural and muscle activity perturbations have less of an effect on the oscillator's phase.

These differences in phase response do not significantly alter the coordination in the pair of oscillators. Figure 4.13 shows the G-functions for the pair of neuromechanical oscillators in the

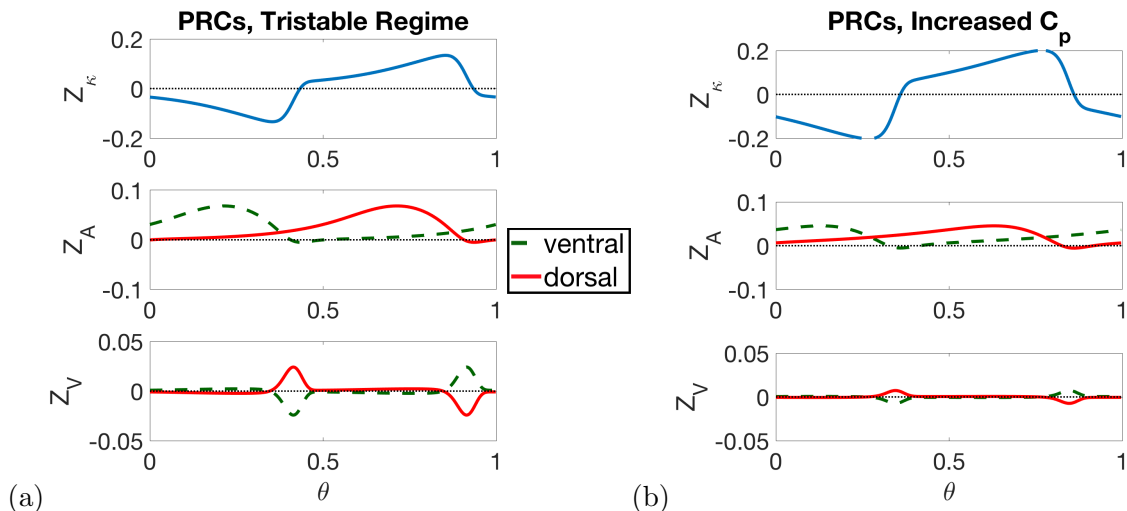


FIGURE 4.12. PRCs for the neuromechanical oscillator module for (a) the tristable regimes (with  $c_p = 1$ ) and (b) increased proprioceptive feedback strength  $c_p = 10$ . The PRCs for the muscle and neural activities are given in dashed green lines for the ventral and solid red lines for the dorsal.

tristable regime, with increased  $c_m$ , and with increased  $c_p$ . The promoted phase-locked states of the mechanical and gap-junctional coupling modalities are unchanged between regimes, however, so the coordination is relatively similar. Only the proprioceptive G-functions promote different phase-locked states, as shown in Figure 4.13(b), but the promoted phase-locked state is still intermediate between synchrony and antiphase. This difference would likely only change the coupling parameters  $\varepsilon_p$  and  $\varepsilon_g$  needed to obtain the approximate wavelength in water in the model as in Chapter 3.

**4.2.3. Phase response properties underlying timescale ordering.** In Chapter 3.3.4, we showed that changing the order of the timescales  $\tau_b$  and  $\tau_m$  changes the coordination by altering the stability of the phase-locked states in the pair of neuromechanical modules. Here, we show that the shape of the phase response curves, which plays a key role in setting the zeros of the G-functions in Figure 3.5(a-c), have only slight changes between the two main cases  $\tau_b$  less than and greater than  $\tau_m$ .

Figure 4.14 shows the PRCs for (a)  $\tau_b = 0.5s > \tau_m = 0.15s$ , and (b)  $\tau_b = 0.05s < \tau_m = 0.15s$ . The curvature PRCs  $Z_\kappa$  are different in timing, with the zero crossings slightly before phase 0.5 and 0 in the  $\tau_b > \tau_m$  case, but slightly after phase 0 and 0.5 in the  $\tau_b < \tau_m$  case. The curvature PRCs are also lower in amplitude by a factor of 2 in the  $\tau_b < \tau_m$  case. The muscle activity PRCs

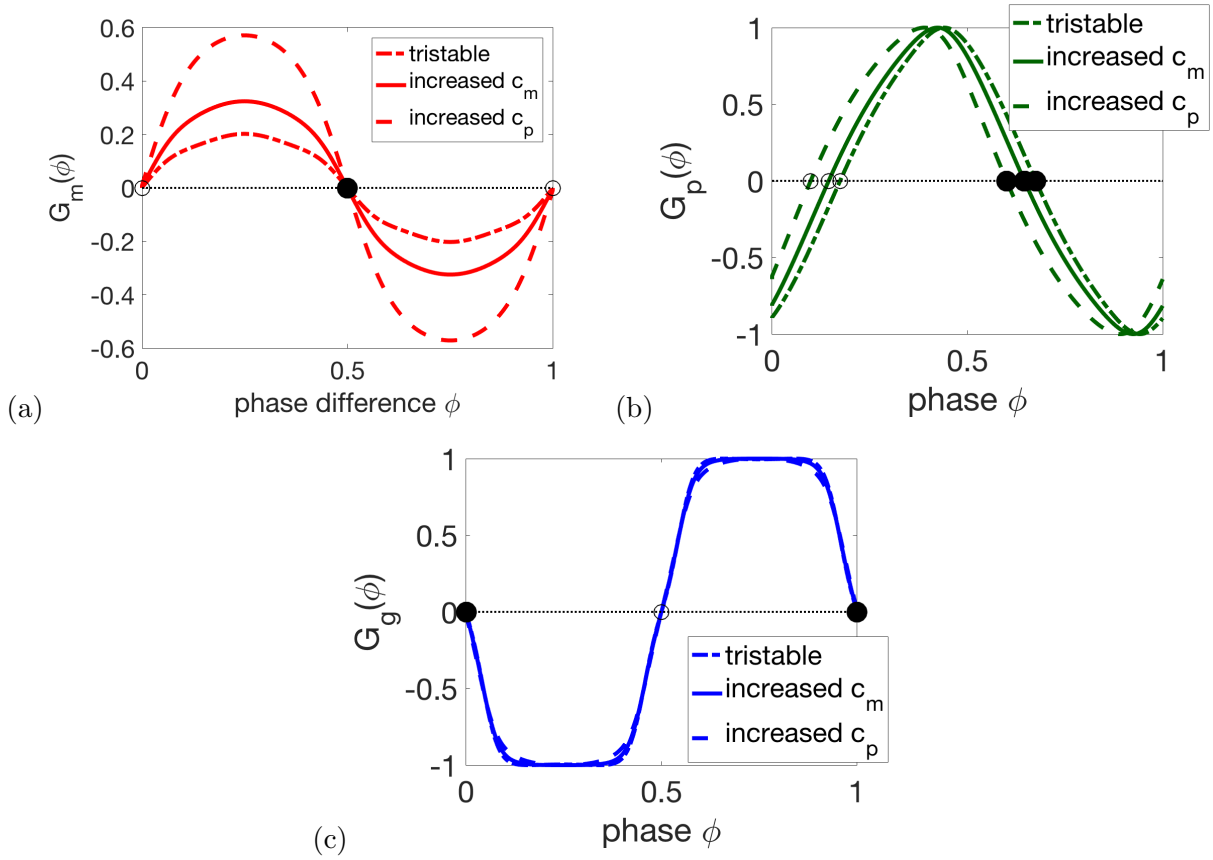


FIGURE 4.13. G-functions for the neuromechanical oscillator module for the tristable parameter regime, with increased  $c_m$ , and with increased  $c_p$ : (a) mechanical, (b) proprioceptive, (c) gap-junctional. Stable phase-locked states are given by filled black circles.

are relatively similar in amplitude between the two cases, but in the  $\tau_b > \tau_m$  case they have slight negative responses to certain timings, while in the  $\tau_b < \tau_m$  case they only ever have positive phase responses. The neural activity PRCs are also relatively similar in amplitude between the two cases, but in the  $\tau_b > \tau_m$  case they are flatter away from the peaks, i.e. they are less sensitive to perturbations outside of the peak-timing windows.

To see how the two cases differ in coordination, Figure 4.15 shows the curvature PRC  $Z_\kappa$ , the coupling current  $d\kappa/dt$ , and the mechanical G-function  $G_m$  for the two cases: (a)  $\tau_b = 0.5s > \tau_m = 0.15s$ , (c)  $\tau_b = 0.05s < \tau_m = 0.15s$ . The mechanical G-function, which is the odd-part of the convolution of the curvature PRC  $Z_\kappa$  and the mechanical coupling current  $d\kappa/dt$ , has flipped stabilities of the synchronous and antiphase-locked states when  $\tau_b > \tau_m$  compared to when  $\tau_b < \tau_m$ .

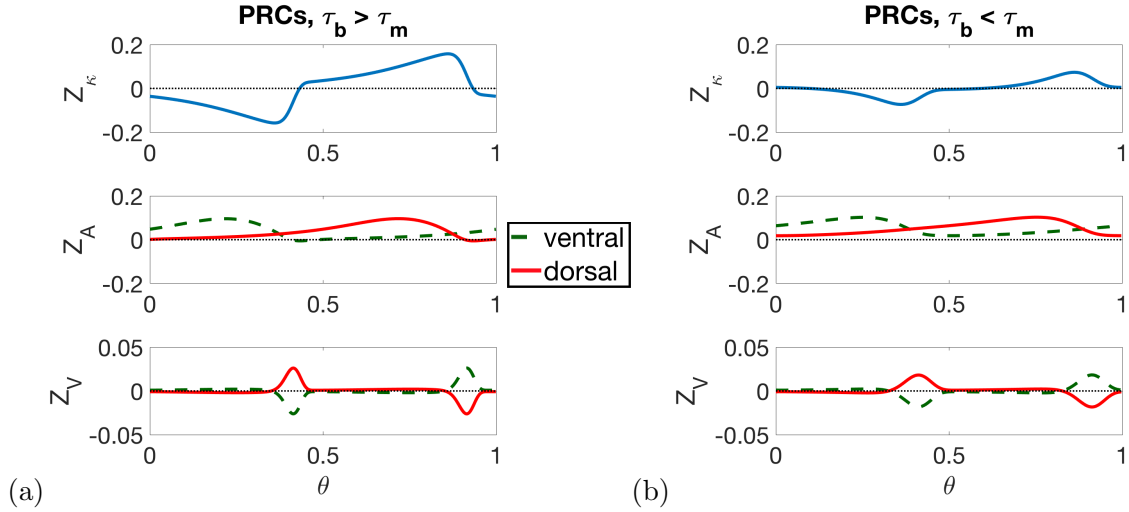


FIGURE 4.14. PRCs for the neuromechanical oscillator module for parameter regimes with (a)  $\tau_b > \tau_m$ , and (b)  $\tau_b < \tau_m$ . The PRCs for the muscle and neural activities are given in dashed green lines for the ventral and solid red lines for the dorsal.

The coupling current  $d\kappa/dt$  is relatively similar between these two cases, though maybe more sinusoidal in the  $\tau_b < \tau_m$  case, but with similar timing. The curvature PRC  $Z_\kappa$  are different in timing, with the zero crossings slightly before phase 0.5 and 0 in the  $\tau_b > \tau_m$  case, but slightly after phase 0 and 0.5 in the  $\tau_b < \tau_m$  case. However, how these slight differences cause the shift in stability of the phase-locked states in the mechanical G-function remains unclear.

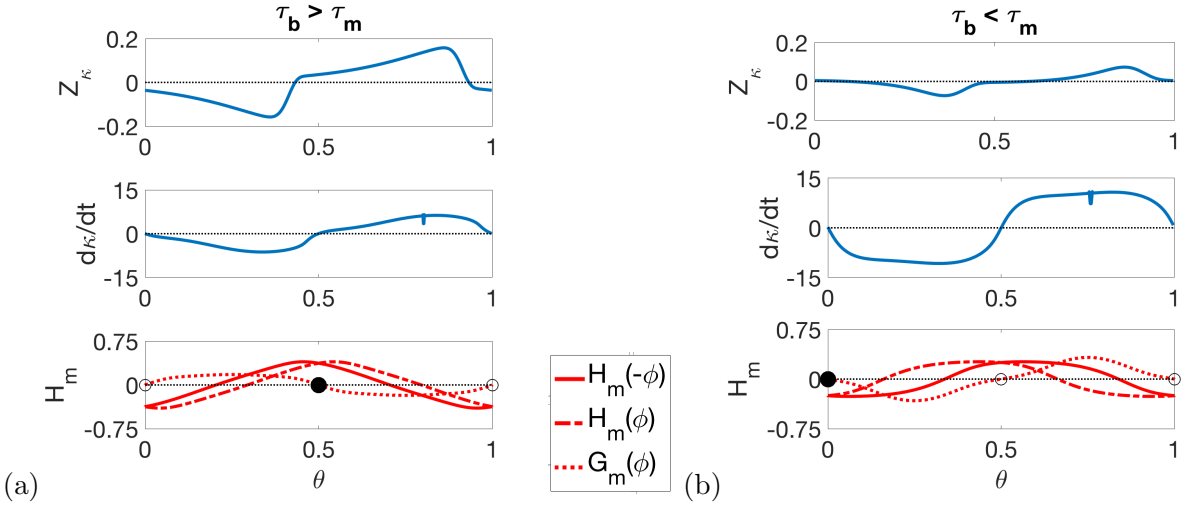


FIGURE 4.15. Curvature PRC  $Z_\kappa$ , coupling current  $d\kappa/dt$ , and the mechanical H and G functions ( $H_m(\phi)$ ,  $H_m(-\phi)$ , and  $G_m(\phi)$ ) for the neuromechanical oscillator module for parameter regimes with (a)  $\tau_b > \tau_m$  and (b)  $\tau_b < \tau_m$ .

## Reduction of the Neuromechanical Oscillator to a 1-D Map Captures Limit Cycle Dynamics

Here, we reduce our neuromechanical oscillator model to a 2-dimensional hybrid system, and then reduce it further to a 1-D Poincaré map that captures the limit cycle dynamics. This map makes it easier to assess when limit cycles exist and what sets the period and amplitude of the neuromechanical oscillations. The 1-D map also provides a framework for future work: analysis of the mechanisms underlying the neuromechanical oscillator, its phase response properties, and the coordination of the full neuromechanical model.

### 5.1. Reduction of the Neuromechanical Oscillator

To reduce the neuromechanical oscillator module (equations 4.1-4.5) down to a 2-dimensional hybrid system with instantaneous switching input, we first linearize the muscle force, then nondimensionalize the system, and finally use a singular limit to reduce the neural activity to discrete states. The reduced model can be solved piecewise and used to understand the neuromechanical oscillation mechanism.

**5.1.1. Analogous Linear Model for Muscle Force.** We use the same dynamics for the muscle activity as in the neuromechanical oscillator model (equations 4.1-4.3). The ventral (dorsal) muscle activity  $A_V$  ( $A_D$ ) induces a contractile force  $\sigma(A)$  (equation 2.7) in the ventral (dorsal) body wall of the neuromechanical module, which changes the body curvature. During oscillations in the neuromechanical oscillator model, the sigmoid-like function  $\sigma(A)$  is usually not saturated at the peak muscle force, so here we assume that  $\sigma(A)$  is linear, i.e.,  $\sigma(A) = A$ . (Note that this means that in this reduced model, negative muscle activity can effectively produce expansive forces rather than contractile forces). The linear contractile forces applied by the muscles induce a bending moment

in the neuromechanical module, changing its body curvature  $\kappa$  according to

$$(5.1) \quad \frac{d\kappa}{dt} = -\frac{1}{\tau_b} \left( \kappa + \frac{c_m}{2} (A_V - A_D) \right).$$

Since the rate of change of curvature depends only on the difference between the muscle activities  $M = A_D - A_V$ , this allows us to reduce the neuromechanical module to

$$(5.2) \quad \frac{d\kappa}{dt} = -\frac{1}{\tau_b} \left( \kappa - \frac{c_m}{2} M \right),$$

$$(5.3) \quad \frac{dM}{dt} = \frac{1}{\tau_m} (2(V_D - V_V) - M),$$

$$(5.4) \quad \frac{dV_V}{dt} = \frac{1}{\tau_n} (F(V_V) + c_p \kappa),$$

$$(5.5) \quad \frac{dV_D}{dt} = \frac{1}{\tau_n} (F(V_D) - c_p \kappa).$$

**5.1.2. Nondimensionalization.** Nondimensionalizing time  $\tilde{t} = \tau_m t$  and curvature  $K = c_p \kappa$ , we denote  $\dot{X} = dX/d\tilde{t}$  (for  $X = M, K, V_V, V_D$ ) so that

$$(5.6) \quad \tau \dot{K} = -K + \frac{c}{2} M,$$

$$(5.7) \quad \dot{M} = 2(V_D - V_V) - M,$$

$$(5.8) \quad \dot{V}_V = \frac{\tau_m}{\tau_n} (F(V_V) + K),$$

$$(5.9) \quad \dot{V}_D = \frac{\tau_m}{\tau_n} (F(V_D) - K),$$

where  $\tau = \tau_b/\tau_m$  is the the nondimensional timescale and  $c = c_m c_p$  is the nondimensional feedback strength. Note that  $M$ ,  $V_V$ , and  $V_D$  are already arbitrary and effectively nondimensional. If we differentiate equation 5.6 with respect to  $\tilde{t}$ , we obtain

$$(5.10) \quad \begin{aligned} \tau \ddot{K} &= -\dot{K} + \frac{c}{2} \dot{M} \\ &= -\dot{K} + \frac{c}{2} (2(V_D - V_V) - M) \\ &= -\dot{K} + \frac{c}{2} \left( 2(V_D - V_V) - \frac{2}{c} (\tau \dot{K} + K) \right). \end{aligned}$$

Thus the neuromechanical oscillator module can be reduced to:

$$(5.11) \quad \tau \ddot{K} + (1 + \tau) \dot{K} + K = c(V_D - V_V)$$

$$(5.12) \quad \dot{V}_V = \frac{\tau_m}{\tau_n} (F(V_V) + K),$$

$$(5.13) \quad \dot{V}_D = \frac{\tau_m}{\tau_n} (F(V_D) - K).$$

**5.1.3. Singular Limit Reduces Neural Activity to Discrete States.** In Chapters 2-4, we assumed that the neural activity timescale was the fastest process in the system. We used the value  $\tau_n = 0.01$  s, while  $\tau_m$  was typically between 0.05 and 0.25 s. Here, we take the singular limit  $\tau_n/\tau_m \rightarrow 0$ , so that the neural activities  $V_V$  and  $V_D$  are always at quasi-steady state, i.e.,  $K = f(V_V) = V_V - aV_V^3 + I$ , and  $-K = f(V_D) = V_D - aV_D^3 + I$ . Figure 5.1(a) shows the quasi-steady voltage states of equations 5.12-5.13. In the singular limit, the neural activity rapidly relaxes to one of two stable branches of the slow manifold. The neural activity flows along the stable branch until it reaches the end of the branch at  $\pm 1/\sqrt{3a}$ , which corresponds to the “knees” of  $f(V)$  (equation 2.11). At the end of this stable branch, the neural activity will jump to the other stable branch of the slow manifold.

Note that the two stable branches of the slow manifold represent an “active” state with  $V > 0$  and an “inactive” state with  $V < 0$ , and along each branch the value of  $V$  doesn’t change much. To reduce the model further, we replace these stable branch values with either an active ( $S = 1$ ) or inactive ( $S = 0$ ) state. That is, we augment the effects of the neurons with a unit step function so that

$$(5.14) \quad \tau \ddot{K} + (1 + \tau) \dot{K} + K = c(S_D - S_V),$$

where the states of the ventral/dorsal B-class neurons are given by

$$(5.15) \quad S_V = u(V_V), \quad S_D = u(V_D),$$

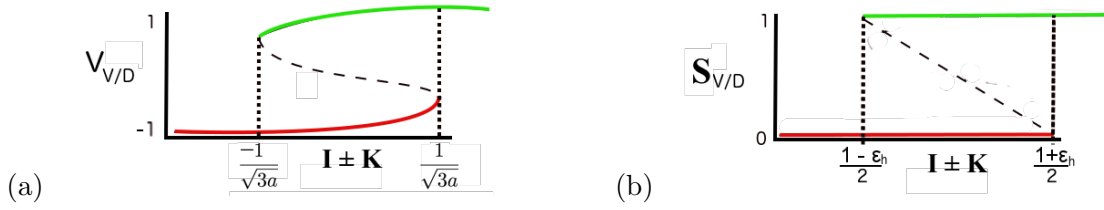


FIGURE 5.1. (a) The steady voltage states of the continuous differential equations 5.12-5.13 for the B-class neurons. (b) The discrete states after putting the steady voltage states through the unit step function  $u(x)$  (equation 5.16) and reexpressing the input thresholds.

and  $u(x)$  is the unit step function

$$(5.16) \quad u(x) = \begin{cases} 1, & \text{if } x > 0, \\ 0, & \text{if } x \leq 0. \end{cases}$$

The neural activity jumps between stable branches of the slow manifold and switches on or off ( $S = 1$  or  $S = 0$ ) depending on the input ( $I \pm K$ ) and their current state. Figure 5.1(b) shows the quasi-steady states  $S = u(V)$ . The input thresholds at which the neural activity jumps between stable branches are denoted by  $(1 \pm \varepsilon_h)/2$ , so that the location of the thresholds depends *linearly* on the parameter  $\varepsilon_h$ . That is,  $\varepsilon_h$  is the size of the range of inputs for which the neurons exhibit hysteresis. Because the curvature  $K$  of the module changes over time while the AVB input  $I$  is constant, these input thresholds are essentially proprioceptive *curvature thresholds* for each neuron. In nondimensional form, the proprioceptive curvature thresholds  $K_{off}^V = -I - \varepsilon_h/2$ ,  $K_{on}^V = -I + \varepsilon_h/2$ ,  $K_{off}^D = I + \varepsilon_h/2$ ,  $K_{on}^D = I - \varepsilon_h/2$ . If the curvature  $K$  of the module reaches one of these thresholds, then the corresponding neuron (ventral/dorsal) will jump to the corresponding steady-state (on/off), e.g., at  $K_{off}^V$ , the ventral neuron will jump to  $S_V = 0$ , the “off” state, if it is on or remain off if it is already off. Without loss of generality, we assume that  $0 < I < \varepsilon_h/2$  so that

$$(5.17) \quad K_{off}^D > K_{on}^V > 0 > K_{on}^D > K_{off}^V.$$

Other values of  $I$ ,  $\varepsilon_h$  will result in different orderings of the curvature thresholds, some of which will result in similar neuromechanical oscillations and others which cannot.

This reduces the neuromechanical oscillator to the 2-dimensional hybrid system

$$(5.18) \quad \tau \ddot{K} + (1 + \tau) \dot{K} + K = c(S_D - S_V)$$

$$(5.19) \quad S_V(\tilde{t}) = \begin{cases} 0, & K(\tilde{t}) \leq K_{off}^V \\ 0, & K_{off}^V < K(\tilde{t}) < K_{on}^V \text{ and } \lim_{t \rightarrow \tilde{t}_-} S_V(t) = 0 \\ 1, & K_{off}^V < K(\tilde{t}) < K_{on}^V \text{ and } \lim_{t \rightarrow \tilde{t}_-} S_V(t) = 1 \\ 1, & K_{on}^V \leq K(\tilde{t}) \end{cases},$$

$$(5.20) \quad S_D(\tilde{t}) = \begin{cases} 1, & K(\tilde{t}) \leq K_{on}^D \\ 1, & K_{on}^D < K(\tilde{t}) < K_{off}^D \text{ and } \lim_{t \rightarrow \tilde{t}_-} S_D(t) = 1 \\ 0, & K_{on}^D < K(\tilde{t}) < K_{off}^D \text{ and } \lim_{t \rightarrow \tilde{t}_-} S_D(t) = 0 \\ 0, & K_{off}^D \leq K(\tilde{t}) \end{cases}.$$

**5.1.4. Phase Plane Dynamics.** Figure 5.2(a,b,c) shows example phase planes of the system (equations 5.18-5.20) with parameters  $c = 5, \tau = 5, I = 0.75, \varepsilon_h = 5.5$  for (a)  $S_D - S_V = 0$ , (b)  $S_D - S_V = 1$ , and (c)  $S_D - S_V = -1$ . In all three cases, there is a globally stable equilibrium at  $K = c(S_D - S_V), M = 0$  (see Appendix C.1). These equilibria correspond to: (a) a zero curvature module; (b) a positive curvature module (bent towards the dorsal side); and (c) a negative curvature module (bent towards the ventral side).

For some initial conditions and parameter regimes, the system settles at one of these equilibrium points. For other initial conditions and parameter regimes, trajectories cross a curvature threshold (e.g.  $K_{on}^V$ ) before reaching an equilibrium point, which then changes the phase plane dynamics including the target equilibrium point. An example of this is shown in Figure 5.2(d), where initial condition (A) reaches the curvature threshold at  $K_{off}^D$  but initial condition (B) flows to the equilibrium point instead. For certain initial conditions and parameters, the system can get caught in a loop of chasing these switching equilibria, and thus undergo oscillations.

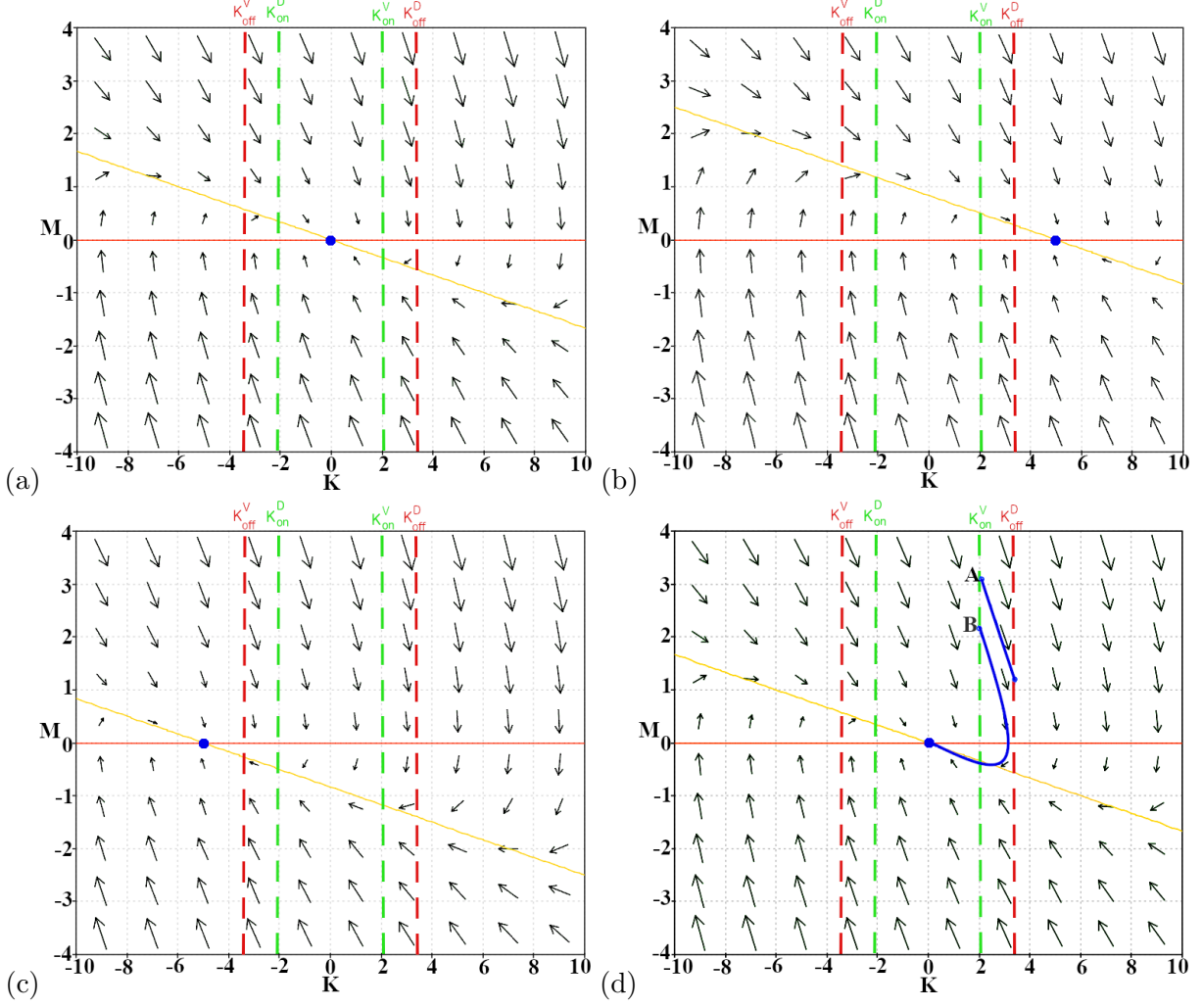


FIGURE 5.2. Phase planes for equation 5.18 with parameters  $c = 5, \tau = 5, I = 0.75, \varepsilon_h = 5.5$  and fixed  $S_D, S_V$ . (a) For  $S_D - S_V = 0$ , there is a stable equilibrium at  $K = 0, M = 0$ . (b) For  $S_D - S_V = 1$ , there is a stable equilibrium at  $K = c, M = 0$ . (c) For  $S_D - S_V = -1$ , there is a stable equilibrium at  $K = -c, M = 0$ . (d) Sample trajectories in the  $S_D - S_V = 0$  phase plane. Some initial conditions (A) flow to the curvature threshold at  $K_{off}^D$ , which changes the equilibrium point and phase plane dynamics. Other initial conditions (B) do not reach the curvature threshold and instead flow to the equilibrium point at  $K = M = 0$ .

## 5.2. 1-D Map Captures Limit Cycle Dynamics

**5.2.1. 1-D Map Construction.** We define a return map  $\alpha_2 = F(\alpha_0)$  that takes an initial condition along the Poincaré section  $K = K_{off}^V, M = \alpha_0 < 0, S_D = 1, S_V = 0$  until it returns to the Poincaré section at  $M = \alpha_2 < 0$ , as defined by the flow of equations 5.18-5.20. To do this,

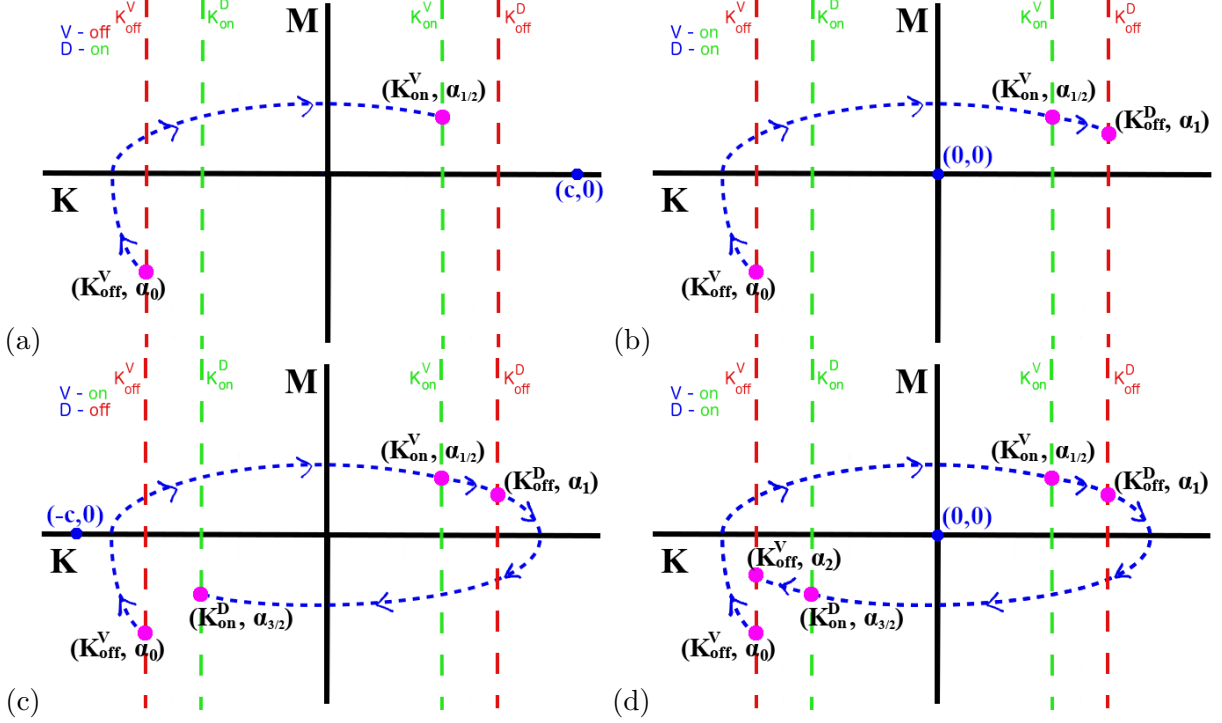


FIGURE 5.3. (a) Map 1 flows the solution forward from initial condition  $(K = K_{off}^V, M = \alpha_0)$  to the first curvature threshold at  $(K_{on}^V, \alpha_{1/2})$ . (b) Map 2 flows the solution forward from initial condition  $(K_{on}^V, \alpha_{1/2})$  to the next curvature threshold at  $(K_{off}^D, \alpha_1)$ . (c) Map 3 flows the solution forward from initial condition  $(K_{off}^D, \alpha_1)$  to the next curvature threshold at  $(K_{on}^D, \alpha_{3/2})$ . (d) Map 4 flows the solution forward from initial condition  $(K_{on}^D, \alpha_{3/2})$  to the final curvature threshold at  $(K_{off}^V, \alpha_2)$ .

we solve the system (equations 5.18-5.20) piecewise, where each solution piece/branch is for fixed neural states, and appropriately piece the solutions together when the neural states switch on/off. The return map consists of intermediate maps along each solution branch that are given by implicit expressions in Appendix C.2.

Figure 5.3 illustrate this process by following a specific trajectory of the system. Starting with a specific initial condition along the Poincaré section  $K = K_{off}^V, M = \alpha_0 < 0, S_D = 1, S_V = 0$ , we use the system solution (equation C.3) with equilibrium  $c(S_D - S_V) = c$  to flow the solution forward in time until the system reaches the curvature threshold at  $(K_{on}^V, \alpha_{1/2})$ , as in Figure 5.3(a). This constructs a map from  $\alpha_0 < 0$  to  $\alpha_{1/2}$ , i.e.,

$$(5.21) \quad \alpha_{1/2} = F_1(\alpha_0),$$

which is given by an implicit expression in Appendix C.2.1.

When the system crosses the curvature threshold  $K_{on}^V$ , the ventral B neuron turns on, i.e.,  $S_V = 1$ , thus the equilibrium shifts to  $c(S_D - S_V) = 0$ . Figure 5.3(b) shows the trajectory continuing from  $K = K_{on}^V, M = \alpha_{1/2}, S_D = 1, S_V = 1$  until the next curvature threshold at  $(K_{off}^D, \alpha_1)$ . This constructs a map from  $\alpha_{1/2}$  to  $\alpha_1$ , i.e.,

$$(5.22) \quad \alpha_1 = F_2(\alpha_{1/2}),$$

which is given by an implicit expression in Appendix C.2.2.

When the system crosses the curvature threshold  $K_{off}^D$ , the ventral D neuron turns off, i.e.,  $S_D = 0$ , thus the equilibrium shifts to  $c(S_D - S_V) = -c$ . Figure 5.3(c) shows the trajectory continuing from  $K = K_{off}^D, M = \alpha_1, V_D = 0, V_V = 1$  until the next curvature threshold at  $(K_{on}^D, \alpha_{3/2})$ . When the system crosses the curvature threshold  $K_{on}^D$ , the ventral D neuron turns on, i.e.,  $S_D = 1$ , thus the equilibrium shifts to  $c(S_D - S_V) = 0$ . Figure 5.3(d) shows the trajectory continuing from  $K = K_{on}^D, M = \alpha_{3/2}, V_D = 1, V_V = 1$  until the return to the Poincaré section at  $(K_{off}^V, \alpha_2)$ .

By symmetry, the rest of the map can be constructed by

$$(5.23) \quad \alpha_{3/2} = -F_1(-\alpha_1),$$

$$(5.24) \quad \alpha_2 = -F_2(-\alpha_{3/2}),$$

which are given by implicit expressions in Appendix C.2.3-4.

Piecing the solutions along each branch together generates a Poincaré map from initial condition  $K = K_{off}^V, M = \alpha_0, V_D = 1, V_V = 0$  to the next intersection with this curvature threshold  $K = K_{off}^V$  from the right, i.e., to  $K = K_{off}^V, M = \alpha_2 < 0, V_D = 1, V_V = 0$ . Essentially, we map  $M = \alpha_0$  to  $M = \alpha_2$  after a full neuromechanical loop. This 1-D map is given by

$$(5.25) \quad \alpha_2 = F(\alpha_0) = -F_2(F_1(-F_2(F_1(\alpha_0)))).$$

If the system converges to a stable equilibrium along one of the solution branches for some initial conditions (as in Figure 5.2(d)), then the map is not defined. Fixed points of the full 1-D map,

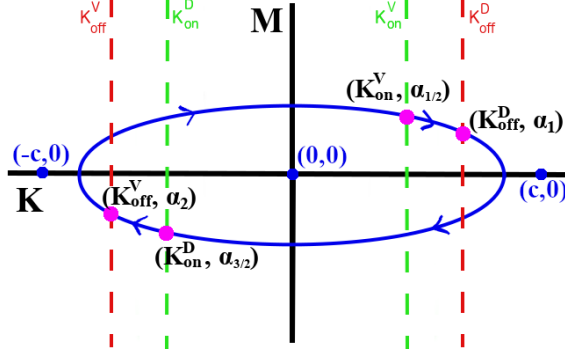


FIGURE 5.4. The limit cycle in the  $M, K$ -phase plane. The 1-D Map takes initial condition  $K = K_{off}^V, M = \alpha_0, V_D = 1, V_V = 0$  and maps it to the next intersection with the curvature threshold  $K = K_{off}^V$  after a full loop, i.e., to  $K = K_{off}^V, M = \alpha_2, V_D = 1, V_V = 0$ .

$\alpha^* = F(\alpha^*)$ , correspond to limit cycles. Figure 5.4 shows a qualitative representation of the full limit cycle in the  $M, K$ -phase plane.

**5.2.2. Limit Cycle Properties from the 1-D Map.** The 1-D Map gives us a quick way to assess when limit cycles exist and how parameters effect their periods and amplitudes. The fixed points of the map,  $\alpha^* = F(\alpha^*)$ , correspond to limit cycles in the reduced neuromechanical oscillator model (equations 5.18-5.20), and they are stable iff  $|F'(\alpha^*)| < 1$ . Figure 5.5(a) shows  $\alpha_2 = F(\alpha_0)$  for a range of  $\alpha_0$  and with parameters  $I = 0.01, \varepsilon_h = 2, c = 10, \tau = 5$ . There is only one fixed point  $\alpha^*$ , and it is stable since  $|F'(\alpha^*)| < 1$ . This single stable fixed point corresponds to a single stable limit cycle, which indicates that the reduced oscillator model is fundamentally different than the full neuromechanical oscillator model of Chapter 4, which also has an unstable limit cycle. Figure 5.5(a) also shows that the map is remarkably flat, which indicates that if one exists, a limit cycle will be stable and the system will converge very quickly to it. Figure 5.5(b) shows that not only is the full map  $\alpha_2 = F(\alpha_0)$  very flat, but the intermediate maps are flat as well, indicating that each branch of the map is strongly contractive.

After finding the fixed point  $\alpha^*$  of the 1-D map, we can compute the period and amplitude of the limit cycle from the piecewise general solution (see Appendix C.4 for details). Figure 5.6 shows the emergent period and amplitude of the limit cycle as a function of the nondimensional parameters, the feedback strength  $c$  and timescale  $\tau$ , with  $\varepsilon_h = 2$  and  $I = 0.01$  or  $I = 0.001$ . Empty values correspond to parameter regimes with no fixed point  $\alpha^*$  in the 1-D map, i.e., with no limit

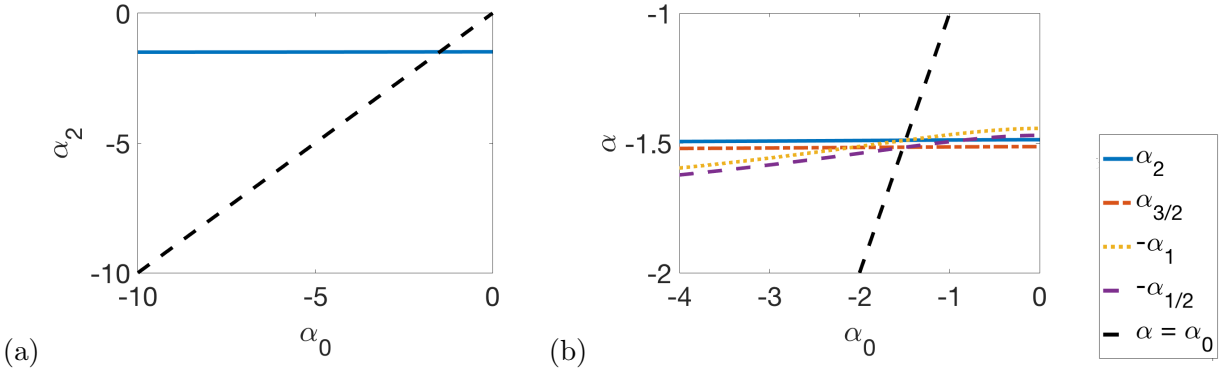


FIGURE 5.5. (a) The Poincaré map  $\alpha_2 = F(\alpha_0)$  yields a single stable fixed point  $\alpha^*$ , which the system converges to for  $\alpha_0 < 2$ . (b) The intermediate maps. Other parameters here are  $I = 0.01, \varepsilon_h = 2, c = 10, \tau = 5$ .

cycle in the system. Figure 5.6 shows a quadratic-like relationship between  $\log(\tau)$  and  $c$  for the existence of limit cycles. Decreasing  $I$  shifts the limit-cycle-existence-boundary to lower  $c$  values because  $c > K_{off}^D = I + \varepsilon_h/2$  is necessary for a solution (see Appendix C.3 for details). The limit-cycle-existence boundary is remarkably similar to the stability diagrams in Figure 4.7(a-b) for the full neuromechanical oscillator model in Chapter 4. Recall that we also showed in Chapter 4 that the boundary that marked the existence of oscillations in these stability diagrams was constant with the product  $c_m c_p$ , which is the nondimensional feedback strength here. Thus, this 1-D map seems to capture the mechanistic underpinnings of the existence of oscillations in the full neuromechanical oscillator model.

Figure 5.6(a,b) show that increasing the nondimensional feedback strength  $c$  decreases the period of the oscillation, which is similar to the effects of the feedback strengths  $c_m$  and  $c_p$  on the period of the full neuromechanical oscillator in Chapter 4. Figure 5.6(a,b) also show that increasing  $\tau$  increases the period, which is similar to the effects of both the timescales  $\tau_b$  and  $\tau_m$  on the full neuromechanical oscillator period (see Figure 4.6(a)). Figure 5.6(c,d) show that increasing the nondimensional feedback strength  $c$  increases the amplitude, which is similar to the effect of the feedback strength  $c_m$  in Chapter 4. Figure 5.6(c,d) shows that the relationship between  $\tau$  and the curvature amplitude is more complex. For  $\tau > 1$  ( $\log_{10} \tau > 0$ ), increasing  $\tau$  decreases the amplitude, and for  $\tau < 1$ , decreasing  $\tau$  decreases the amplitude. This is similar to how the

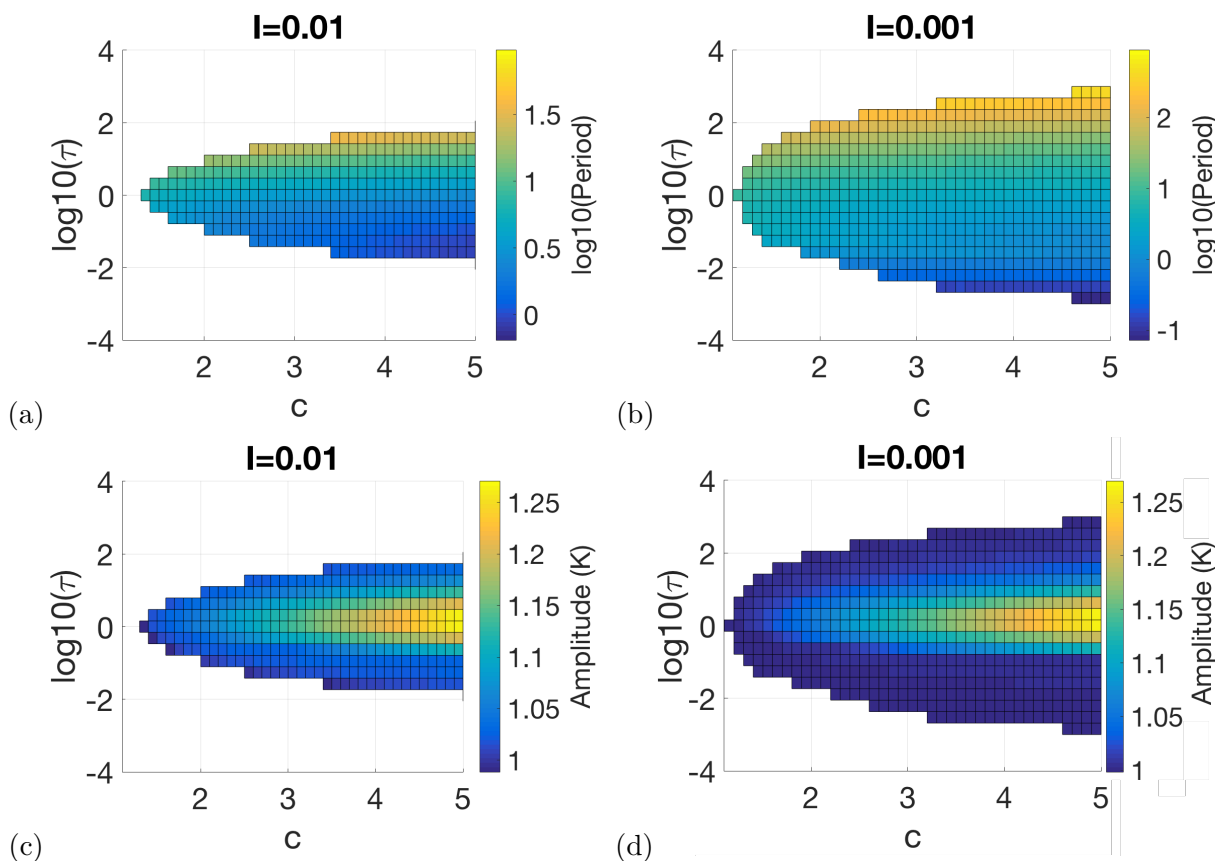


FIGURE 5.6. (a,b) Log10 of the period vs. the nondimensional feedback strength  $c$  and the nondimensional timescale  $\tau$  for (a)  $I = 0.01$  and (b)  $I = 0.001$ . Increasing  $c$  decreases the period of the oscillation, and increasing  $\tau$  increases the period. (c,d) The amplitude (in  $K$ ) vs. the nondimensional feedback strength  $c$  and the nondimensional timescale  $\tau$  for (c)  $I = 0.01$  and (d)  $I = 0.001$ . . Increasing  $c$  increases the amplitude, but the relationship between  $\tau$  and the amplitude is more complex. For  $\tau > 1$  ( $\log_{10} \tau > 0$ ), increasing  $\tau$  decreases the amplitude, and for  $\tau < 1$ , decreasing  $\tau$  decreases the amplitude.

muscle activity timescale  $\tau_m$  affected the curvature amplitude in the full neuromechanical model (see Figure 4.6(b)).

In summary, this simple 1-D Poincaré map captures the full limit cycle dynamics of the reduced oscillator model, which captures most of the dynamics of the full neuromechanical oscillator model. This 1-D map provides a framework for further analysis of the mechanisms of oscillation in the neuromechanical oscillator. We could trace out explicit parameter dependence of the bifurcations, period, and amplitude of the reduced oscillator model. The existence of oscillations, which in

both the neuromechanical oscillator model and the reduced oscillator model depends nonlinearly on the timescales  $\tau_b$  and  $\tau_m$  and the feedback strengths  $c_m$  and  $c_p$ , is determined by the existence of solutions to the nonlinear maps  $F_1(\alpha), F_2(\alpha)$ . Thus, a deeper analysis of the dependence of these maps on  $c = c_m c_p$  and  $\tau = \tau_b / \tau_m$  would give insight into the biophysical mechanisms behind the existence of oscillations in the neuromechanical oscillator model. Another future direction is to perturb this reduced system in any direction and solve piecewise along the limit cycle to compute the phase response curve analytically. An analytic PRC could give deeper insight into how the biophysical mechanisms of the oscillator shape the PRC and thus the coordination of the neuromechanical model.

## CHAPTER 6

### Chains of Different Numbers of Modules

In Chapter 3, we examine the stable phase differences between neighboring modules in a two-oscillator model and a six-oscillator model. In both cases, we show that the general trend of each pairwise phase difference— decreasing from near-synchrony towards antiphase as external fluid viscosity  $\mu_f$  increases— underlies the wavelength trend of gait adaptation. However, in the six-oscillator model (Ch. 3.4), the pair-wise phase differences are not uniform across the body. In particular, at low and zero fluid viscosity the phase differences of the six-oscillator model are spread out between roughly 0.85 and 0.95, while for the same parameters the two-oscillator model has a phase difference of roughly 0.9. Here, we examine chains of different numbers of oscillators in order to give insight into how these results depend on the number of oscillators.

We simulated the phase model and neuromechanical model with  $N$  oscillator modules, where  $N = 2 - 6, 10, 12, 20,$  and  $25$ . Figure 6.1 shows the stable pair-wise phase differences as external fluid viscosity  $\mu_f$  is varied for  $N = 2 - 6$ , and Figure 6.2 shows the same for  $N = 10, 12, 20,$  and  $25$ . At low fluid viscosity, where the phase differences are primarily determined by the neural coupling, the pair-wise phase differences are spread out between roughly 0.8 and 0.95. As fluid viscosity increases, these pair-wise phase differences generally decrease, though at non-uniform rates. That is, the dependence of each pair-wise phase difference on the fluid viscosity depends on the position of that pair of oscillators in the body.

The ordering of the varying pair-wise phase differences is also determined by the position in the chain: at low viscosity, the pair at the head ( $\phi_1$ ) is at the lowest phase difference (near 0.8), the pair at the tail ( $\phi_N$ ) are at the highest phase differences (near 0.95), and the rest are ordered by position at intermediate phase differences between these two. This pattern holds independent of  $N$ . However, at high fluid viscosity, where mechanical coupling is stronger, the ordering of pair-wise phase differences is rearranged, and there is not a consistent pattern between chains.

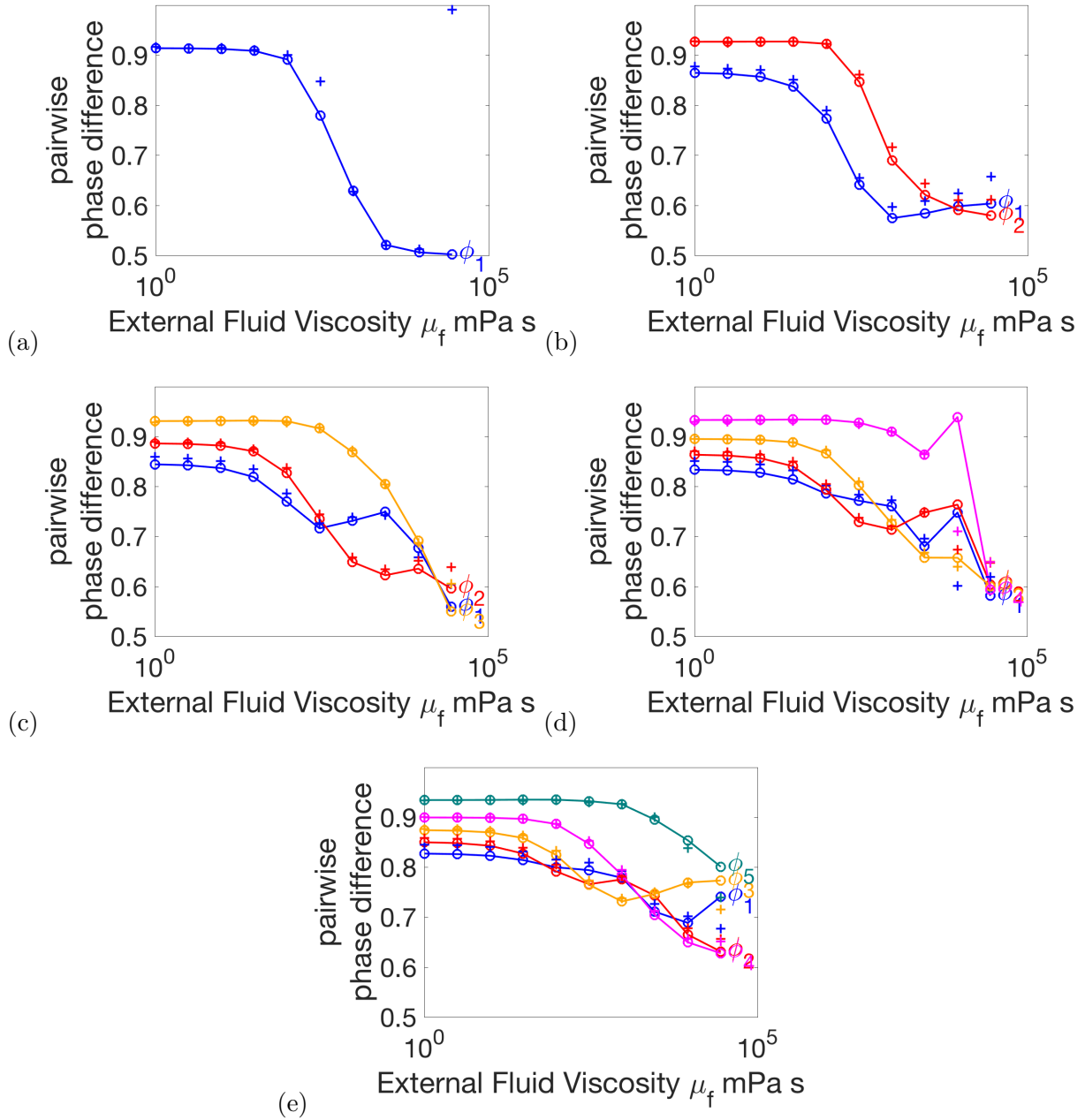


FIGURE 6.1. Stable pair-wise phase differences of the phase model (lines, circles) and neuromechanical model (crosses) as a function of external fluid viscosity  $\mu_f$  in the  $N$ -oscillator chain with fixed module length  $\ell$ .  $N = 2 - 6$  for cases (a)-(e).

Figure 6.3 shows the wavelengths computed from the above  $N$ -module phase differences (see Appendix A.1 for details). In the  $N$ -oscillator cases considered here, the wavelength trends are decreasing, though they don't always capture the quantitative trend observed experimentally as

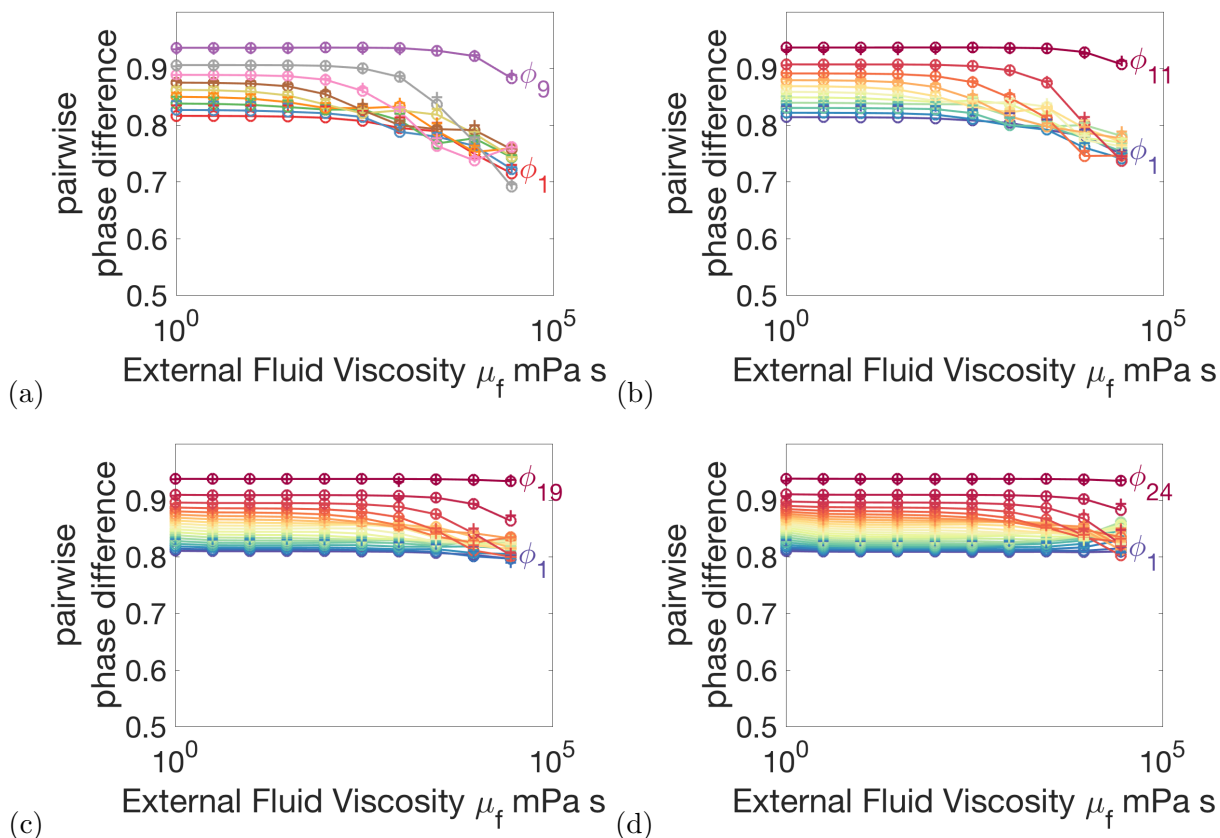


FIGURE 6.2. Stable pair-wise phase differences of the phase model (lines, circles) and neuromechanical model (crosses) as a function of external fluid viscosity  $\mu_f$  in the  $N$ -oscillator chain with fixed module length  $\ell$ .  $N = 10, 12, 20, 25$  for cases (a)-(d).

in Figure 2.2. For each of these simulations, we used the same neural coupling parameters that were used in Chapter 2.4.1 to generate the data for Figure 2.2,  $\varepsilon_g = 0.017$  and  $\varepsilon_p = 0.05$ . The wavelength trend is steepest for small  $N$ , and flattest for large  $N$ , which suggests that as  $N$  increases, the mechanical coupling strength is weakening relative to the neural coupling strength.

In Chapter 2.4.3, we show how changing the neural coupling strengths  $\varepsilon_g$  and  $\varepsilon_p$  affects the wavelength trend in the six-oscillator neuromechanical model. Here, we investigate how changing the neural coupling strengths affects the wavelength trend for a chain with a different number of oscillators. Figure 6.4 shows the wavelengths of the 20-oscillator phase model with different gap-junctional coupling strengths,  $\varepsilon_g$ . For each  $\varepsilon_g$ , the proprioceptive coupling strength  $\varepsilon_p$  was fit to match the wavelength in water (1.5 bodylengths). For  $\varepsilon_g = 0.001$  (and  $\varepsilon_p = 0.0035$ ), the wavelength

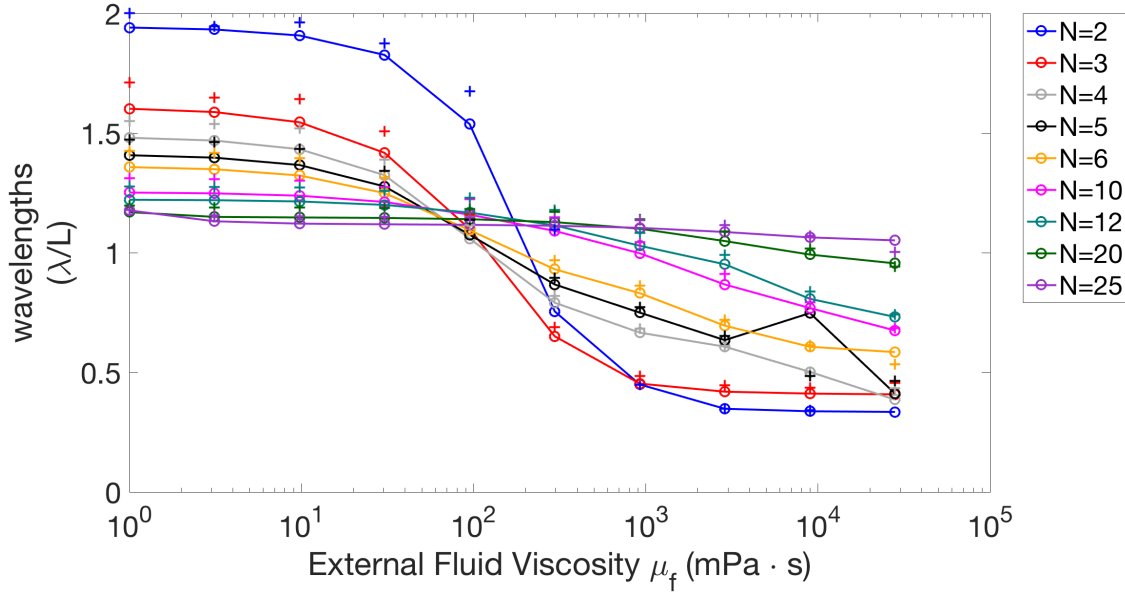


FIGURE 6.3. Wavelength ( $\lambda/L$ ) as a function of external fluid viscosity  $\mu_f$  for the  $N$ -oscillator chain. Wavelength computed from the phase model (lines, circles) and the neuromechanical model (crosses).

trend closely resembles the data of Fang-Yen et al. 2010 [15]. This indicates that, independent of the number of oscillators  $N$ , the model can quantitatively capture the wavelength trend by altering the neural coupling strengths to account for the changing mechanical coupling strength with  $N$ .

For the  $N$ -oscillator cases considered here, we can generally find gait adaptation; however the model requires different neural parameters for different numbers of oscillators in order to get similar wavelength trends over this range of external fluid viscosities. Thus, the main conclusions of Chapters 2 and 3 do not depend on the number of oscillators considered; by changing model parameters, the model can capture and explain gait adaptation independent of the number of oscillators.

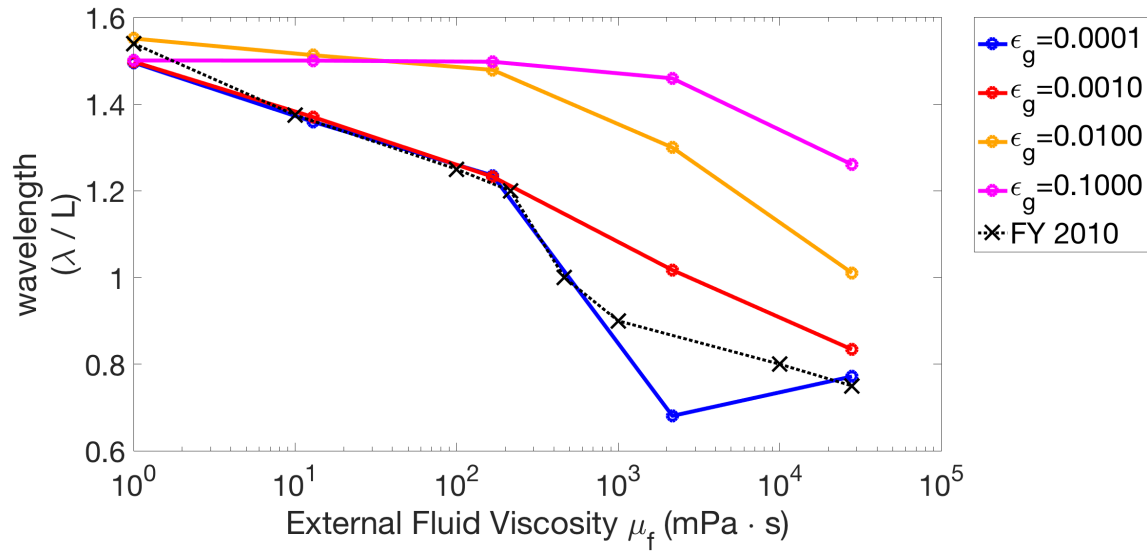


FIGURE 6.4. Wavelength ( $\lambda/L$ ) as a function of external fluid viscosity  $\mu_f$  for the 20-oscillator chain for various gap-junctional coupling strengths  $\epsilon_g$ . Proprioceptive coupling strengths  $\epsilon_p$  were chosen to match the wavelength in water (1.5 bodylengths). Data from Fang-Yen et al. 2010 [15] in black X's.

## CHAPTER 7

### Discussion and Conclusions

The analysis of the neuromechanical model presented here identifies a mechanism for gait adaptation to increasing fluid viscosity in *C. elegans* forward locomotion. In Chapter 2, we model the *C. elegans* forward locomotion system as a chain of neuromechanical oscillators coupled by body mechanics, proprioceptive coupling, and gap-junctional coupling. Using the theory of weakly coupled oscillators, we exploit the modular structure of the forward locomotion system to analyze the relative contributions of the various coupling modalities. In Chapter 3, we show that proprioceptive coupling between modules leads to a posteriorly-directed traveling wave with a characteristic wavelength. Gap-junction coupling between neural modules promotes synchronous activity (long wavelength), and mechanical coupling promotes a high spatial frequency (short wavelength). The wavelength of *C. elegans*' undulatory waveform is set by the relative strengths of these three coupling forms. As the external fluid viscosity increases, the mechanical coupling strength increases and the wavelength decreases, as observed experimentally.

By tuning only a few coupling parameters, the model can robustly capture the gait adaptation seen in experiments [3, 15, 49] over a wide range of mechanical parameters. The robustness of the model is of particular importance because the experimental measurements of mechanical body parameters vary widely. Our model suggests relationships between the parameters that need to hold in order to get the appropriate coordination and wavelength trend. In particular, the effective mechanical body timescale  $\tau_b = \mu_b/k_b$  (the ratio of body viscosity to stiffness) plays a key role. In Chapter 2, we show that our model yields the correct coordination trend across the entire range of reported mechanical parameters provided that  $\tau_b$  is in the range 0.07 – 1 s. Furthermore, our model suggests that generally the muscle activity timescale  $\tau_m$  must be shorter than the effective body mechanics timescale  $\tau_b$ . In other words, the system must generate contractile forces faster than the body responds. Otherwise, the model suggests that there will not be a traveling wave of neuromechanical activity, and therefore no effective locomotion for high external fluid viscosities.

The coordination trend of the full neuromechanical model can be inferred from the properties of the individual neuromechanical oscillator modules. In Chapter 4, we show how model parameters affect the period, amplitude, existence of oscillations, and phase response properties of the single neuromechanical module. We show that the oscillations are robust over a wide range of parameters and the bifurcation structure remains largely the same as well. Different parameters give different phase response properties, however these differences translate into generally the same G-functions and thus the same coordination. On the other hand, changing the ordering of the timescales  $\tau_m$  and  $\tau_n$  changes the G-functions and thus the coordination in the two-oscillator model. The muscle activity timescale  $\tau_m$  must generally be lower than the effective body mechanics timescale  $\tau_b$  in order to get the appropriate coordination in the G-functions, as observed in Chapters 2 and 3. This major coordination change is the result of subtle changes in the phase response and limit cycle properties of the neuromechanical oscillator module, so understanding the underlying biophysical processes would provide additional insight into the mechanisms of coordination.

In Chapter 5, we present a simplified version of the neuromechanical oscillator model that is more amenable to analysis, and we build a framework to more deeply understand the parametric dependence of the neuromechanical oscillator module. By appropriate assumptions about the neuromechanical oscillator module, including linear contractile forces and instantaneous switches between neural states, we reduce the oscillator module to a form that is analytically piecewise-solvable. This allows us to construct a 1-D Poincaré map that captures the limit cycle dynamics. This 1-D map shows how the feedback strengths and system timescales shape the existence of oscillations and influence the period and amplitude of the limit cycle. The map also provides a framework for further analysis of the mechanisms of oscillation and phase response properties of the neuromechanical oscillator.

In our model, the wavelength trend of gait adaptation can be explained by the general trend of the pair-wise phase differences between oscillator modules; however, the numbers of oscillators in the model is a key parameter that affects the wavelength trend. In Chapter 6, we show that the model requires different neural parameters for different numbers of oscillators in order to get similar wavelength trends over the considered range of external fluid viscosities. Thus, the model's ability to capture gait adaptation does not depend on the number of oscillators considered.

Our model is similar in structure to previous modeling work by Boyle et al. [5]. In particular, the neural module is very similar to Boyle et al. [5]. On the other hand, the description of the muscle dynamics and body mechanics are more complex in the Boyle et al. model [5]. Boyle et al. [5] also captures gait adaptation, and the large number of parameters and variables of the model allows it to more closely match the wavelengths, amplitudes, and undulation frequencies observed experimentally. However, the complexity of the model also limits the ability to systematically assess the relative roles of body mechanics and proprioception in coordination. A key difference between our model and Boyle et al. [5] is the number of neural modules: Boyle et al. [5] considers a chain of 12 modules in line with the number of VB neurons (11), whereas our model considers a chain of 6 modules in line with the number of DB neurons (7). However, both assumptions are reasonable as it is unclear what the correct “number of modules” is in the motor circuit. Furthermore, we have also shown in Chapter 6 that the main conclusions of our model do not depend on the choice of the number of oscillators.

Another difference between our model and Boyle et al. [5] is in the sign, directionality, and extent of nonlocal proprioception. The directionality of proprioception in Boyle et al. [5] is consistent with the directionality of undifferentiated processes extending posteriorly from the B-class neurons, which are postulated to be responsible for proprioception [58]. We take the directionality of proprioception to be consistent with the functional directionality suggested by the experiments of Wen et al. [51]. Note that symmetry arguments can be made that reversing both the sign and direction of the nonlocal proprioception will not change the behavior of the models, as Denham et al. [11] points out. The extent of proprioception in Boyle et al. [5] is over half a bodylength, and Denham et al. [11] showed that the larger the proprioceptive range, the longer the undulatory wavelength their model. We considered only nearest-neighbor proprioception, which is sufficient to achieve the long-wavelength undulations in water because of our inclusion of gap-junctional coupling that promotes synchrony between the modules and thus long wavelengths.

*C. elegans* gait adaptation is marked by a shortening of the wavelength and a decrease in undulation frequency with increasing fluid viscosity [3, 15, 49]. Boyle et al. [5] captures both wavelength and frequency adaptation as a function of external fluid viscosity. Our model captures the quantitative trend in wavelength and the qualitative trend in frequency. However, the model

frequency range is only 1.7–1.6 Hz as fluid viscosity is increased as opposed to the range 1.7–0.3 Hz given in Fang-Yen et al. [15]. Many differences between Boyle et al. [5] and our model may account for this discrepancy in frequency adaptation; these differences include nonlinear and heterogeneous mechanical body parameters and a more sophisticated muscle model.

Our model assumes that the undulatory gait emerges from a chain of neuromechanical oscillators coupled by both body mechanics and neural connectivity. However, there are several other hypotheses for how the undulatory gait is generated and coordinated [19]: (1) a separate head circuit contains a CPG that drives the propagated bending wave along the body, and (2) a network of coupled CPGs generates and coordinates the bending wave in a feed-forward manner. Modeling work by Olivares et al. [41] shows that the anatomical structure of the neural circuitry of *C. elegans* can be tuned to produce CPG-driven locomotion. However, there is no experimental evidence to date for such spontaneous isolated neural activity [10,58]. Furthermore, recent experiments by [16] showed that *C. elegans* is capable of decoupled “two-frequency undulations”. By suppressing neural activity in the neck region, the head and body can undulate seemingly independent of one another at different frequencies (the head slower and the body faster). This evidence supports the presence of multiple neural or neuromechanical oscillators.

In the present study, the theory of weakly coupled oscillators is used to identify the roles of the various coupling modalities in generating coordination for forward locomotion in *C. elegans*. The phase models derived by the theory of weakly coupled oscillators capture the influence of one oscillating module on another through the interaction functions  $H(\phi)$ , which are convolution-like integrals of the coupling input and the corresponding phase response function  $Z(t)$  of the individual modules. Therefore, our findings could be validated by experimentally measuring the phase-response curves of the neuromechanical circuit [37]. This could be achieved using a combination of optogenetic techniques and mechanical stimuli to perturb the system [16,27,51]. Note also that the structure of the phase equations could be exploited to further dissect out the biophysical mechanisms that underlie coordination of the undulatory motion of *C. elegans*. Because the shapes of the PRCs and the coupling signals combine to determine the interaction functions, a systematic analysis of how cellular and synaptic dynamics [57], muscle properties, and body mechanics shape

the PRCs and coupling signals would provide further insight into the integrated neuromechanical mechanisms underlying the generation and coordination of locomotion.

## APPENDIX A

### Neuromechanical Model Details

#### A.1. Defining Wavelength

**A.1.1. Constant Wavespeed.** For a wavelength of undulation in the neuromechanical model traveling front-to-back at constant speed, the phase is defined as

$$(A.1) \quad \theta(x, t) = \left( \frac{t}{T} - \frac{x}{\lambda} \right) \bmod 1$$

The phase corresponding to module  $k$  ( $k = 1, \dots, 6$ ) centered at body position  $x = \ell(k - 1/2)$  is

$$(A.2) \quad \theta_k = \left( \frac{t}{T} - \frac{\ell}{\lambda} \left( k - \frac{1}{2} \right) \right) \bmod 1,$$

where  $T$  is the oscillator period. Thus, the constant phase difference  $\phi^*$  is

$$(A.3) \quad \phi^* = (\theta_{k+1} - \theta_k) \bmod 1 = \left( -\frac{\ell}{\lambda} \right) \bmod 1 = 1 - \frac{\ell}{\lambda}.$$

and the constant wavelength is

$$(A.4) \quad \lambda = \frac{\ell}{1 - \phi^*}.$$

For the neuromechanical model,  $\ell = L/6$ , so the wavelength (normalized by bodylength) is

$$(A.5) \quad \frac{\lambda}{L} = \frac{1}{6(1 - \phi^*)}.$$

**A.1.2. Nonconstant Wavespeed.** The non-uniform phase differences  $\phi_k = \theta_{k+1} - \theta_k$  ( $k = 1, \dots, 5$ ) between modules are used to define an effective wavelength of undulation when the wavespeed is nonconstant. The distance between the center of the first and center of the sixth module is  $5/6L$ , and the phase difference between them is  $\sum_{k=1}^5 (1 - \phi_k)$ . This gives an effective

wavelength (normalized by 5/6 bodylengths)

$$(A.6) \quad \frac{\lambda}{(5/6)L} = \frac{1}{\sum_{k=1}^5 (1 - \phi_k)},$$

so the wavelength (normalized by bodylength) is

$$(A.7) \quad \frac{\lambda}{L} = \frac{1}{6 \sum_{k=1}^5 (1 - \phi_k)/5}.$$

Note that this is equivalent to the constant phase difference wavelength (equation A.5) using the *average phase difference* between the modules as the constant phase difference  $\phi^*$ , i.e., with

$$(A.8) \quad 1 - \phi^* = \frac{\sum_{k=1}^5 (1 - \phi_k)}{5}.$$

For the neuromechanical model results, first the phase differences  $\phi_k$  between the modules were computed, then the wavelength was computed according to equation A.7 above.

**A.1.3.  $N$ -Module Wavelength.** With  $N$  modules of fixed length  $\ell = L/6$ , the non-uniform phase differences  $\phi_k = \theta_{k+1} - \theta_k$  ( $k = 1, \dots, 5$ ) between modules are used to define an effective wavelength of undulation. The distance between the center of the first and center of the sixth module is  $(N - 1)\ell$ , and the phase difference between them is  $\sum_{k=1}^{N-1} (1 - \phi_k)$ . This gives an effective wavelength (normalized by  $(N - 1)\ell$  bodylengths)

$$(A.9) \quad \frac{\lambda}{(N - 1)\ell} = \frac{1}{\sum_{k=1}^{N-1} (1 - \phi_k)},$$

so the wavelength  $\lambda$  is

$$(A.10) \quad \lambda = \frac{(N - 1)\ell}{\sum_{k=1}^{N-1} (1 - \phi_k)},$$

which normalized by bodylength  $L = 6\ell$  is

$$(A.11) \quad \frac{\lambda}{L} = \frac{1}{6 \sum_{k=1}^{N-1} (1 - \phi_k)/(N - 1)}.$$

## A.2. Derivation of Mechanical Parameters

First, the bending modulus  $k_b = EI_c$  of the cuticle of the worm was determined, where  $E$  is the Young's modulus and  $I_c$  is the second moment of area of the cuticle. The nematode body can

be thought of as a pressurized, fluid-filled tube or modeled as an annular cylinder as in Cohen and Ranner [9], so the only elasticity in the body is that of the cuticle. To approximate the second moment of area of the cuticle,  $I_c$ , note that the cuticle width  $r_{\text{cuticle}} = 0.5 \mu\text{m}$  is much smaller than the average worm radius  $R = 40 \mu\text{m}$ . Following Cohen and Ranner [9],

$$(A.12) \quad I_c = 2\pi R^3 r_{\text{cuticle}} = 2.0 \times 10^{-7} \text{mm}^4.$$

The Young's modulus  $E$  has been estimated to be as small as  $E = 3.77 \pm 0.62 \text{ kPa}$  [49] or as large as  $E = 13 \text{ MPa}$  [15]. Backholm et al. [2] gives a range of  $110 \pm 30 \text{ kPa} \leq E \leq 1.3 \pm 0.3 \text{ MPa}$ . Using these estimates, we explore the range of bending moduli  $k_b = EI_c = 7.53 \times 10^{-10} - 2.6 \times 10^{-6} \text{ N}(\text{mm})^2$ .

The *cuticle* viscosity has been estimated as  $5 \times 10^{-16} \text{ Nm}^2\text{s}$  [15]. The internal *tissue* viscosity has been estimated to be constant and negative (energy-generating) as  $c_d = -177.1 \pm 15.2 \text{ Pa s}$  so that  $\mu_b = c_d I = -1.7 \times 10^{-11} \text{ N}(\text{mm})^2\text{s}$  [49] by a model fit, however this includes the active muscle components. Backholm et al. [2] estimated the range  $c_d \in [1 \times 10^2, 1 \times 10^4] \text{ Pa s}$ , so that the effective viscosity is  $c_d I \in [2 \times 10^{-11}, 2 \times 10^{-9}] \text{ N}(\text{mm})^2\text{s}$ . These experiments used different techniques and models for viscosity, so likely have different effects lumped into the viscosity parameter. In order to explore the range of effective body mechanics timescales  $\tau_f = \mu_b/k_b = 0.001 - 5 \text{ s}$ , we use the range of body viscosities  $\mu_b = 5 \times 10^{-10} - 1.3 \times 10^{-7} \text{ N}(\text{mm})^2\text{s}$  in our model.

Following previous modeling procedures [9, 15], the normal drag coefficient  $C_N$  of a slender body with length  $L = 1 \text{ mm}$  and (average) radius  $R = 40 \mu\text{m}$  in a solution with viscosity  $\mu_f$  is

$$(A.13) \quad C_N = \frac{4\pi\mu_f}{\ln(L/R) + 0.5} = \alpha\mu_f \approx 3.4\mu_f.$$

## APPENDIX B

### Theory of Weakly Coupled Oscillators

Here, we describe how the theory of weakly coupled oscillators [44] can reduce the 30-dimensional neuromechanical model down to a 6-dimensional phase model. Recall that the neuromechanical model can be written as a network of coupled oscillator modules:

$$(B.1) \quad \frac{d\mathbf{X}_j}{dt} = S(\mathbf{X}_j(t)) + C_j(\mathbf{X}_1(t), \dots, \mathbf{X}_6(t)), \quad j = 1, \dots, 6$$

where  $S(\mathbf{X}_j(t))$  describes the intrinsic uncoupled oscillator dynamics (equations 3.1-3.5) and  $C_j(\mathbf{X}_1(t), \dots, \mathbf{X}_6(t))$  describes the coupling input from all the modules to the  $j^{\text{th}}$  module through gap-junctions, nonlocal proprioception, and body mechanics (equation 3.11).

#### B.1. Phase and Inverse Phase Map

When uncoupled, each neuromechanical module oscillates with a stable period  $T$ . The neuromechanical oscillation corresponds to a stable  $T$ -periodic limit cycle  $\mathbf{X}^{LC}(t)$  in  $(\kappa, A_V, A_D, V_V, V_D)$ -state-space. This limit cycle can be parametrized by phase

$$(B.2) \quad \theta = (\omega t + \theta^0) \bmod 1$$

with the initial phase  $\theta^0 \in [0, 1)$ . As  $\theta$  increases at a constant rate  $\omega = 1/T$ ,  $\mathbf{X}^{LC}(\theta)$  traces out the limit cycle through state-space and the state of the oscillator on the limit cycle is given by

$$(B.3) \quad \mathbf{X}(t) = \mathbf{X}^{LC}(\theta).$$

Each point on the limit cycle  $\mathbf{X} = \mathbf{X}^{LC}(\theta)$  corresponds to a unique phase  $\theta$ , so there is an inverse map

$$(B.4) \quad \theta = (\mathbf{X}^{LC})^{-1}(\mathbf{X}) = \Phi(\mathbf{X}).$$

The time-evolution of phase is then given by the time-derivative of equation B.4, which is equal to  $\omega$  by the definition of phase (equation B.2):

$$(B.5) \quad \frac{d\theta}{dt} = \nabla_{\underline{\mathbf{X}}}\Phi(\underline{\mathbf{X}}^{LC}(t)) \cdot \frac{d\underline{\mathbf{X}}^{LC}}{dt} = \omega,$$

where  $\nabla_{\underline{\mathbf{X}}}\Phi$  is the gradient of  $\Phi(\underline{\mathbf{X}})$  evaluated at the point on the limit cycle  $\underline{\mathbf{X}}$ :

$$(B.6) \quad \nabla_{\underline{\mathbf{X}}}\Phi(\underline{\mathbf{X}}) = \left[ \left( \frac{d\Phi}{d\kappa}, \frac{d\Phi}{dA_V}, \frac{d\Phi}{dA_D}, \frac{d\Phi}{dV_V}, \frac{d\Phi}{dV_D} \right) \Big|_X \right]^T.$$

Since the gradient of the phase map can describe how the phase  $\Phi$  shifts in response to perturbations in any direction, it is also called the phase response curve/function (PRC)  $\underline{\mathbf{Z}}(t)$ . The phase response functions for perturbations to each system state variable,  $Z_{\kappa}(t), Z_{A_V}(t), Z_{A_D}(t), Z_{V_V}(t), Z_{V_D}(t)$ , are the vector-wise components of the gradient of the phase map  $\nabla_{\underline{\mathbf{X}}}\Phi$ . Thus we use the gradient along the limit cycle  $\nabla_{\underline{\mathbf{X}}}\Phi(\underline{\mathbf{X}}^{LC})$  and the periodic phase response function  $\underline{\mathbf{Z}}(t)$  interchangeably.

**B.1.1. Asymptotic Phase.** For points  $\underline{\mathbf{X}}$  on the limit cycle there is a unique phase  $\theta$ , and vice-versa. The solution  $\underline{\mathbf{Y}}(t)$  to the module equations, with initial condition  $\underline{\mathbf{Y}}_0$  off but close to the limit cycle (denoted  $\underline{\mathbf{Y}}(t; \underline{\mathbf{Y}}_0)$ ), will asymptotically approach the limit cycle and converge to a solution  $\underline{\mathbf{X}}(t; \underline{\mathbf{X}}_0)$  for some unique initial condition  $\underline{\mathbf{X}}_0$  on the limit cycle. We define the *asymptotic phase* of a point  $\underline{\mathbf{Y}}_0$  off the limit cycle to be the phase  $\theta = \Phi(\underline{\mathbf{X}}_0)$ , i.e.,  $\Phi(\underline{\mathbf{Y}}_0) = \Phi(\underline{\mathbf{X}}_0)$  if and only if

$$(B.7) \quad \|\underline{\mathbf{X}}(t; \underline{\mathbf{X}}_0) - \underline{\mathbf{Y}}(t; \underline{\mathbf{Y}}_0)\| \rightarrow 0 \text{ as } t \rightarrow \infty.$$

## B.2. Weakly Coupled Oscillators

Combining the differential equations for the fully coupled neuromechanical model (equation B.1) and the phase of a single module (equation B.5), the phase of the  $j^{th}$  oscillator module in the fully coupled neuromechanical model is governed by

$$(B.8) \quad \begin{aligned} \frac{d\theta_j}{dt} &= \nabla_{\underline{\mathbf{X}}}\Phi(\underline{\mathbf{X}}_j(t)) \cdot \frac{d\underline{\mathbf{X}}_j}{dt} \\ &= \nabla_{\underline{\mathbf{X}}}\Phi(\underline{\mathbf{X}}_j(t)) \cdot [S(\underline{\mathbf{X}}_j(t)) + C_j(\underline{\mathbf{X}}_1(t), \dots, \underline{\mathbf{X}}_6(t))] \end{aligned}$$

When the coupling input  $C_j(\underline{\mathbf{X}}_1(t), \dots, \underline{\mathbf{X}}_6(t))$  is weak, the module's intrinsic dynamics  $S(\underline{\mathbf{X}}_j)(t)$  dominate the dynamics of the fully-coupled system, and the modules remain on their intrinsic limit cycle, i.e.,  $X_j(t) \approx X^{LC}(t + \theta_j(t))$ . That is, we assume that the coupling only affects the phase of the oscillators but not the amplitude of the limit cycles. With this assumption, the phase equations are

$$(B.9) \quad \begin{aligned} \frac{d\theta_j}{dt} &= \nabla_{\underline{\mathbf{X}}} \Phi(\underline{\mathbf{X}}^{LC}(t + \theta_j(t))) \cdot [S(\underline{\mathbf{X}}^{LC}(t + \theta_j(t))) + C_j(\underline{\mathbf{X}}_1(t + \theta_1(t)), \dots, \underline{\mathbf{X}}_6(t + \theta_6(t)))] \\ &= \omega_j + \nabla_{\underline{\mathbf{X}}} \Phi(\underline{\mathbf{X}}^{LC}(t + \theta_j(t))) \cdot C_j(\underline{\mathbf{X}}_1(t + \theta_1(t)), \dots, \underline{\mathbf{X}}_6(t + \theta_6(t))). \end{aligned}$$

Under the weak coupling assumption, the modules respond linearly to the coupling inputs, so the small phase shifts in response to coupling inputs at different timings sum linearly. We can assume that the phase shifts due to coupling dynamics are negligible over a single period and that they only add up over many periods, that is the changes in phase  $\theta_j$  occur on a much slower timescale than the period  $T$ . Thus the explicit time dependence in equation B.9 can be removed by averaging the rate of change of  $\theta_j$  over a single period  $T$  and holding  $\theta_1, \dots, \theta_6$  constant inside the integral:

$$(B.10) \quad \frac{d\theta_j}{dt} = \omega_j + \frac{1}{T} \int_0^T \underline{\mathbf{Z}}(\tilde{t} + \theta_j) \cdot C_j(\underline{\mathbf{X}}^{LC}(\tilde{t} + \theta_1), \dots, \underline{\mathbf{X}}^{LC}(\tilde{t} + \theta_6)) d\tilde{t}.$$

This averaging process assumes that the phases  $\theta_j$  are constant with respect to the fast-time  $\tilde{t}$ , but they vary in the slow-time  $t$  (for the rigorous averaging theory see [14, 21]). Shifting the integrand by  $\theta_j$ ,

$$(B.11) \quad \frac{d\theta_j}{dt} = \omega_j + \frac{1}{T} \int_0^T \underline{\mathbf{Z}}(\tilde{t}) \cdot C_j(\underline{\mathbf{X}}^{LC}(\tilde{t} + \theta_1 - \theta_j), \dots, \underline{\mathbf{X}}^{LC}(\tilde{t} + \theta_6 - \theta_j)) d\tilde{t}.$$

Applying the description of the coupling inputs (equation 3.11), taking the dot product inside the integral, and separating terms,

$$\begin{aligned}
\text{(B.12)} \quad \frac{d\theta_j}{dt} = & \omega_j + \sum_{k=1}^6 \varepsilon_m (D_4^{-1})_{jk} \frac{1}{T} \int_0^T Z_\kappa(\tilde{t}) (-\dot{\kappa}^{LC}(\tilde{t} + \theta_k - \theta_j)) d\tilde{t} \\
& + \sum_{k=1}^6 \frac{\varepsilon_p}{\tau_n} (W_p)_{jk} \frac{1}{T} \int_0^T Z_{V_V}(\tilde{t}) \kappa^{LC}(\tilde{t} + \theta_k - \theta_j) d\tilde{t} \\
& + \sum_{k=1}^6 \frac{\varepsilon_p}{\tau_n} (W_p)_{jk} \frac{1}{T} \int_0^T Z_{V_D}(\tilde{t}) (-\kappa^{LC}(\tilde{t} + \theta_k - \theta_j)) d\tilde{t} \\
& + \sum_{k=1}^6 \frac{\varepsilon_g}{\tau_n} (W_g)_{jk} \frac{1}{T} \int_0^T Z_{V_V}(\tilde{t}) (V_V^{LC}(\tilde{t} + \theta_k - \theta_j) - V_V^{LC}(\tilde{t})) d\tilde{t} \\
& + \sum_{k=1}^6 \frac{\varepsilon_g}{\tau_n} (W_g)_{jk} \frac{1}{T} \int_0^T Z_{V_D}(\tilde{t}) (V_D^{LC}(\tilde{t} + \theta_k - \theta_j) - V_D^{LC}(\tilde{t})) d\tilde{t}.
\end{aligned}$$

This is equivalent to the phase model

$$\text{(B.13)} \quad \dot{\theta}_j = \omega_j + \sum_{k=1}^6 \varepsilon_m (D_4^{-1})_{jk} H_m(\theta_k - \theta_j) + \varepsilon_g (W_g)_{jk} H_g(\theta_k - \theta_j) + \varepsilon_p (W_p)_{jk} H_p(\theta_k - \theta_j),$$

with interaction functions  $H(\phi)$  :

$$\text{(B.14)} \quad H_m(\phi) = -\frac{1}{T} \int_0^T Z_\kappa(t) \dot{\kappa}^{LC}(t - \phi) dt,$$

$$\text{(B.15)} \quad H_p(\phi) = \frac{1}{\tau_n} \frac{1}{T} \int_0^T Z_{V_V}(t) \kappa^{LC}(t - \phi) - Z_{V_D}(t) \kappa^{LC}(t - \phi) dt,$$

$$\text{(B.16)} \quad H_g(\phi) = \frac{1}{\tau_n} \frac{1}{T} \int_0^T Z_{V_V}(t) (\underline{\mathbf{V}}_V^{LC}(t - \phi) - \underline{\mathbf{V}}_V^{LC}(t)) + Z_{V_D}(t) (\underline{\mathbf{V}}_D^{LC}(t - \phi) - \underline{\mathbf{V}}_D^{LC}(t)) dt.$$

### B.3. Computing the Phase Response Curves

Here, we show how to compute the periodic phase response curve (PRC) function  $\underline{\mathbf{Z}}(t)$ , i.e., the gradient of the phase map along the limit cycle  $\nabla_{\underline{\mathbf{X}}} \Phi(\underline{\mathbf{X}}^{LC}(t))$ . Consider two solutions to the isolated neuromechanical oscillator module equations,  $\underline{\mathbf{X}}(t) = \underline{\mathbf{X}}^{LC}(t + \theta)$  that starts at  $\underline{\mathbf{X}}_0 =$

$\underline{\mathbf{X}}^{LC}(\theta)$  and  $\underline{\mathbf{Y}}(t) = \underline{\mathbf{X}}^{LC}(t + \theta) + \underline{\mathbf{p}}(t)$  that starts at  $\underline{\mathbf{Y}}(0) = \underline{\mathbf{X}}^{LC}(\theta) + \underline{\mathbf{p}}(0)$ , where  $\underline{\mathbf{p}}(0)$  is a small perturbation. Linearizing around the stable limit cycle, the perturbation  $p(t)$  satisfies

$$(B.17) \quad \frac{dp}{dt} = DF(\underline{\mathbf{X}}^{LC}(t + \theta))p,$$

where  $DF(\underline{\mathbf{X}}^{LC}(t))$  is the Jacobian of  $S(\underline{\mathbf{X}})$ , the isolated oscillator dynamics, evaluated along the limit cycle  $\underline{\mathbf{X}}^{LC}(t)$ . The phase difference between the two solutions  $\underline{\mathbf{X}}(t), \underline{\mathbf{Y}}(t)$  is

$$(B.18) \quad \Delta\theta = \Phi(\underline{\mathbf{X}}^{LC}(t + \theta) + p(t)) - \Phi(\underline{\mathbf{X}}^{LC}(t + \theta)) = \nabla_{\underline{\mathbf{X}}}\Phi(\underline{\mathbf{X}}^{LC}(t + \theta)) \cdot p(t) + \mathcal{O}(|p^2|)$$

Because the oscillator modules are isolated, the phase difference between the two solutions,  $\Delta\theta$ , is constant, so by differentiating equation B.18 with respect to time,

$$(B.19) \quad \begin{aligned} 0 &= \frac{d}{dt} [\nabla_{\underline{\mathbf{X}}}\Phi(\underline{\mathbf{X}}^{LC}(t + \theta)) \cdot p(t)] \\ &= \frac{d}{dt} [\nabla_{\underline{\mathbf{X}}}\Phi(\underline{\mathbf{X}}^{LC}(t + \theta))] \cdot p(t) + \nabla_{\underline{\mathbf{X}}}\Phi(\underline{\mathbf{X}}^{LC}(t + \theta)) \cdot \frac{dp}{dt} \\ &= \frac{d}{dt} [\nabla_{\underline{\mathbf{X}}}\Phi(\underline{\mathbf{X}}^{LC}(t + \theta))] \cdot p(t) + \nabla_{\underline{\mathbf{X}}}\Phi(\underline{\mathbf{X}}^{LC}(t + \theta)) \cdot (DF(\underline{\mathbf{X}}^{LC}(t + \theta))p(t)) \\ &= \left[ \frac{d}{dt} (\nabla_{\underline{\mathbf{X}}}\Phi(\underline{\mathbf{X}}^{LC}(t + \theta))) + DF(\underline{\mathbf{X}}^{LC}(t + \theta))^T \nabla_{\underline{\mathbf{X}}}\Phi(\underline{\mathbf{X}}^{LC}(t + \theta)) \right] \cdot p(t) \end{aligned}$$

Since the perturbation  $p(t)$  is arbitrary,

$$(B.20) \quad \frac{d}{dt} (\nabla_{\underline{\mathbf{X}}}\Phi(\underline{\mathbf{X}}^{LC}(t + \theta))) + DF(\underline{\mathbf{X}}^{LC}(t + \theta))^T \nabla_{\underline{\mathbf{X}}}\Phi(\underline{\mathbf{X}}^{LC}(t + \theta)) = 0,$$

i.e.,  $\nabla_{\underline{\mathbf{X}}}\Phi(\underline{\mathbf{X}}^{LC}(t))$  solves the ‘‘adjoint equation’’

$$(B.21) \quad \frac{d\underline{\mathbf{Z}}}{dt} = -DF(\underline{\mathbf{X}}^{LC}(t))\underline{\mathbf{Z}}.$$

The definition of the phase map provides a normalization condition:

$$(B.22) \quad \frac{d\theta}{dt} = \nabla_{\underline{\mathbf{X}}}\Phi(\underline{\mathbf{X}}^{LC}(t)) \cdot \frac{d\underline{\mathbf{X}}^{LC}}{dt} = \underline{\mathbf{Z}}(t) \cdot S(\underline{\mathbf{X}}^{LC}(t)) = \omega.$$

The adjoint system (equation B.21) has an unstable  $T$ -periodic limit cycle because it has the opposite stability of the original system, an asymptotically stable  $T$ -periodic limit cycle. Thus the

T-periodic solution to equation B.21, i.e., the PRC  $\underline{\mathbf{Z}}(t)$ , can be found by integrating backwards in time from an arbitrary initial condition. We then normalize the PRC using equation B.22.

#### B.4. Computing the Interaction Functions Quickly Using the Fourier Transform

We can compute the interaction functions quickly using the Fourier transform to turn the convolution-like integral into a product of vector functions. Given periodic functions  $Z(t)$  (a PRC component) and  $I(t)$  (a coupling input), the interaction function  $H(\phi)$  is

$$(B.23) \quad H(\phi) = \frac{1}{T} \int_0^T Z(t)I(t + \phi)dt.$$

If we let  $\tilde{Z}(-t) = Z(t)$ , then

$$(B.24) \quad H(\phi) = \frac{1}{T} \int_0^T \tilde{Z}(-t)I(\phi - (-t))dt.$$

With the change of variables  $\tau = -t$ ,  $d\tau = -dt$  and

$$(B.25) \quad H(\phi) = -\frac{1}{T} \int_0^T \tilde{Z}(\tau)I(\phi - \tau)d\tau,$$

which is now a convolution integral. Applying the Fourier transform turns the convolution into a product:

$$(B.26) \quad H(\phi) = -\frac{1}{T} \mathcal{F}^{-1}\{\mathcal{F}\{\tilde{Z}\}(\xi) \cdot \mathcal{F}\{I\}(\xi)\}(\phi).$$

Note that

$$(B.27) \quad \begin{aligned} \mathcal{F}\{\tilde{Z}\}(\xi) &= \int_{-\infty}^{\infty} \tilde{Z}(t)e^{-i\xi t} dt \\ &= \int_{-\infty}^{\infty} Z(-t)e^{-i(-\xi)(-t)} dt \\ &= -\int_{-\infty}^{\infty} Z(\tau)e^{-i(-\xi)\tau} dt \\ &= -\mathcal{F}\{Z\}(-\xi), \end{aligned}$$

so

$$(B.28) \quad H(\phi) = -\frac{1}{T} \mathcal{F}^{-1} \{ -\mathcal{F}\{Z\}(-\xi) \cdot \mathcal{F}\{I\}(\xi) \}(\phi).$$

This can be computed quickly and efficiently using the Fast Fourier Transform (fft) and the Inverse Fast Fourier Transform (ifft) on vectorized samples of the periodic functions  $Z(t)$ ,  $I(t)$  by the command `(-1/T)*ifft(-fft(flip(Z)).*fft(I))` in MATLAB.

## APPENDIX C

### Deriving the 1-D Poincaré Map

#### C.1. Steady-State Analysis

When  $S_V$  and  $S_D$  are *fixed* and  $S_D - S_V = 0$ , i.e., when the two neurons are both on or both off, we can assess the steady state behavior of the reduced neuromechanical module (equation 5.18). By assuming  $K(t) = a \exp(\lambda t)$ , the 2nd order ODE becomes

$$(C.1) \quad (\tau\lambda^2 + (1 + \tau)\lambda + 1)a \exp(\lambda t) = 0$$

and thus

$$(C.2) \quad \begin{aligned} \lambda &= \frac{1}{2\tau} \left( -1 - \tau \pm \sqrt{(1 + \tau)^2 - 4\tau} \right) \\ &= \frac{1}{2\tau} \left( -1 - \tau \pm \sqrt{1 - 2\tau + \tau^2} \right) \\ &= \frac{1}{2\tau} (-1 - \tau \pm (1 - \tau)) \\ &= -1, -1/\tau. \end{aligned}$$

Hence, without any dynamics in  $S_D, S_V$ , the steady state at  $K = 0, M = 0$  is globally asymptotically stable for any  $\tau$ . If the system starts with  $S_D - S_V = 0$  and input to the B-class neurons in between the on/off thresholds, i.e., the initial  $K$  is in  $\left( \frac{-1 - \epsilon}{2} - I, \frac{1 + \epsilon}{2} - I \right)$ , then neither neuron will switch on/off and so  $K \rightarrow 0, M \rightarrow 0$  according to the above solution.

When  $S_V$  and  $S_D$  are *fixed* and either  $S_D - S_V = 1$  or  $S_D - S_V = -1$ , the solutions are similar. Generically, the solution to equation 5.11 for fixed  $S_V, S_D$  is given by

$$(C.3) \quad K(t) = Ae^{-t} + Be^{-t/\tau} + c(S_D - S_V),$$

and the equilibrium  $K = c(S_D - S_V), M = 0$  is always globally asymptotically stable.

## C.2. Map Derivation

Here, we piece together the solutions to the reduced oscillator model (equations 5.18-5.20) through each proprioceptive threshold to generate a Poincaré map from initial condition  $K = K_{off}^V, M = \alpha_0, S_D = 1, S_V = 0$  to the next intersection with this proprioceptive threshold  $K = K_{off}^V$  from the right, i.e., to  $K = K_{off}^V, M = \alpha_2 < 0, S_D = 1, S_V = 0$ . Essentially, we map  $M = \alpha_0$  to  $M = \alpha_2$  after a full neuromechanical loop. This 1-D map is given by

$$(C.4) \quad \alpha_2 = F(\alpha_0) = -F_2(F_1(-F_2(F_1(\alpha_0)))),$$

and is generated by intermediate maps along each solution branch

$$(C.5) \quad \alpha_{1/2} = F_1(\alpha_0),$$

$$(C.6) \quad \alpha_1 = F_2(\alpha_{1/2}),$$

$$(C.7) \quad \alpha_{3/2} = -F_1(-\alpha_1),$$

$$(C.8) \quad \alpha_2 = -F_2(-\alpha_{3/2}),$$

which we define in the following subsections. Note that depending on parameters, these maps may not be defined, which indicates that the system instead converges to a stable equilibrium along one of the solution branches, breaking the neuromechanical loop. Conditions for the existence of these maps and details on how to numerically solve for the roots of these maps are given in the next section.

**C.2.1. Map 1 -  $(K_{off}^V, \alpha_0)$  to  $(K_{on}^V, \alpha_{1/2})$ .** Map 1 flows the solution forward in time from the first proprioceptive threshold at  $K_{off}^V$  to the second threshold at  $K_{on}^V$  to map  $M = \alpha_0$  to  $M = \alpha_{1/2}$ . Using the general solution (equation C.3) with the initial condition  $K = K_{off}^V, M = \alpha_0, S_D = 1, S_V = 0$ , and equilibrium  $c(S_D - S_V) = c$ , we obtain the coefficients

$$(C.9) \quad B = \frac{K_{off}^V + \alpha_0 - c}{1 - 1/\tau},$$

$$(C.10) \quad A = K_{off}^V - c - B.$$

Next, we solve for the proprioceptive-threshold crossing time, i.e., the time  $t_{1/2}$  such that

$$(C.11) \quad K(t_{1/2}) = K_{on}^V, \quad M(t_{1/2}) = \alpha_{1/2}.$$

With the general solution (equation C.3) and coefficients (equations C.9-C.10), we sum together  $K(t_{1/2})$  and  $M(t_{1/2})$  to obtain an equation for the crossing time  $t_{1/2}$ :

$$\begin{aligned} c + Ae^{-t_{1/2}} + Be^{-t_{1/2}/\tau} &= K_{on}^V \\ +) \quad -Ae^{-t_{1/2}} - \frac{B}{\tau}e^{-t_{1/2}/\tau} &= \alpha_{1/2} \\ \hline c + B(1 - 1/\tau)e^{-t_{1/2}/\tau} &= K_{on}^V + \alpha_{1/2} \\ (K_{off}^V - c + \alpha_0)e^{-t_{1/2}/\tau} &= K_{on}^V - c + \alpha_{1/2} \\ (C.12) \quad t_{1/2} &= -\tau \ln \left( \frac{K_{on}^V - c + \alpha_{1/2}}{K_{off}^V - c + \alpha_0} \right). \end{aligned}$$

Finally, we use equation C.12 to derive an implicit equation for  $\alpha_{1/2}$ :

$$\begin{aligned} \frac{c}{\tau} + \frac{A}{\tau}e^{-t_{1/2}} + \frac{B}{\tau}e^{-t_{1/2}/\tau} &= \frac{K_{on}^V}{\tau} \\ +) \quad -Ae^{-t_{1/2}} - \frac{B}{\tau}e^{-t_{1/2}/\tau} &= \alpha_{1/2} \\ \hline \frac{c}{\tau} + A(1/\tau - 1)e^{-t_{1/2}} &= \frac{K_{on}^V}{\tau} + \alpha_{1/2} \\ c + A(-\tau)(1 - 1/\tau) \left[ \frac{K_{on}^V - c + \alpha_{1/2}}{K_{off}^V - c + \alpha_0} \right]^\tau &= K_{on}^V + \alpha_{1/2}\tau \\ c - [(K_{off}^V - c)(1 - 1/\tau) - (K_{off}^V - c + \alpha_0)]\tau \left[ \frac{K_{on}^V - c + \alpha_{1/2}}{K_{off}^V - c + \alpha_0} \right]^\tau &= K_{on}^V + \alpha_{1/2}\tau \\ (K_{off}^V - c + \alpha_0\tau) \left[ \frac{K_{on}^V - c + \alpha_{1/2}}{K_{off}^V - c + \alpha_0} \right]^\tau &= K_{on}^V - c + \alpha_{1/2}\tau \\ (C.13) \quad \left[ \frac{K_{on}^V - c + \alpha_{1/2}}{K_{off}^V - c + \alpha_0} \right]^\tau &= \frac{K_{on}^V - c + \alpha_{1/2}\tau}{K_{off}^V - c + \alpha_0\tau} \end{aligned}$$

Finding the root  $\alpha_{1/2}$  of equation C.13 for a given  $\alpha_0$  defines the map from  $\alpha_0$  to  $\alpha_{1/2}$ , i.e.,  $\alpha_{1/2} = F_1(\alpha_0)$ . Note that depending on parameters, equation C.13 may not have a root  $\alpha_{1/2}$ , which indicates that the system instead converges to the stable equilibrium  $K = c, M = 0$ .

**C.2.2. Map 2 -  $(K_{on}^V, \alpha_{1/2})$  to  $(K_{off}^D, \alpha_1)$ .** Map 2 flows the solution forward in time from the second proprioceptive threshold at  $K_{on}^V$  to the third threshold at  $K_{off}^D$  to map  $M = \alpha_{1/2}$  to  $M = \alpha_1$ . Using the general solution (equation C.3) with the initial condition  $K = K_{on}^V, M = \alpha_{1/2}, S_D = 1, S_V = 1$ , and equilibrium  $c(S_D - S_V) = 0$ , we obtain the coefficients

$$(C.14) \quad B = \frac{K_{on}^V + \alpha_{1/2}}{1 - 1/\tau},$$

$$(C.15) \quad A = K_{on}^V - B.$$

Next, we solve for the proprioceptive-threshold crossing time, i.e., the time  $t_1$  such that

$$(C.16) \quad K(t_1) = K_{off}^D, \quad M(t_1) = \alpha_1.$$

With the general solution (equation C.3) and coefficients (equations C.14-C.15), we sum together  $K(t_1)$  and  $M(t_1)$  to obtain an equation for the crossing time  $t_1$ :

$$\begin{aligned} & Ae^{-t_1} + Be^{-t_1/\tau} = K_{off}^D \\ +) & -Ae^{-t_1} - \frac{B}{\tau}e^{-t_1/\tau} = \alpha_1 \\ \hline & B(1 - 1/\tau)e^{-t_1/\tau} = K_{off}^D + \alpha_1 \\ & (K_{on}^V + \alpha_{1/2})e^{-t_1/\tau} = K_{off}^D + \alpha_1 \\ (C.17) \quad & t_1 = -\tau \ln \left( \frac{K_{off}^D + \alpha_1}{K_{on}^V + \alpha_{1/2}} \right). \end{aligned}$$

Finally, we use equation C.17 to derive an implicit equation for  $\alpha_1$ :

$$\frac{A}{\tau}e^{-t_1} + \frac{B}{\tau}e^{-t_1/\tau} = \frac{K_{off}^D}{\tau}$$

$$+) \quad -Ae^{-t_1} - \frac{B}{\tau}e^{-t_1/\tau} = \alpha_1$$

---


$$A(1/\tau - 1)e^{-t_1} = \frac{K_{off}^D}{\tau} + \alpha_1$$

$$A(-\tau)(1 - 1/\tau) \left[ \frac{K_{off}^D + \alpha_1}{K_{on}^V + \alpha_{1/2}} \right]^\tau = K_{off}^D + \alpha_1\tau$$

$$-[(K_{on}^V)(1 - 1/\tau) - (K_{on}^V + \alpha_{1/2})]\tau \left[ \frac{K_{off}^D + \alpha_1}{K_{on}^V + \alpha_{1/2}} \right]^\tau = K_{off}^D + \alpha_1\tau$$

$$(K_{on}^V + \alpha_{1/2}\tau) \left[ \frac{K_{off}^D + \alpha_1}{K_{on}^V + \alpha_{1/2}} \right]^\tau = K_{off}^D + \alpha_1\tau$$

$$(C.18) \quad \left[ \frac{K_{off}^D + \alpha_1}{K_{on}^V + \alpha_{1/2}} \right]^\tau = \frac{K_{off}^D + \alpha_1\tau}{K_{on}^V + \alpha_{1/2}\tau}$$

Finding the root  $\alpha_1$  of equation C.18 for a given  $\alpha_{1/2}$  defines the map from  $\alpha_{1/2}$  to  $\alpha_1$ , i.e.,  $\alpha_1 = F_2(\alpha_{1/2})$ . Note that depending on parameters, equation C.18 may not have a root  $\alpha_1$ , which indicates that the system instead converges to the stable equilibrium  $K = 0, M = 0$ .

**C.2.3. Map 3 -  $(K_{off}^D, \alpha_1)$  to  $(K_{on}^D, \alpha_{3/2})$ .** Map 3 flows the solution forward in time from the third proprioceptive threshold at  $K_{off}^D$  to the fourth threshold at  $K_{on}^D$  to map  $M = \alpha_1$  to  $M = \alpha_{3/2}$ . Using the general solution (equation C.3) with the initial condition  $K = K_{off}^D, M = \alpha_1, S_D = 0, S_V = 1$ , and equilibrium  $c(S_D - S_V) = -c$ , we obtain the coefficients

$$(C.19) \quad B = \frac{K_{off}^D + \alpha_1 + c}{1 - 1/\tau},$$

$$(C.20) \quad A = K_{off}^D + c - B.$$

Next, we solve for the proprioceptive-threshold crossing time, i.e., the time  $t_{3/2}$  such that

$$(C.21) \quad K(t_{3/2}) = K_{on}^D, \quad \dot{K}(t_{3/2}) = \alpha_{3/2}.$$

With the general solution (equation C.3) and coefficients (equations C.19-C.20), we sum together  $K(t_{3/2})$  and  $M(t_{3/2})$  to obtain an equation for the crossing time  $t_{3/2}$ :

$$\begin{aligned}
& -c + Ae^{-t_{3/2}} + Be^{-t_{3/2}/\tau} = K_{on}^D \\
+) & -Ae^{-t_{3/2}} - \frac{B}{\tau}e^{-t_{3/2}/\tau} = \alpha_{3/2} \\
\hline
& -c + B(1 - 1/\tau)e^{-t_{3/2}/\tau} = K_{on}^D + \alpha_{3/2} \\
& (K_{off}^D + c + \alpha_1)e^{-t_{3/2}/\tau} = K_{on}^D + c + \alpha_{3/2} \\
(C.22) \quad & t_{3/2} = -\tau \ln \left( \frac{K_{on}^D + c + \alpha_{3/2}}{K_{off}^D + c + \alpha_1} \right).
\end{aligned}$$

Finally, we use equation C.22 to derive an implicit equation for  $\alpha_{3/2}$ :

$$\begin{aligned}
& \frac{-c}{\tau} + \frac{A}{\tau}e^{-t_{3/2}} + \frac{B}{\tau}e^{-t_{3/2}/\tau} = \frac{K_{on}^D}{\tau} \\
+) & -Ae^{-t_{3/2}} - \frac{B}{\tau}e^{-t_{3/2}/\tau} = \alpha_{3/2} \\
\hline
& \frac{-c}{\tau} + A(1/\tau - 1)e^{-t_{3/2}} = \frac{K_{on}^D}{\tau} + \alpha_{3/2} \\
& c + A(-\tau)(1 - 1/\tau) \left[ \frac{K_{on}^D + c + \alpha_{3/2}}{K_{off}^D + c + \alpha_1} \right]^\tau = K_{on}^D + \alpha_{3/2}\tau \\
& c - [(K_{off}^D + c)(1 - 1/\tau) - (K_{off}^D + c + \alpha_1)]\tau \left[ \frac{K_{on}^D + c + \alpha_{3/2}}{K_{off}^D + c + \alpha_1} \right]^\tau = K_{on}^D + \alpha_{3/2}\tau \\
& (K_{off}^D + c + \alpha_1\tau) \left[ \frac{K_{on}^D + c + \alpha_{3/2}}{K_{off}^D + c + \alpha_1} \right]^\tau = K_{on}^D + c + \alpha_{3/2}\tau \\
(C.23) \quad & \left[ \frac{K_{on}^D + c + \alpha_{3/2}}{K_{off}^D + c + \alpha_1} \right]^\tau = \frac{K_{on}^D + c + \alpha_{3/2}\tau}{K_{off}^D + c + \alpha_1\tau}
\end{aligned}$$

Finding the root  $\alpha_{3/2}$  of equation C.23 for a given  $\alpha_1$  defines the map from  $\alpha_1$  to  $\alpha_{3/2}$ , i.e.,  $\alpha_{3/2} = F_3(\alpha_1)$ . However, because  $K_{on}^D = -K_{on}^V$  and  $K_{off}^D = -K_{off}^V$ , this is equivalent to

$$(C.24) \quad \left[ \frac{-(K_{on}^V - c) + \alpha_{3/2}}{-(K_{off}^V - c) + \alpha_1} \right]^\tau = \frac{-(K_{on}^V - c) + \alpha_{3/2}\tau}{-(K_{off}^V - c) + \alpha_1\tau}$$

Hence this map is equivalent to  $\alpha_{3/2} = -F_1(-\alpha_1)$ .

**C.2.4. Map 4 -  $(K_{on}^D, \alpha_{3/2})$  to  $(K_{off}^V, \alpha_2)$ , and Full Map.** Map 3 flows the solution forward in time from the fourth proprioceptive threshold at  $K_{on}^D$  to the first threshold at  $K_{off}^V$  to map  $M = \alpha_{3/2}$  to  $M = \alpha_2$ . Using the general solution (equation C.3) with the initial condition  $K = K_{on}^D$ ,  $M = \alpha_{3/2}$ ,  $S_D = 1$ ,  $S_V = 1$ , and equilibrium  $c(S_D - S_V) = 0$ , we obtain the coefficients

$$(C.25) \quad B = \frac{K_{on}^D + \alpha_{3/2}}{1 - 1/\tau},$$

$$(C.26) \quad A = K_{on}^D - B.$$

Next, we solve for the proprioceptive-threshold crossing time, i.e., the time  $t_2$  such that

$$(C.27) \quad K(t_2) = K_{off}^V, \quad M(t_2) = \alpha_2.$$

With the general solution (equation C.3) and coefficients (equations C.25-C.26), we sum together  $K(t_2)$  and  $M(t_2)$  to obtain an equation for the crossing time  $t_2$ :

$$(C.28) \quad t_2 = -\tau \ln \left[ \frac{K_{off}^V + \alpha_2}{K_{on}^D + \alpha_{3/2}} \right].$$

By going through a similar process as in the previous subsection, one can show that the map from  $\alpha_{3/2}$  to  $\alpha_2$  is given by  $\alpha_2 = -F_2(-\alpha_{3/2})$ . Then since

$$(C.29) \quad \alpha_{1/2} = F_1(\alpha_0),$$

$$(C.30) \quad \alpha_1 = F_2(\alpha_{1/2}),$$

$$(C.31) \quad \alpha_{3/2} = -F_1(-\alpha_1),$$

$$(C.32) \quad \alpha_2 = -F_2(-\alpha_{3/2}),$$

the full map is

$$(C.33) \quad \alpha_2 = F(\alpha_0) = -F_2(F_1(-F_2(F_1(\alpha_0)))).$$

### C.3. Numerically Finding the Roots of the Map Branches

For Map 1, numerically finding the root of  $F_1(\alpha)$  (equation C.13) using Newton-like methods is aided by computing bounds on  $\alpha_{1/2}$ . In the limit cycle trajectory, the system crosses the threshold  $K_{off}^V$  from the right and the threshold  $K_{on}^V$  from the left, so  $\alpha_0 < 0$  and  $\alpha_{1/2} > 0$ . By combining equations C.12 and C.13, we also have that

$$(C.34) \quad t_{1/2} = -\tau \ln \left( \frac{K_{on}^V - c + \alpha_{1/2}}{K_{off}^V - c + \alpha_0} \right) = -\ln \left( \frac{K_{on}^V - c + \alpha_{1/2}\tau}{K_{off}^V - c + \alpha_0\tau} \right).$$

In order for the crossing time  $t_{1/2}$  to be real, we must have that argument to  $\ln$  is always positive. Since  $K_{off}^V, \alpha_0 < 0$  and  $c, \tau > 0$ , the denominators  $K_{off}^V - c + \alpha_0$  and  $K_{off}^V - c + \alpha_0\tau$  are always negative. So in order to obtain a real  $t_{1/2}$  from equation C.34, we must have

$$(C.35) \quad K_{on}^V - c + \alpha_{1/2} < 0$$

and

$$(C.36) \quad K_{on}^V - c + \alpha_{1/2}\tau < 0.$$

These inequalities yield the following bounds on  $\alpha_{1/2}$ :

$$(C.37) \quad 0 < \alpha_{1/2} < c - K_{on}^V$$

$$(C.38) \quad 0 < \alpha_{1/2} < \frac{c - K_{on}^V}{\tau}.$$

These bounds imply that we must have  $c > K_{on}^V$  to have a real crossing time  $t_{1/2}$ . In finding the root of the map  $\alpha_{1/2} = F(\alpha_0)$  (equation C.13), we choose whichever bound on  $\alpha_{1/2}$  as our initial root-finding interval is tighter depending on whether  $\tau > 1$  or  $\tau < 1$ . Note that these bounds also guarantee that  $t_{1/2} > 0$ .

In summary, in order to guarantee a first crossing time  $t_{1/2}$ , we must have  $c > K_{on}^V$ . Then, if  $\tau < 1$ , we will find the root  $\alpha_{1/2}$  of the above map  $\alpha_{1/2} = F(\alpha_0)$  in the interval

$$(C.39) \quad \alpha_{1/2} \in (0, c - K_{on}^V).$$

If  $\tau > 1$ , we will find the root  $\alpha_{1/2}$  in the interval

$$(C.40) \quad \alpha_{1/2} \in \left(0, \frac{c - K_{on}^V}{\tau}\right).$$

For Map 2, numerically finding the root of  $F_2(\alpha)$  (equation C.18) using Newton-like methods is aided by computing bounds on  $\alpha_1$ . In the limit cycle trajectory, the system crosses the threshold  $K_{on}^V$  from the left and the threshold  $K_{off}^D$  from the left, so  $\alpha_{1/2} > 0$  and  $\alpha_1 > 0$ . Since  $K_{on}^V$  and  $K_{off}^D$  are also both positive, equation C.17 will always yield a real, finite crossing time  $t_1$ .

By combining equations C.17 and C.18, we also have that

$$(C.41) \quad t_1 = -\tau \ln \left( \frac{K_{off}^D + \alpha_1}{K_{on}^V + \alpha_{1/2}} \right) = -\ln \left( \frac{K_{off}^D + \alpha_1 \tau}{K_{on}^V + \alpha_{1/2} \tau} \right).$$

We also know that  $0 < \alpha_{1/2} < c - K_{on}^V$  from equation C.37, so in order for  $t_1$  to be positive and real, we must have that

$$(C.42) \quad 0 < K_{off}^D + \alpha_1 < K_{on}^V + \alpha_{1/2} < c,$$

$$(C.43) \quad 0 < K_{off}^D + \alpha_1 \tau < K_{on}^V + \alpha_{1/2} \tau < K_{on}^V + (c - K_{on}^V) \tau.$$

Thus we have two bounds on  $\alpha_1$  for our root-finding method:

$$(C.44) \quad 0 < \alpha_1 < c - K_{off}^D,$$

$$(C.45) \quad 0 < \alpha_1 < \frac{K_{on}^V(1 - \tau) + c\tau - K_{off}^D}{\tau}.$$

From the limit cycle trajectory, we expect  $\alpha_1$  to be close to  $\alpha_{1/2}$ , so we can also use this as our initial guess, or whichever interval is tighter. In order for  $t_1$  or  $\alpha_1$  to exist, we also have bounds on the nondimensional feedback strength  $c$ :

$$(C.46) \quad c > K_{off}^D,$$

$$(C.47) \quad c > \frac{K_{off}^D + K_{on}^V(\tau - 1)}{\tau}.$$

For Map 3, since  $\alpha_{3/2} = -F_1(\alpha_1)$ , we should follow the same rules as in Map 1 for numerically finding the root. For Map 3, since  $\alpha_2 = -F_2(-\alpha_{3/2})$ , we should follow the same rules as in Map 2 for numerically finding the root.

#### C.4. Limit Cycle from Map

After finding the fixed point  $\alpha^*$  of the 1-D map (equation C.33), we can piece together an analytic expression for the limit cycle. First, we compute the period  $T$  of the limit cycle by summing the proprioceptive-threshold crossing times:

$$(C.48) \quad T = t_{1/2} + t_1 + t_{3/2} + t_2 = 2t_{1/2} + 2t_1.$$

That is, we use  $\alpha_0 = \alpha_2 = \alpha^*$  to compute  $\alpha_{1/2}, \alpha_1$ , and  $\alpha_{3/2}$  using equations C.13, C.18, and C.23, and then we compute the crossing times  $t_{1/2}, t_1, t_{3/2}$ , and  $t_2$  by equations C.12, C.17, C.22, and C.28. Then we can define the limit cycle by piecing together the solutions along each branch of the map:

$$(C.49) \quad K(t) = \begin{cases} A_1 e^{-t} + B_1 e^{-t/\tau} + c, & t \pmod{T} \in [0, t_{1/2}], \\ A_2 e^{-t} + B_2 e^{-t/\tau}, & t \pmod{T} \in [t_{1/2}, t_{1/2} + t_1], \\ A_3 e^{-t} + B_3 e^{-t/\tau} - c, & t \pmod{T} \in [t_{1/2} + t_1, t_{1/2} + t_1 + t_{3/2}], \\ A_4 e^{-t} + B_4 e^{-t/\tau}, & t \pmod{T} \in [t_{1/2} + t_1 + t_{3/2}, T], \end{cases}$$

where the coefficients  $B_1, A_1$  are given by equations C.9,C.10, the coefficients  $B_2, A_2$  are given by equations C.14,C.15, the coefficients  $B_3, A_3$  are given by equations C.19,C.20, and the coefficients  $B_4, A_4$  are given by equations C.25,C.26. The curvature amplitude of the limit cycle can be computed as the max  $K(t)$  in equation C.49.

## Bibliography

- [1] Z. ALTUN AND D. HALL, *Wormatlas*, 2002.
- [2] M. BACKHOLM, W. S. RYU, AND K. DALNOKI-VERESS, *Viscoelastic properties of the nematode caenorhabditis elegans, a self-similar, shear-thinning worm*, Proceedings of the National Academy of Sciences, 110 (2013), pp. 4528–4533.
- [3] S. BERRI, J. H. BOYLE, M. TASSIERI, I. A. HOPE, AND N. COHEN, *Forward locomotion of the nematode c. elegans is achieved through modulation of a single gait*, HFSP Journal, 3 (2009), pp. 186–193.
- [4] A. BORGMANN, H. SCHARSTEIN, AND A. BÜSCHGES, *Intersegmental coordination: Influence of a single walking leg on the neighboring segments in the stick insect walking system*, Journal of Neurophysiology, 98 (2007), pp. 1685–1696.
- [5] J. H. BOYLE, S. BERRI, AND N. COHEN, *Gait modulation in c. elegans: An integrated neuromechanical model*, Front Comput Neurosci, 6 (2012), p. 10.
- [6] J. H. BOYLE, J. BRYDEN, AND N. COHEN, *An integrated neuro-mechanical model of c. elegans forward locomotion*, in Neural Information Processing, M. Ishikawa, K. Doya, H. Miyamoto, and T. Yamakawa, eds., Berlin, Heidelberg, 2008, Springer Berlin Heidelberg, pp. 37–47.
- [7] J. BRYDEN AND N. COHEN, *Neural control of caenorhabditis elegans forward locomotion: the role of sensory feedback*, Biological Cybernetics, 98 (2008), pp. 339–351.
- [8] A. H. COHEN, G. BARD ERMENTROUT, T. KIEMEL, N. KOPELL, K. A. SIGVARDT, AND T. L. WILLIAMS, *Modelling of intersegmental coordination in the lamprey central pattern generator for locomotion*, Trends in Neurosciences, 15 (1992), pp. 434–438.
- [9] N. COHEN AND T. RANNER, *A new computational method for a model of c. elegans biomechanics: Insights into elasticity and locomotion performance*, arXiv:1702.04988v1 [physics.bio-ph], (2017).
- [10] N. COHEN AND T. SANDERS, *Nematode locomotion: dissecting the neuronal–environmental loop*, Current Opinion in Neurobiology, 25 (2014), pp. 99–106.
- [11] J. E. DENHAM, T. RANNER, AND N. COHEN, *Signatures of proprioceptive control in caenorhabditis elegans locomotion*, Philosophical Transactions of the Royal Society B: Biological Sciences, 373 (2018), p. 20180208.
- [12] P. ERDÖS AND E. NIEBUR, *The neural basis of the locomotion of nematodes*, in Statistical Mechanics of Neural Networks, L. Garrido, ed., Berlin, Heidelberg, 1990, Springer Berlin Heidelberg, pp. 253–267.
- [13] B. ERMENTROUT, *Xppaut®: The differential equations tool, version 5.98*, 2006.

- [14] G. B. ERMENTROUT AND N. KOPELL, *Multiple pulse interactions and averaging in systems of coupled neural oscillators*, *Journal of Mathematical Biology*, 29 (1991), pp. 195–217.
- [15] C. FANG-YEN, M. WYART, J. XIE, R. KAWAI, T. KODGER, S. CHEN, Q. WEN, AND A. D. T. SAMUEL, *Biomechanical analysis of gait adaptation in the nematode *caenorhabditis elegans**, *Proc Natl Acad Sci U S A*, 107 (2010), pp. 20323–8.
- [16] A. D. FOUAD, S. TENG, J. R. MARK, A. LIU, P. ALVAREZ-ILLERA, H. JI, A. DU, P. D. BHIRGOO, E. CORNBATH, S. A. GUAN, AND C. FANG-YEN, *Distributed rhythm generators underlie *caenorhabditis elegans* forward locomotion*, *Elife*, 7 (2018).
- [17] FUCHS, *Intersegmental coordination of cockroach locomotion: adaptive control of centrally coupled pattern generator circuits*, *Frontiers in Neural Circuits*, (2010).
- [18] S. GAO, S. A. GUAN, A. D. FOUAD, J. MENG, T. KAWANO, Y.-C. HUANG, Y. LI, S. ALCAIRE, W. HUNG, Y. LU, Y. B. QI, Y. JIN, M. ALKEMA, C. FANG-YEN, AND M. ZHEN, *Excitatory motor neurons are local oscillators for backward locomotion*, *Elife*, 7 (2018).
- [19] J. GJORGJIEVA, D. BIRON, AND G. HASPEL, *Neurobiology of *caenorhabditis elegans* locomotion: Where do we stand?*, *BioScience*, 64 (2014), pp. 476–486.
- [20] R. GOLDSCHMIDT, *Das nervensystem von *ascaris lumbricoides* und *megaloccephala**, *Z. wiss. Zool*, 11 (1909), pp. 306–357.
- [21] J. GUCKENHEIMER AND P. HOLMES, *Nonlinear oscillations, dynamical systems, and bifurcations of vector fields*, vol. 42, Springer Science & Business Media, 2013.
- [22] T. W. HARRIS, I. ANTOSHECHKIN, T. BIERI, D. BLASJAR, J. CHAN, W. J. CHEN, N. DE LA CRUZ, P. DAVIS, M. DUESBURY, R. FANG, J. FERNANDES, M. HAN, R. KISHORE, R. LEE, H.-M. MÄLLER, C. NAKAMURA, P. OZERSKY, A. PETCHERSKI, A. RANGARAJAN, A. ROGERS, G. SCHINDELMAN, E. M. SCHWARZ, M. A. TULI, K. VAN AUKEN, D. WANG, X. WANG, G. WILLIAMS, K. YOOK, R. DURBIN, L. D. STEIN, J. SPIETH, AND P. W. STERNBERG, *WormBase: a comprehensive resource for nematode research*, *Nucleic Acids Research*, 38 (2009), pp. D463–D467.
- [23] G. HASPEL AND M. J. O'DONOVAN, *A perimotor framework reveals functional segmentation in the motoneuronal network controlling locomotion in *caenorhabditis elegans**, *Journal of Neuroscience*, 31 (2011), pp. 14611–14623.
- [24] P. HOLMES, R. J. FULL, D. KODITSCHKEK, AND J. GUCKENHEIMER, *The dynamics of legged locomotion: Models, analyses, and challenges*, *SIAM Review*, 48 (2006), pp. 207–304.
- [25] E. J. IZQUIERDO AND R. D. BEER, *The whole worm: brain–body–environment models of *c. elegans**, *Current opinion in neurobiology*, 40 (2016), pp. 23–30.
- [26] E. J. IZQUIERDO AND R. D. BEER, *From head to tail: a neuromechanical model of forward locomotion in *caenorhabditis elegans**, *Philosophical Transactions of the Royal Society B: Biological Sciences*, 373 (2018), p. 20170374.

- [27] H. JI, A. D. FOUAD, AND C. FANG-YEN, *A novel model of bending wave generation supports a threshold-switch mechanism in the c. elegans motor circuit*, in the Proceedings of the 22nd International C. elegans Conference, 2019.
- [28] J. KARBOWSKI, G. SCHINDELMAN, C. J. CRONIN, A. SEAH, AND P. W. STERNBERG, *Systems level circuit model of c. elegans undulatory locomotion: mathematical modeling and molecular genetics*, Journal of Computational Neuroscience, 24 (2008), pp. 253–276.
- [29] N. KOPELL AND G. ERMENTROUT, *Coupled oscillators and the design of central pattern generators*, Mathematical Biosciences, 90 (1988), pp. 87 – 109.
- [30] N. KOPELL AND G. B. ERMENTROUT, *Symmetry and phaselocking in chains of weakly coupled oscillators*, Communications on Pure and Applied Mathematics, 39 (1986), pp. 623–660.
- [31] J. KUNERT, E. SHLIZERMAN, AND J. N. KUTZ, *Low-dimensional functionality of complex network dynamics: Neurosensory integration in the caenorhabditis elegans connectome*, Phys. Rev. E, 89 (2014), p. 052805.
- [32] B. C. LUDWAR, M. L. GÖRITZ, AND J. SCHMIDT, *Intersegmental coordination of walking movements in stick insects*, Journal of Neurophysiology, 93 (2005), pp. 1255–1265.
- [33] E. MARDER AND R. L. CALABRESE, *Principles of rhythmic motor pattern generation*, Physiological Reviews, 76 (1996), pp. 687–717.
- [34] J. E. MELLEM, P. J. BROCKIE, D. M. MADSEN, AND A. V. MARICQ, *Action potentials contribute to neuronal signaling in c. elegans*, Nat Neurosci, 11 (2008), pp. 865–7.
- [35] B. MILLIGAN, N. CURTIN, AND Q. BONE, *Contractile properties of obliquely striated muscle from the mantle of squid (alloteuthis subulata) and cuttlefish (sepia officinalis)*, Journal of Experimental Biology, 200 (1997), pp. 2425–2436.
- [36] O. J. MULLINS, J. T. HACKETT, J. T. BUCHANAN, AND W. O. FRIESEN, *Neuronal control of swimming behavior: comparison of vertebrate and invertebrate model systems*, Prog Neurobiol, 93 (2011), pp. 244–69.
- [37] T. NETOFF, M. SCHWEMMER, AND T. LEWIS, *Phase Response Curves in Neuroscience*, vol. 6 of Springer Series in Computational Neuroscience, Springer, 2012, ch. Experimentally Estimating Phase Response Curves of Neurons: Theoretical and Practical Issues.
- [38] E. NIEBUR AND P. ERDÖS, *Theory of the locomotion of nematodes*, Biophysical Journal, 60 (1991), pp. 1132–1146.
- [39] E. NIEBUR AND P. ERDOS, *Theory of the locomotion of nematodes: Control of the somatic motor neurons by interneurons*, Mathematical Biosciences, 118 (1993), pp. 51 – 82.
- [40] V. M. NIGON AND M.-A. FÉLIX, *History of research on c. elegans and other free-living nematodes as model organisms*, WormBook, 2017 (2017), pp. 1–84.
- [41] E. O. OLIVARES, E. J. IZQUIERDO, AND R. D. BEER, *Potential role of a ventral nerve cord central pattern generator in forward and backward locomotion in caenorhabditis elegans*, Network Neuroscience, 2 (2018), pp. 323–343.

- [42] K. G. PEARSON, *Generating the walking gait: role of sensory feedback*, Brain Mechanisms for the Integration of Posture and Movement, (2004), pp. 123–129.
- [43] W. R. SCHAFER, *Proprioception: A channel for body sense in the worm*, Current Biology, 16 (2006), pp. R509–R511.
- [44] M. A. SCHWEMMER AND T. J. LEWIS, *The Theory of Weakly Coupled Oscillators*, Springer New York, New York, NY, 2012, pp. 3–31.
- [45] K. A. SIGVARDT AND T. L. WILLIAMS, *Effects of local oscillator frequency on intersegmental coordination in the lamprey locomotor cpg: theory and experiment*, J Neurophysiol, 76 (1996), pp. 4094–103.
- [46] F. K. SKINNER, N. KOPELL, AND B. MULLONEY, *How does the crayfish swimmeret system work? insights from nearest-neighbor coupled oscillator models*, J Comput Neurosci, 4 (1997), pp. 151–60.
- [47] F. K. SKINNER AND B. MULLONEY, *Intersegmental coordination in invertebrates and vertebrates*, Curr Opin Neurobiol, 8 (1998), pp. 725–32.
- [48] A. O. STRETTON, R. E. DAVIS, J. D. ANGSTADT, J. E. DONMOYER, AND C. D. JOHNSON, *Neural control of behaviour in ascaris*, Trends in Neurosciences, 8 (1985), pp. 294 – 300.
- [49] J. SZNITMAN, X. SHEN, P. K. PUROHIT, AND P. E. ARRATIA, *The effects of fluid viscosity on the kinematics and material properties of c. elegans swimming at low reynolds number*, Experimental Mechanics, 50 (2010), pp. 1303–1311.
- [50] E. D. TYTELL, C.-Y. HSU, T. L. WILLIAMS, A. H. COHEN, AND L. J. FAUCI, *Interactions between internal forces, body stiffness, and fluid environment in a neuromechanical model of lamprey swimming*, Proceedings of the National Academy of Sciences, 107 (2010), pp. 19832–19837.
- [51] Q. WEN, M. D. PO, E. HULME, S. CHEN, X. LIU, S. W. KWOK, M. GERSHOW, A. M. LEIFER, V. BUTLER, C. FANG-YEN, T. KAWANO, W. R. SCHAFER, G. WHITESIDES, M. WYART, D. B. CHKLOVSKII, M. ZHEN, AND A. D. T. SAMUEL, *Proprioceptive coupling within motor neurons drives c. elegans forward locomotion*, Neuron, 76 (2012), pp. 750–61.
- [52] J. G. WHITE, *Getting into the mind of a worm— a personal view*.
- [53] J. G. WHITE, E. SOUTHGATE, J. N. THOMSON, AND S. BRENNER, *The structure of the nervous system of the nematode caenorhabditis elegans*, Philos Trans R Soc Lond B Biol Sci, 314 (1986), pp. 1–340.
- [54] C. H. WIGGINS, *Flexive and propulsive dynamics of elastica at low reynolds number*, Physical Review Letters, 80 (1998), pp. 3879–3882.
- [55] T. L. WILLIAMS, K. A. SIGVARDT, N. KOPELL, G. B. ERMENTROUT, AND M. P. REMLER, *Forcing of coupled nonlinear oscillators: studies of intersegmental coordination in the lamprey locomotor central pattern generator*, J Neurophysiol, 64 (1990), pp. 862–71.

- [56] C. ZHANG, R. D. GUY, B. MULLONEY, Q. ZHANG, AND T. J. LEWIS, *Neural mechanism of optimal limb coordination in crustacean swimming*, Proceedings of the National Academy of Sciences, 111 (2014), pp. 13840–13845.
- [57] C. ZHANG AND T. J. LEWIS, *Phase response properties of half-center oscillators*, Journal of Computational Neuroscience, 35 (2013), pp. 55–74.
- [58] M. ZHEN AND A. D. T. SAMUEL, *C. elegans locomotion: small circuits, complex functions*, Curr Opin Neurobiol, 33 (2015), pp. 117–26.